ARMCX proteins regulate mitochondrial function in the Retinal Pigment Epithelium

Dilyana Doncheva

September 2021

Thesis submitted in fulfilment of the requirements for the degree of

Doctor of Philosophy

University College London (UCL)

Institute of Ophthalmology

Declaration

I, Dilyana Doncheva, confirm that the work presented in this thesis is my own. Where information has been derived from other sources, I confirm that this has been indicated in the thesis.

Acknowledgement

When I arrived in England, exactly 10 years ago, I could hardly string a sentence in English. I studied the language extensively for a year before I embarked on BSc Pharmacology and Molecular Genetics at King's College London. While continuing to brush up my English I succeeded in completing my Bachelor's degree with upper-second class honours. I became very interested in research and it was already at King's that I decided that I wanted to do a PhD. Following a gap year I was accepted at Imperial College London to do MRes Biomedical Research, which prepared me for the next chapter of my academic career – becoming a PhD candidate at University College London. Four years later, despite the difficulties associated with the Covid-19 pandemic and the typical symptoms from the last months of a planned pregnancy, which came a bit earlier than expected, I present my PhD thesis, a culmination of all the hard work I have put in over the last 10 years. What a journey it has been!

I was, however, not alone on this journey and I would like to acknowledge the people responsible for shaping me into the scientist I am today.

I would like to firstly thank my dear husband Todor Donchev and my wider family for all of their support and for giving me the strength to continue and never give up.

I would also like to express my sincere gratitude to Prof Patric Turowski for taking me on as a PhD student, guiding me throughout the years and especially teaching me biochemistry and strengthening my knowledge of molecular biology techniques. This thesis would not have been possible without his help, support and patience.

My special thanks go to Dr Emily Eden, who took over from Dr Pete Coffey as my second supervisor and was invaluable throughout my PhD studies. I am forever grateful for her advice and help as well as encouragement and support throughout my PhD and in particular during the final months on managing it whilst pregnant.

I am grateful also to Prof Peter Coffey for being my first secondary supervisor and supporting me during my upgrade.

I would like to take the opportunity to thank Dr William Grey who was a great teacher to me during my first research internship in the summer following my first year at King's. I would also like to give credit to Dr Edwige Voisset who together with Dr Grey sparked my interest in research.

Prof Eric Lamb, my supervisor during my time at Imperial, has had a considerable impact on my academic and personal development and I would like to also take this opportunity to thank him for all his guidance and help, preparing me to realise my goal of embarking on a PhD.

I would like to thank my colleagues and friends at Turowski's lab Ms Bruna Caridi, Dr Karen Frudd, Dr Silvia Dragoni, and Dr Jui-Hsien (Cher) Chang who helped me greatly and with whom we've have a lot of fun times together.

I would also like to extend my highest appreciation to Moorfields Eye Charity, who provided the necessary financial support for this research.

Following a period dedicated to my little girl, who's arrival my husband and I are eagerly awaiting, I look forward to the post-doctorate journey ahead, which I will have the pleasure to start with Dr Emily Eden.

Abstract

Retinal Pigment Epithelium (RPE) functions, including energy absorption, photo-pigment recycling, and oxidative stress regulation, depend on a healthy mitochondrial network. Notably, RPE mitochondrial integrity declines during aging and even more so Age-related Macular Degeneration (AMD). Healthy mitochondria pervade the entirety of the cell as an organelle network undergoing constant dynamic renewal through fusion, fission and mitophagy. Armadillo repeat-containing genes located on the X chromosome (Armcx) form an Eutharian specific cluster of 6 genes which are implicated in mitochondrial motility in axons and, more generally, in mitophagy (as substrates of Parkin). Armcx6 is up-regulated in differentiated RPE whilst Armcx3 is down-regulated in AMD, collectively suggesting an important role in the homeostasis of RPE. This study specifically analysed the role of Armcx proteins in RPE cells.

Armcx1, 2, 3 and 6 but not 4 or 5 are found as bona fide mitochondrial regulators and to be upregulated in RPE differentiation *in vitro*. Further analysis focused on Armcx1 and Armcx2 showed both proteins to affect mitochondrial network differently in RPE. Endogenous Armcx1 and Armcx2 were strongly associated with mitochondria in ARPE-19 cells and strongly expressed in the RPE layer of human retina. Armcx1 knockdown resulted in increased mitochondrial motility, whereas Armcx2 depletion led to decreased mitochondrial movements. Armcx overexpression resulted in aggregation and

reduced mobility of mitochondria indicating disrupted dynamics. Armcx1 and Armcx2 knockdown resulted in fragmented mitochondria, however with different phenotypes, suggesting enhanced fission and/or mitophagy. Indeed, Armcx1 knockdown showed increased Parkin activation upon mitophagy induction, whereas Armcx2 resulted in no difference. In addition, Lamp2 expression was also affected differently, by Armcx1 depletion leading to upregulated Lamp2, in contrast to Armcx2 knockdown which decreased Lamp2 levels. Moreover, compensatory experiments using marsupial Armc10 revealed that Armcx1 and Armcx2 have acquired novel roles during their evolution in the Eutherian clade, probably to fulfil new functions essential to support the more complex Eutherian clade.

Impact Statement

RPE plays an important role in the support of retinal function and thus maintaining healthy vision. Non-functional RPE has been linked with the development of AMD, a major cause of blindness worldwide. In this study, we provide first evidence for an important physiological role of a family of molecules (known as Armcx) in RPE cells. A member of these molecules (Armcx3) has previously been reported to be linked to the pathophysiology of AMD. This study generates insights into fundamental science relevant for researchers in cell and molecular biology. The data from this study will raise further questions to be addressed in further research looking to better understand the function of RPE and related diseases. In this report we also describe molecular pathways linked to the Armcx molecules, which have not been explored thus far. Therefore, this research will help widen the overall knowledge of their physiological role.

Table of Contents

List of Figures

List of Tables

Abbreviations

Ab	Antibody
Alex	Arm-containing protein lost in epithelial cancers linked to X-chromosome
AMD	Age-related macular degeneration
AMPK	5' AMP-activated protein kinase
APS	Ammonium persulfate
Arm	Armadillo domain
Armcx	Armadillo repeat-containing genes located on the X chromosome
ATG9	Autophagy-related protein 9
ATP	Adenosine triphosphate
BHLH9	GASP 3
BM	Bruch’s membrane
BRB	Blood-retinal barrier
BSA	Bovine serum albumin
CCCP	Carbonyl cyanide m-chlorophenylhydrazone
Covid-19	Coronavirus disease from 2019
DAPI	4′,6-diamidino-2-phenylindole
DDSA	Dodecenyl succinic anhydridie
DMEM	Dulbecco’s modified eagle’s medium
DMP30	Tris (dimethylaminomethyl)phenol, 2,4,6-tris (dimethylaminomethyl)phenol

DMSO	Dimethyl sulfoxide
Drp-1	Dynamin-related protein-1
ECL	Enhanced chemiluminescence
EM	Electron microscopy
EMBL-EBI	European Molecular Biology Laboratory's European Bioinformatics Institute
ER	Endoplasmic reticulum
FCS	Fetal calf serum
GASP	G-protein-coupled receptor associated sorting G-protein
GCL	Ganglion cell layer
GLUT	Glucose transporter
GPCR	G-protein-coupled receptor
GTEx	Genotype-tissue expression
HRP	Horse radish peroxidase
IMM	Inner mitochondrial membrane
INL	Inner nuclear layer
IRB	Institutional Review Board
LB	Luria broth
LC3-II	Microtubule-associated protein-1/2 light chain-3
MCT	Monocarboxylate transporter
MerTK	Tyrosine kinase c-mer
MFF	Mitochondrial fission factor
Mfn1	Mitofusin 1

MiNa	Mitochondrial network analysis tool
mtDNA	Mitochondrial DNA
MTS	Mitochondrial targeting sequence
NCBI	National Center for Biotechnology Information
NLS	Nuclear localisation signal
NTS	Nuclear targeting signals
OMM	Outer mitochondrial membrane
ON/IS	Outer/Inner photoreceptor segment
ONL	Outer nuclear layer
OPA1	Optic atrophy 1
PBS	Phosphate buffered saline
PCR	Polymerase chain reaction
PGC-1a	Peroxisome proliferator-activated receptor gamma coactivator 1-alpha
PINK1	PTEN-induced kinase 1
ROS	Reactive oxygen species
RPE	Retinal pigment epithelium
RT-qPCR	Real-time polymerase chain reaction
SAP	Shrimp alkaline phosphatase
SDS	Sodium dodecyl sulfate
SEM	Standard error of the mean
TBS	Tris-buffer saline
TEER	Transepithelial electrical resistance

TEMED	N′-Tetramethyl ethylenediamine
TM	Transmembrane domain
TPM	Transcripts per million
Trak1	Trafficking kinesin protein 1
Trak2	Trafficking kinesin protein 2
UCL	University College London
UCSB	University of California, Santa Barbara
VEGF	Vascular endothelial growth factor
VWR	VWR International

Chapter 1 Introduction

1.1 Retinal Pigment Epithelium (RPE)

1.1.1 RPE location and structure

The retina, also known as the neural portion of the eye, consists of different cell types, which function in parallel in light absorption, its transmission into electrical stimuli that are captured by the brain and ultimately to process visual recognition (Purves, 2004). The retina of all vertebrates comprises five neuronal cell types: photoreceptors, bipolar, ganglion, horizontal and amacrine cells (Figure 1.1). The former three participate in the direct transformation of light absorption into neuronal signal. The neuronal cell bodies of the retina are located in the inner, outer nuclear and ganglionic cell layers, with all connecting processes and synapses located in the inner and outer plexiform layers. Photoreceptor cells represent the light sensitive elements of the retina consisting of two cell types – rods and cones – which can detect different light wavelengths (Purves, 2004, Hoon et al., 2014). The majority of photoreceptor cells in the human retina are rods (up to 95%) and they have the ability to respond to individual photons of light. They allow vision under very low light levels, especially important for our late ancestors that spent most of their lives in the dark. Cones, on the other hand, comprise a small proportion (up to 5%) of the total photoreceptors where each cell displays sensitivity to a specific light wavelength. Despite their overall number, cones are packed at a high-density region in the retina responsible for bright-light, colourful high visual acuity, which we mostly rely on nowadays (Lamb, 2016).

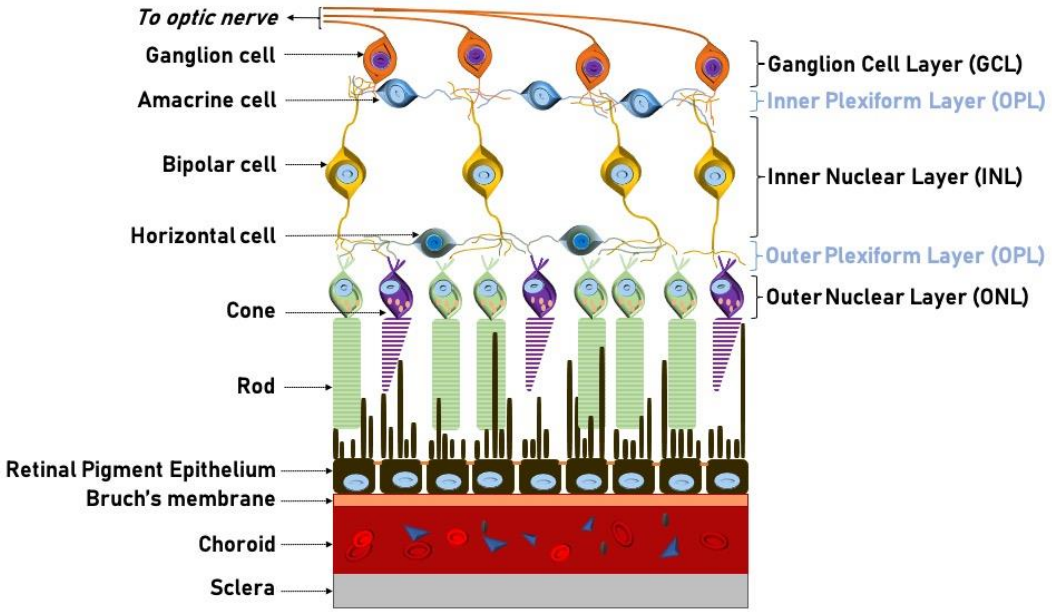

Figure 1.1 Structure of the vertebrate retina. Schematic illustration of the basic circuitry of the retina showing the five neuronal cell types – photoreceptors, horizontal, bipolar, amacrine and ganglionic cells. Rods and cones are supported by the Retinal Pigment Epithelium (RPE) that is attached to the Bruch's membrane. The blood supply of the outer retina comes from the choroid positioned between the Bruch's membrane and the sclera. Diagram is adapted from Caridi et al. (Caridi et al., 2021).

The light is captured by the photopigment in the outer segments of both photoreceptor types and triggers a synaptic signal to travel via bipolar to ganglionic cells. Depending on the light conditions, signals are modified and integrated by horizontal cells, connecting multiple photoreceptors with bipolar cells, and amacrine cells which short axons connect with the ganglion cell dendrites. Ultimately, the integrated flow of information is transmitted via long axons of the ganglion cells to the rest of the central nervous system. During this dynamic process of visual recognition photoreceptors undergo daily renewal where new photoreceptor outer segments are synthesised, and the old ones are shed. Importantly, the photoreceptors are unable neither to process their expended outer segments nor to renew the photopigment, both

of which processes optimal activity is crucial for the proper visual process (Masland, 2001, Purves, 2004, Hoon et al., 2014). Therefore, photoreceptors need a support system to maintain their function. The retinal pigment epithelium (RPE) consists of a monolayer of highly differentiated, pigmented cells that are positioned directly behind the photoreceptors. Indeed, RPE is the cell layer that governs a large number of processes in order to maintain healthy and functional photoreceptors and normal visual cycle (Strauss, 2005).

The RPE layer has the same neuroectodermal origin as the retina during development, hence it is considered to be part of the retina. RPE is a simple layer of cuboidal cells that exhibits a hexagonal shape when observed *en face*. The apical side of the RPE carries long microvilli, which disperse towards the light sensitive segments, interdigitating the photoreceptor outersegments and its basal side faces the Bruch's membrane, which separates the RPE from the choriocapillaris (Figure 1.2). Since the retina (including photoreceptors) is avascular, the RPE provides a direct link to the blood stream, where nutrients and waste products are actively transported (Strauss, 2005, Sparrow et al., 2010, Simo et al., 2010).

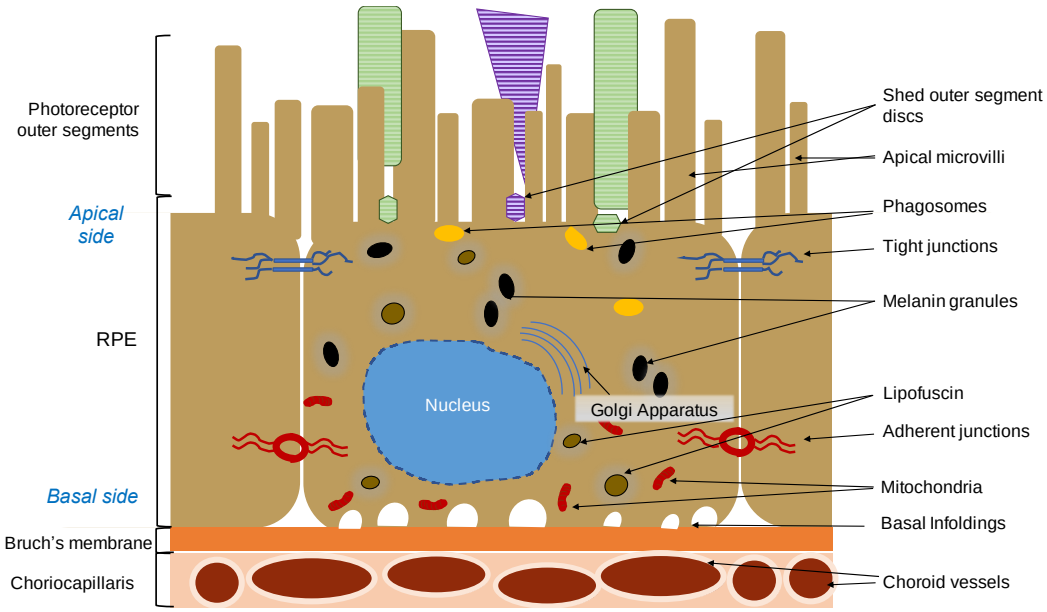

Figure 1.2 RPE anatomy. A schematic illustration of RPE structure and apical connections with the photoreceptor outer segments and basal connections with the Bruch's membrane. The latter separates the RPE from the blood supply. Typical for simple epithelium features are indicated – microvilli, tight and adherent junctions and basal infoldings. Old photoreceptor outer segments are shed and are phagocytosed in the RPE. Melanin and lipofuscin containing vesicles are also indicated.

Similarly, to other epithelial layers the RPE is highly polarised and is interposed between the photoreceptors and choroid capillaries, maintaining different functions for each side. RPE apical side comprises long microvilli made of a stable core of actin filaments, all protruding towards the photoreceptor segments, providing mechanical support and assisting with the removal of shed photoreceptor tips. Basally, RPE also possesses actin filaments in its basal infoldings, whose expansive surface area at the interface with the choroid, enhance essential absorption and secretion from and to the blood supply (Bonilha, 2014). Laterally, RPE membranes are the sites for cellular adhesion and interaction. RPE possesses lateral tight junctions positioned towards the apical surface, which help to maintain cell polarity and to prevent unnecessary intramembranous transport of molecules. Adherent

junctions of actin filaments that form a continuous belt around each cell allowing intact epithelium to be formed (Figure 1.2) (Sparrow et al., 2010, Bonilha, 2014).

Furthermore, at their apical side RPE contains pigment granules melanosomes, which are formed early in postnatal life and are the main site of melanin synthesis (Seagle et al., 2005, Wasmeier et al., 2008). In addition, other pigment-containing vesicles are found in the RPE cells - lipofuscins and melanolipofuscins, numbers of which increase with age. Lipofuscin is stored in lysosomes and formed from incompletely digested photoreceptor outer segments which process increases with age (Boulton, 2014). The nucleus and mitochondria are mostly located at the basal side of the epithelium. Other cellular organelles such as the ER and lysosomes are found spread throughout the cell, but subcellular localisation is also highly regulated and likely important for retina – bloodstream crosstalk (Marmorstein, 2001, Sparrow et al., 2010). As a supportive tissue, RPE functions must be fine-tuned in order to maintain healthy retina and thus support vision.

1.1.2 RPE functions

One of the main functions of RPE is to absorb the scattered light focused on the retina by the lens. The light energy passing through the photoreceptors is captured by melanin found at the apical side of RPE. Melanin also plays a role in scavenging free radicals and reactive oxygen species accumulated from the shed photoreceptor segments (Seagle et al., 2005, Sparrow et al., 2010).

At the interface of the blood supply and retina, transepithelial transport is an extremely important function of RPE, with nutrients and ions delivered from the blood to the neuroretina and electrolytes and waste products dispensed for clearance into the choroid from the subretinal space (Simo et al., 2010). Water is produced in large amounts as a result of neuron and photoreceptor turnover and is eliminated from the subretinal space by the RPE into the bloodstream. This is important for keeping the retinal architecture adjacent (Marmor, 1990, Strauss, 2005). However, water cannot diffuse paracellularly due to the strong tight junctions, instead it is transported via aquaporin-1 driven by Cl^- transepithelial transport out from the retina. The transport of Cl- is orchestrated by an apical Na+/K+ ATPase. The movement of Na+ down its concentration gradient from intracellular to the extracellular space drives Na+/K+/2Cl- co-transporter also located apically. This give rise to the accumulation of Cl^- ions intracellularly and results in basolateral negative and apical positive transepithelial potential, which is crucial for the proper transport of net amounts of fluid in RPE (Marmor et al., 1990; Strauss 1995; Rizzolo L 2014) (Marmor, 1990, Strauss, 1995, Rizzolo, 2014).

Alongside ion transport regulation, RPE maintain pH levels within the subretinal space. As a result of the high metabolic activity in the photoreceptor segments, rods and cones secrete large amounts of lactic acid, which is taken up by the RPE apically via the proton-driven monocarboxylate transporter-1 (MCT-1) and then actively released basally in the choroidal bloodstream via MCT-3. In the opposite direction, nutrients such as glucose, fatty acids, and retinal are taken up from the bloodstream by the RPE and delivered to the

neuroretina. For glucose transport RPE expresses both apically and basally glucose transporters (GLUT1 and GLUT3). Adequate glucose delivery is important to meet the metabolic needs of the photoreceptors (Lehmann et al., 2014).

Furthermore, RPE plays an important role in the visual cycle being the principal site for regeneration of the photosensitive derivate of vitamin A (11-cis retinal). In the photoreceptors cis-retinal is covalently bound to an opsin molecule, to form the visual pigment complex. During light response, the cis-retinal becomes isomerised to all-trans retinal, activating opsin, which triggers the phototransduction cascade and subsequent vision process. Notably, all-trans-retinol is not light sensitive, thus it needs to be converted back to 11-cis-retinal in order for the photoreceptors to be able to use it. The re-isomerisation of all-trans retinal takes places in the RPE, facilitated by the RPE65 enzyme, to ensure the continuous availability of 11-cis retinal and subsequent photoreceptor excitability (Kono et al., 2008, Tsin et al., 2018).

As mentioned earlier, photoreceptors absorb large amounts of light as a result of which they produce waste materials including photo-damaged outer segments. Thus, to maintain visual function, fresh photoreceptors need to be generated, while expended ones need to be eliminated by phagocytosis by RPE. Studies *in vitro* showed the presence of shed outer segments to be sufficient to initiate phagocytosis in RPE. At first shed photoreceptors are transported to the apical side of RPE where they are recognised and transferred to the intracellular space. Receptors such as macrophagic scavenger receptor CD36 and tyrosine kinase c-mer (MerTK) are known to be

involved in shed photoreceptor tips internalisation and activation of secondary messengers to ingest the target, respectively. The process of disk shedding and phagocytosis is precisely coordinated between the RPE and photoreceptors and is under circadian control (Strauss, 2005, Mazzoni et al., 2014).

Moreover, another important function of the RPE is to produce and secrete growth factors that are essential for the retinal and choroidal structural maintenance. One of these factors is the pigment epithelial growth factor (PEDF). PEDF has two important functions: to act as a neuroprotective factor to protect the neuroretinal cells from e.g. hypoxia-induced apoptosis; and to act as an antiangiogenic factor to inhibit abnormal neovascularisation of the choroid (Barnstable and Tombran-Tink, 2004). Another factor synthesised in the RPE with an important function in supporting a healthy retina is the vascular endothelial growth factor (VEGF). This factor is secreted by the basolateral RPE in low amounts in a healthy eye where it prevents apoptosis of endothelial cells and supports an intact endothelium within the choriocapillaris (Strauss, 2005, Apte et al., 2019).

The RPE is also an essential component of the outer blood-retinal barrier (BRB) alongside the Bruch's membrane and choroid. They all participate in the mediation of size-selective passive diffusion of molecules to and from the neuroretina. In contrast to the inner BRB, the outer BRB is composed of tight junctions between the RPE cells and not between endothelial cells. Indeed, the choriocapillaris of the outer BRB are unusually permeable to macromolecules and the tight control over the transport of solutes to the

photoreceptors is directed by the RPE. However, the RPE junctional complexes do not form an impermeable wall instead they allow specific transport of ions according to the needs of the photoreceptor. This permeability is normally observed by measuring the transepithelial electrical resistance (TEER), which indicates ion movements paracellularly (Naylor et al., 2019, Fields et al., 2020). The Bruch's membrane is part of the outer BRB to support RPE layer physically, to allow diffusion of molecules between RPE and choroid and to restrict cell migration between the neuroretina and choriocapillaris. There are five layers of the Bruch's membrane, composed of elastin and collagen-rich extracellular matrices. All of the major components of these layers are produced by the RPE and/or the choroid. The inner layer of the Bruch's membrane serves as the RPE basement membrane providing structural support and differentiation for the RPE layer (Booij et al., 2010). Indeed, many studies showed the importance of the basal membrane and extracellular matrix for RPE differentiation *in vivo* (Marneros et al., 2004) and *in vitro* (Turowski et al., 2004, McLenachan et al., 2017).

Importantly, a failure of any of the RPE functions discussed above can result in photoreceptor degeneration, retinal dysfunction and concomitant visual loss. Although RPE functions have been studied well, there is lack of understanding the exact mechanism(s) of how dysfunctional RPE results in retinal degeneration.

1.1.3 RPE cell culture and differentiation

In order to better understand the consequences of RPE impairment and associated retinal diseases, further studies are needed. However, the location of RPE at the back of the eye makes the direct approach for research challenging. Studies on the RPE *in vitro* are well explored in a variety of applications to study molecular mechanisms in RPE cells (Bonilha, 2014). Importantly, in order to study RPE physiology and pathology *in vitro*, the cell culture needs to reflect as close as possible the natural state of RPE. Primary human cells appear to sustain normal physiological features; however their availability and isolation processes are often an obstacle as well as their low proliferation activity (Dunn et al., 1996). Therefore, in order to surmount this problem, various immortalised RPE cell lines have been established from rat and human species. Despite their global use, cell line cultures fail to preserve many of the characteristic features of RPE *in vivo*, including functional tight junctions and polarity, pigmentation and efficient phagocytosis of photoreceptor outer segments. However, supplementing the medium of RPE cell line cultures showed a promising retention of highly differentiated and functional polarity RPE phenotype (Hu and Bok, 2001, Ahmado et al., 2011).

Mechanistic insight into RPE differentiation will progress the application of RPE cell lines to advancing our understanding of RPE-related pathologies and benefit the development of RPE cell-based therapies and treatments. RPE dysfunction is believed to underly one of the most common causes of irreversible blindness – age-related macular degeneration (AMD) (Nowak, 2006, Inana et al., 2018). Although, the exact mechanisms of AMD pathology

are not well understood, the main complications present in the disease point towards a failure of RPE to support photoreceptor function.

1.2 RPE dysfunction and Mitochondria

1.2.1 RPE dysfunction and AMD

Failure of dysfunctional RPE to support photoreceptors results in progressive photoreceptor degeneration, which is believed to the major cause of vision loss in AMD onset and progression. It is not surprising that in case of dysfunctional RPE, the neuroretina will be compromised. Even though the exact pathophysiology of AMD is not clear, apart from RPE the disease also affects the choroid, Bruch's membrane, and photoreceptors and ultimately destroys the macula (responsible for high acuity vision) (Nowak, 2006).

AMD is a leading cause of blindness in the developed world with increased prevalence in the aging population (aged 50 and over) (Owen et al., 2012, Terluk et al., 2015). There are two types of classified AMD: The dry form, which is slow in progression, affecting most cases. The wet form is characterised by abnormal growth of the blood vessel growth within the choroidal vasculature. Wet AMD progression is fast and affects 10% of AMD cases. Wet AMD form is successfully manageable with anti-angiogenic treatments such as anti-VEGF therapeutic agents (Pugazhendhi et al., 2021). In contrast there is currently no treatment available for dry AMD, which is believed to be due to RPE atrophy resulting in photorecetor loss and subsequent macular degeneration. There are, however, cell-based therapies or RPE replacement

treatments which are being considered to help dry AMD patients (Vitillo et al., 2020, Uyama et al., 2021). Thickening of the Bruch's membrane is another characteristic of dry AMD. Increased lipofuscin formation within the RPE is through to result in deposition of material towards the basal side of the RP and the formation of drusen deposits between the RPE and Bruch's membrane. This accumulation of deposits disrupts the passive diffusion of nutrients between the Bruch's membrane and RPE. In addition, advanced ageing, environmental factors such as smoking, and diet and genetics all contribute to the multicomplexity of AMD pathology (Nowak, 2014).

The final step of both forms of AMD is complete blindness (Wong et al., 2014). The lack of understanding of the underlying mechanism(s) in RPE atrophy and consequent AMD development, coupled with the lack of model research systems, have prevented the development of an established treatment strategy. Emerging evidence is pointing towards increased oxidative stress, inflammation, and mitochondrial dysfunction in RPE, but further research is required to fully understand the underlying exact mechanism (Nowak, 2014, Pugazhendhi et al., 2021).

Since the RPE performs a large amount of energy demanding tasks, it is not surprising that they are very reliant on a stable mitochondrial network. Thus, any functional failure of mitochondria may severely affect RPE homeostasis (Caldwell and Slapnick, 1989, Barot et al., 2011). A large number of age-related degenerative diseases have been linked to mitochondrial dysfunction such as Alzheimer's, Parkinson's and AMD (Barot et al., 2011). The production of reactive oxygen species (ROS), which results in damaged mitochondria

have been described as one of the leading causes of mitochondrial related diseases. The accumulation of oxidative stress in human RPE cells due to a treatment with H_2O_2 and/or rod outer segments resulted in damaged mitochondrial DNA (mtDNA). This was suggested to be the main cause of cell death. Since AMD is strongly associated with loss of RPE, accumulation of damaged mtDNA due to oxidative stress could be a trigger point of AMD (Feher et al., 2006). Furthermore, electron microscopy (EM) results showed a significant decrease in the number and area of mitochondria in human RPE from aging and in AMD patients (Figure 1.3).

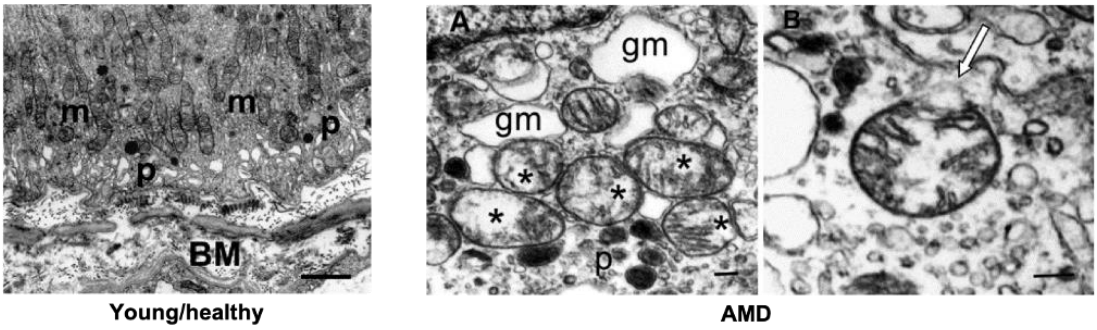

Figure 1.3 Electron microscopy of RPE. Left panel: Elongated mitochondria (m) from healthy patient organised basolateral, close to Bruch's membrane (BM). Right panel: Mitochondria in AMD exhibit morphological changes, loss of matrix density (asterisks) and loss of cristae, sometimes appearing as 'ghost' mitochondria (gm). Inner and outer membranes may also be damaged. The images are adapted from Feher et al 2006 (Feher et al., 2006).

Mitochondrial networks in the RPE from a healthy patient are characterised by long organelles and well-defined mitochondrial matrix. Conversely, mitochondria in the RPE from an AMD patient show substantial loss of matrix density, with mitochondria appearing like "ghosts" and with clear disruption of mitochondrial membrane (Feher et al., 2006).

1.2.2 Mitochondrial morphology and oxidative stress

The mitochondrion is believed to have arisen about two billion years ago from the engulfment of a proteobacterium by a larger eukaryotic precursor cell (Friedman and Nunnari, 2014). Mitochondria are double-membrane organelles, a feature they have conserved from their ancestors. The inner mitochondrial membrane (IMM) is comprised of folded cristae, which are enclosed by an outer mitochondrial membrane (OMM). The former is highly impermeable in comparison to the OMM and contains a large number of mitochondrial transporters (McCarron et al., 2013). The mitochondrial matrix is the innermost part of the organelle, where the citric acid cycle takes place. As a result, electrons are generated and transferred to the respiratory chain, which causes an electrochemical gradient (known as mitochondrial membrane potential) within the IMM resulting in adenosine triphosphate (ATP) production (Osellame et al., 2012). In addition to generating energy, mitochondria perform many other important functions such as Ca^{2+} storage, iron metabolism, apoptosis, and thermogenesis, all important to maintain cellular homeostasis (Dombi et al., 2018).

In contrast to their preserved membrane structures, the mitochondrial genome content was drastically reduced during eukaryotic evolution. Mitochondria possess their own DNA, which encode only 13 proteins important for the respiratory complexes. All other mitochondrial proteins are encoded by the nucleus (Friedman and Nunnari, 2014). Thus, mitochondrial regulation is orchestrated by the gene expression of both mitochondria and nucleus. Mitochondria regulate vital processes in eukaryotes including cellular

metabolism, homeostasis, stress response and energy production (Glancy et al., 2020), thus it is not surprising that their dysfunction is linked to a large number of pathologies including cellular aging and neurodegenerative diseases.

Mitochondria are the major sites of ROS production and detoxification. ROS, such as superoxide anion (O^{2-}) and hydrogen peroxide (H_2O_2) are generated as a product of the respiratory chain in mitochondria (endogenous ROS), exposure to UV light, radiation (exogenous ROS) and others. Mitochondrial ROS are produced as a result of the oxidative phosphorylation in the mitochondrial electron transport chain reaction; and under normal conditions, these species are detoxified and cleared mainly by intracellular antioxidant enzymes. Such enzymes are found in the cytosol (e.g. Cu/Zn-superoxide dismutase) and mitochondrial matrix (e.g. Mn superoxide dismutase) (Nita and Grzybowski, 2016). Initially, ROS production was linked only to pathological conditions to invoke damage, but later emerged as important signalling molecules under physiological conditions. For example, under hypoxic conditions ROS were produced in mitochondria in order to help with metabolic adaption to low oxygen (Chandel et al., 1998). More recently mitochondrial ROS has been implicated in a wide range of biological process such as detecting oxygen concentration, autophagy, immune responses, cell growth and others (Chandel, 2014). Importantly, lipids, proteins and DNA are highly sensitive to the presence of ROS, therefore in cases of high ROS production the cell survival is endangered. This is the general concept of oxidative stress where the levels of oxidants species are higher than the defence mechanisms

resulting in damage to biological molecules and cell death (Filomeni et al., 2015, Choi et al., 2020).

The accumulation of ROS in mitochondria causes mitochondrial dysfunction that has been implicated in neurodegenerative disorders such as Alzheimer's disease (Guo et al., 2013), cancer and in general aging-related diseases including AMD (Srivastava and Kumar, 2015). Mitochondrial content especially their DNA is vulnerable to oxidative damage by being located in close proximity to ROS production in the IMM without the support of histones or other protective proteins (Evans et al., 2004). Accumulating ROS production attacks first the complexes of the mitochondrial respiratory chain, where they are normally generated. This happens by damaging mitochondrial DNA that ultimately affects the gene expression of respiratory chain complexes leading further to dysregulated ROS production and eventually triggers apoptosis (Guo et al., 2013).

An important mechanism of defence against oxidative stress is the removal of damaged proteins and organelles by autophagy. Autophagy is the main pathway of delivery of damaged proteins to the lysosomes, where they are degraded and recycled (Scherz-Shouval and Elazar, 2007). In all eukaryotes, autophagy is highly conserved process with three major types: microautophagy (direct uptake of cargo by the lysosome membrane), chaperone-mediated autophagy (chaperone recognise damaged and misfolded proteins which are then transported directly to lysosomal membrane) and the most widely studied, macroautophagy (referred here as autophagy). Following autophagy initiation, a double-membrane compartment

called a phagophore is formed. The phagophore experiences an elongation event that is supported by the recruitment of protein complexes such as LC3-II (microtubule-associated protein-1 light chain-3) and ATG9 (autophagy-related protein 9). Cytoplasmic cargo becomes completely enclosed during autophagosome formation which is followed by fusion with the lysosomal membrane to form an autolysosome, where the acidic lumen and resident hydrolases of the lysosome causes complete degradation of the damaged intracellular content. Moreover, in some cases, the autophagosome can fuse with early or late endosomes before fusing with lysosomes, a cross-reaction process of autophagy and endocytic pathways that is often seen in mammals (Berg et al., 1998, Parzych and Klionsky, 2014).

Although autophagy is primarily non-selective, preferential autophagy towards impaired organelles such as mitochondria can occur and is known as mitophagy (Scherz-Shouval and Elazar, 2007).

1.2.3 Mitochondrial degradation/mitophagy

Mitophagy is a selective autophagy that involves the degradation of mitochondria. This can occur as part of basal turnover for recycling, or a result of hypoxia and induced damage (Dombi et al., 2018). In addition, mitophagy can be induced without a stressor or impairment and this occurs during the differentiation of red blood cells and retinal ganglion cells. In response to mitophagy triggers such as hypoxia and differentiation, mitochondria are removed via specific interaction of the OMM proteins BNIP3L/NIX with LC3 on

the expanding phagophore subsequently leading to autophagosome formation and degradation (Parzych and Klionsky, 2014, Killackey et al., 2020).

Mitochondrial depolarisation is widely considered a severe mitophagy trigger. Due to membrane potential and the electron transport chain are so intimately connected, ATP generation is impaired under conditions of mitochondrial depolarisation. The exact mechanisms underlying the selective degradation of mitochondria are not completely understood, but it appears that depending on the trigger, different signalling pathways are activated. In contrast to the stress-free mitophagy, severe mitochondrial damage switches on a specific signalling pathway widely known as the PINK1-Parkin complex. Upon mitochondrial depolarisation, cytosolic Parkin (an E3 ubiquitin ligase 3) is phosphorylated by PINK1, that is found on the OMM. Following this post-translational modification, Parkin is recruited to the OMM where it ubiquitinates mitochondrial surface proteins which ultimately serve as autophagy receptor targets leading to mitophagy initiation (Parzych and Klionsky, 2014). Although this mitophagy pathway has been studied well *in vitro*, assessment *in vivo* has been challenging. PINK1 and Parkin knockout studies in mice do not show a phenotype and their basal mitophagy levels were not changed (Walsh et al., 2018, McWilliams et al., 2018). The maintenance of mitochondrial housekeeping functions by basal mitophagy under normal conditions is not well understood. In recent years, scientists developed fluorescent mitophagy reporters (such as mt-Keima and mito-QC) to study mitophagy more *in vivo*. These reporter constructs assess mitophagy in a pH-biosensor manner, exploiting the acid labile properties of the GFP and DsRed fluorescent tags.

The former is sensitive to the low pH of the lysosomes, whereas DsRed is not, thus allowing mitophagy to be assessed by a change in colour, represented by DsRed-only mitochondria (McWilliams et al., 2016, Montava-Garriga and Ganley, 2020). Recent studies on Drosophila melanogaster showed that basal mitophagy can occur without PINK1 and Parkin suggesting a separate function for this pathway in the fruit fly system (Lee et al., 2018).

Mitophagy is a principal mechanism of mitochondrial quality control, eliminating aged and damaged mitochondria. Therefore, mitophagy is important for cellular homeostasis and cell survival because the maintenance of a balance between normal and damaged mitochondria is essential for efficient energy production in the cell (Hyttinen et al., 2018). Indeed, impaired mitophagy that leads to the accumulation of damaged mitochondria has been linked to a number of human pathologies in particular aging and age-related disorders such as neurodegenerative (Alzheimer's disease, Parkinson's disease), cardiovascular pathologies, cancer and AMD (Hyttinen et al., 2018, Chen et al., 2020).

1.2.4 Mitochondria are dynamic organelles

In order for mitochondria to travel to different sub-cellular locations, they are transported via the cytoskeleton and molecular motors (Shen et al., 2018). The best studied mechanism of mitochondria trafficking has been elucidated in neurons where long axonal branches allow easy tracking. Briefly, mitochondrial transport relies on microtubule-based motors, among which the key protein involved is the kinesin-1 family (KIF5). Two adaptor proteins, Miro

and Milton, found on the OMM link mitochondria to kinesin-1. Two Milton orthologues Trak1 and Trak2 (trafficking kinesin protein 1 and 2) are found in mammalian cells, with preferential binding of Trak1 to kinesin1 (Sheng, 2014).

Since mitochondria are the cell engines, they are often required by the cells to be at different sub-cellular locations depending on localised energy needs within the cells. Therefore, mitochondria display important intracellular mobility (Chan, 2006, Suarez-Rivero et al., 2016). The regulation of mitochondrial mobility must be fine-tuned in order to meet regular cell energy demands and to adapt in stress related responses. The processes of mitochondrial mobility are known as mitochondrial dynamics (Figure 1.4) (Boland et al., 2013).

Mitochondrial dynamics maintain homeostasis of the mitochondrial network. Mitochondrial fusion regulates the extent of mitochondria, where individual organelles are fused with one another creating denser networks. During this process OMMs merge, mediated by the activity of mitofusin 1 (Mfn1) and Mfn2 GTPases. Inner membranes (IMM) fusion is mediated by optic atrophy 1 (OPA1) GTPase. Fusion events can stimulate the maintenance of general mitochondrial support by exchanging mitochondrial DNA, respiration, Ca^{2+} oscillations and rescuing damaged parts of mitochondria. By contrast, fission is a dynamic process that gives rise to numerous smaller mitochondria, increasing the area of mitochondria spread inside the cell. Here, during mitochondrial division, dynamin-related protein-1 (Drp-1) is recruited to the OMM by another protein mitochondrial fission factor (MFF) (Eisner et al., 2018). Fission can enhance mitochondrial motility and it is required for the

mitochondrial clearance via mitophagy (Saito and Sadoshima, 2015, Li et al., 2018, Xian et al., 2019).

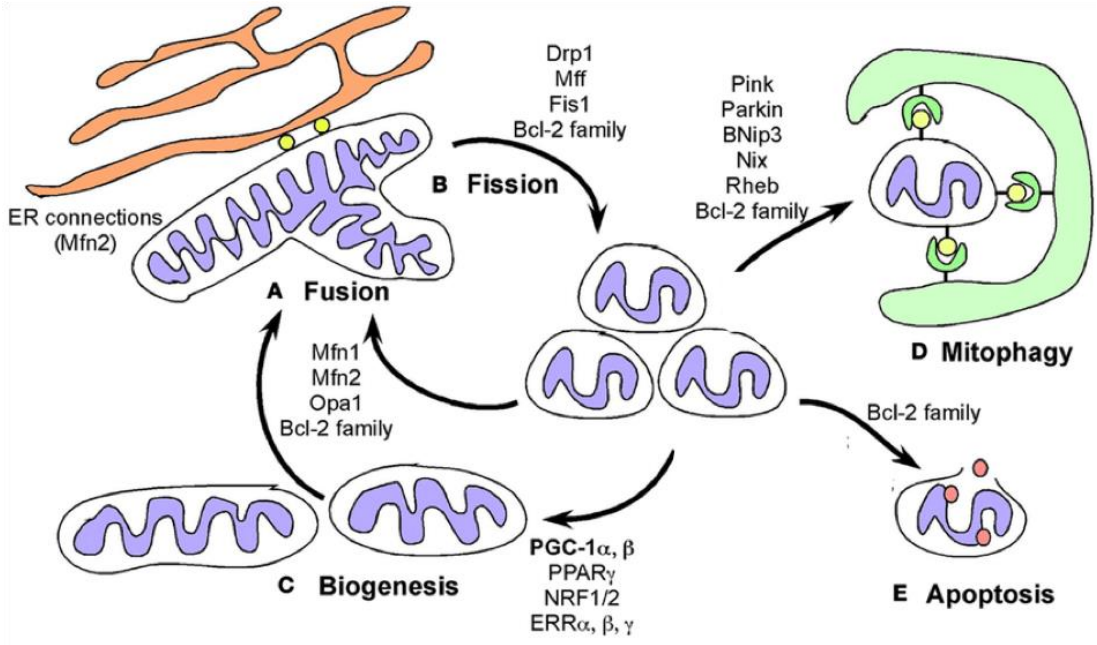

Figure 1.4 Mitochondrial dynamics. A) Mitochondrial fusion is important for the maintenance of healthy mitochondria. The process includes the action of a number of proteins found on the inner (i.e. OPA-1) and outer mitochondrial membrane (Mfn1,2). B) Mitochondrial fission is responsible for the clearance of damaged mitochondria. Fission is promoted by the GTPase activity of Dynamic-related protein (Drp-1). C) Biogenesis is induced by lack of nutrients and/or response to oxidative damage. Important transcription factor such as PGC-1a are strongly expressed. D) Mitophagy is a specific autophagy process available for mitochondria. It is switched on when mitochondria is fragmented and Pink1/Parkin complex plays an important role. E) Apoptosis of mitochondria occurs when cell death regulators are activated such as Bcl-2. Schematic is adopted from Boland et al 2013 (Boland et al., 2013).

Inter-organelle communication has been shown to participate in the regulation of mitochondrial dynamics. Therefore, mitochondrial networks depend on the interaction with other cellular organelles generating a complex regulatory machinery.

Normally, the interaction of ER with mitochondria is essential for calcium signalling and phospholipid synthesis. In 2011 Friedman et al found that the site of mitochondria division is directed by the ER, where the two organelles are found in a close contact. By using electron tomography and fluorescence microscopy, they showed that ER wraps around and constricts mitochondria to direct sites of fission (Friedman et al., 2011). Moreover, ER was found in contacts with mitochondria undergoing fission, in the absence of Drp1 and Mfn proteins, proteins important for conducting the fission reaction. This indicates the ER contact is a key step of the mitochondrial division (Klecker et al., 2014). Moreover, the actin cytoskeleton also participates in ER-associated mitochondrial fission. Here, actin polymerisation is governed by ER proteins, with subsequent recruitment of Drp1 and mitochondrial construction (Korobova et al., 2013).

In addition to being in contact with the ER, mitochondria also interact with the plasma membrane, although these connections are poorly understood (Klecker et al., 2014, Westermann, 2015). Recently, mitochondria-lysosome contacts sites were revealed to regulate mitochondrial fission. Interestingly, this interaction was shown to be bidirectional, where mitochondria were also found to regulate the RAB7 GTP hydrolysis, an essential process for lysosome dynamics (Wong et al., 2018). Therefore, it is clear that by physical association, membrane organelles support the functions of their neighbours, to coordinate their structures and unite their activities. This is essential for the maintenance of the eukaryotic architecture (Klecker et al., 2014).

1.3 ARMCX proteins

1.3.1 ARMCX structure and evolution

Armadillo repeat-containing genes located on the X chromosome (Armcx) are clustered within a small region on the X chromosome (region Xq21.33 – q22.3) and encode 6 proteins (Armcx1 – 6) plus one pseudo-protein (Simonin et al., 2004). This group of genes has not been studied extensively and thus further research is required to evaluate their significance. All Armcx members vary in length but possess a highly conserved carboxy (C)-terminus, which encodes an armadillo domain (Arm) and an uncharacterised sequence. Evolutionary ancient Arm domains consist of varying numbers of repeats of a 42 amino acid motif known to form alpha helices (Ozawa et al., 1995, Hatzfeld, 1999). The Arm repeat was first described in Drosophila as a protein important for segment polarity and later as a diverse platform for binding partners in eukaryotic cells. A classic example of arm-containing protein is beta-catenin, that is described as a multi-functional protein that acts as a "hub" of signalling mechanisms (Tewari et al., 2010). Indeed, proteins interacting with Armcx may do so by binding to the Arm domain (see below). The amino (N)-termini of Armcx are more variable in structure, and harbour a putative transmembrane domain, nuclear signal and mitochondrial targeting sequence (MTS) (Mou et al., 2009, Kusama et al., 2010).

An interesting fact is that Armcx are specific for Eutherian mammals of which placentalia are the only present members. The closest mammalian relatives are marsupials and monotremes, which only possess the putative ancestral

gene Armc10. Located on the 7th chromosome of the human genome, Armc10 is shown to be the closest gene to the Armcx cluster by phylogenetic analysis. Moreover, the Armc10 coding sequence contains multi-exons rather than a single one. This led to the suggestion that Armcx family arose by a duplication of the Armc10 ancestral gene, which occurred during the appearance of Eutheria (López-Doménech et al., 2012). Notably, it is not clear whether the evolution of Armc10 to Armcx constitutes divergence of Armc10 functions to multiple Armcx proteins or to novel functions.

1.3.2 ARMCX genes regulate mitochondria

In addition to describing the evolutionary history of the Armcx cluster, Lopez-Domenech et al have also examined the role of Armcx3 as a regulator of mitochondrial dynamics in neurons. Their investigations showed that Armcx3 overexpression causes mitochondrial aggregation and reduces trafficking along the axons (López-Doménech et al., 2012). Previously, mitochondrial aggregation has been perceived as a result of lack of function of Miro1, an essential protein for the assembly of the mitochondrial trafficking complex in neurones (Fransson et al., 2003). Notably, the aggregation of mitochondria caused by Armcx3 was Miro1 independent, suggesting a different mechanism(s) involved. Furthermore, these authors establish an interaction between Armcx3 and the mitochondrial trafficking complex Miro/Trak2/Kinesin. The interaction was abolished, once the Arm-containing domain was removed, indicating the importance for the domain. Notably, Miro-Trak2 complex interacts with Kinesin motors in a Ca^{2+} dependent manner. Indeed, the interaction between Armcx3 and Miro1 or Miro2 was shown to be

Ca^{2+} sensitive. Armcx3 was not shown to affect the speed of mitochondria, but fewer mobile mitochondria were observed. This suggests that Armcx3 is involved in mitochondria trafficking via interaction with the Kinesin/Miro1/Trak2 complex (López-Doménech et al., 2012). In addition, Armc10 was also found to play a role in mitochondrial dynamics and to interact with and to be phosphorylated by AMPK (Chen et al., 2019).

Furthermore, in a wide proximity proteomic study, Armcx3 and Armc10 were identified as Parkin substrates, whereas Armcx2 was found to be an OMM protein (Heo et al., 2019). In addition, Armc10 was previously found to be ubiquitylated by Parkin in depolarised Hela cells in a large proteomic study (Serrat et al., 2013). This proteomic data implicates the Armcx family in the process of mitochondrial degradation. However, currently there are no studies on Armcx in mitophagy regulation.

1.3.3 Other ARMCX associated functions

The members of the Armcx family were first described as tumour suppressors known as Arm-containing protein lost in epithelial cancers linked to X-chromosome (Alex). Expression of Armcx1 and 2 is either strongly reduced or lost in human cancer affecting the epithelial tissue of ovaries, prostate, colon, pancreas and lungs. However, in cells of tumours such as neuroblastomas and gliomas, Armcx1 and 2 expression is unaltered (Kurochkin et al., 2001). Suppression of gene expression in colorectal cancer may occur through promoter methylation. Notably, the overexpression of Armcx1 also suppresses colony formation of human colorectal carcinoma cell line (Iseki et al., 2012).

Moreover, a recent study has investigated the ARMCX expression levels to be potential prognostic markers for gastric carcinomas (Wang et al., 2020).

Armcx is found in a wide variety of tissue. Armcx1-5 are strongly expressed in the heart, brain, spleen, pancreas, testis, ovaries, prostate and colon, whereas Armcx 6 is mostly seen in the pancreas and spleen. In contrast, Armcx expression is absent in leukocytes (Kurochkin et al., 2001, Kusama et al., 2010). Given the fact that the leukocytes are cells without structural polarity, Armcx may be important for cell polarity and differentiation. In this context, Armcx3 was shown to be regulated by Wnt5a signalling in epithelial cells (Serrat et al., 2013), a signalling cascade which is also important for RPE differentiation (Kim et al., 2015). Furthermore, about 10 years ago, a yeast two-hybrid protein-protein interaction screen revealed Armcx3 as a binding partner of Sox10 (Mou et al., 2009). This important developmental transcription factor is a regulator of cellular fates. Sox10 interacts with many cellular proteins and is found to shuttle between the nucleus and cytoplasm (Rehberg et al., 2002). Moreover, Mou et al showed that Armcx3 localises to the outer mitochondrial membrane in a mouse neuronal cell line (neuro2A). Further work revealed the existence of a potential crosstalk between mitochondria and nucleus, where Armcx3 overexpression influences Sox10 export from the nucleus and subsequent accumulation on mitochondria (Mou et al., 2009).

Although there is evidence of Armcx functions in mitochondrial dynamics, cell differentiation and polarity and most recently mitophagy, more research is needed in order to understand better their physiological purpose.

1.4 Hypothesis and aims

Hypothesis – 1) Armcx proteins contribute to maintaining a healthy mitochondrial network in RPE, and 2) Armcx have evolved to cover diverse function in mitochondrial regulation

To test this hypothesis, we will pursue the following aims:

i. Establish the expression profile and sub-localisation of selected Armcx in ARPE-19 cells and the RPE *in situ*

ii. Study the mitochondrial phenotype and mitochondrial dynamics in ARPE-19 cells following over- or underexpression of selected Armcx proteins

iii. Investigate the role of selected Armcx protein in Parkin-dependent mitophagy

iv. Investigate functional compensation using ancestral Armc10

Chapter 2 Materials and Methods

2.1 Materials

2.1.1 General Materials

General reagents used in this project were purchased from Sigma-Aldrick Company Ltd. (Poole, Dorset, UK) unless otherwise described in the following sections.

2.1.1.1 Plasmids and short interfering RNA

Human ARMCXs full-length cDNA IMAGE clones were inserted in pEGFP-N1 plasmid vectors by the master student Mrs Ming-Min Yang (Yang, 2013). mCherry-Parkin plasmid was purchased from Addgene, US (reference number 23956). MitoDSRed plasmid was kindly provided by Prof Michael Duchen from the Department of Cell and Developmental Biology at UCL. Gene block of Marsupial ARMC10 cDNA was purchased from Integrated DNA technology (Integrated DNA Technologies, BVBA, Belgium). Short interfering (si) RNA oligonucleotides for Armcx1, Armcx 2 and a non-targeting control were purchased from Dharmacon, UK (Table 2.1).

Table 2.1 siRNA oligonucleotides list

siRNA	Company	Reference
ON-TARGETplus Human ARMCX1 (51309) siRNA - Set of 4	Dharmacon	LQ-013198-02-0002
ON-TARGETplus Human ARMCX2 (9823) siRNA - Set of 4	Dharmacon	LQ-010936-01-0002
ON-TARGETplus Non-targeting Pool	Dharmacon	D-001810-10-05

2.1.2 General Solutions

Milli-Q reagent grade water from Milipore was used for all cell and tissue related experiments, and molecular biology water (Sigma-Aldrich Merck Company Ltd. Poole, Dorset, UK) was used for molecular cloning. Phosphate Buffered Saline (PBS) 10x solution (Fisher Scientific UK, Loughborough, UK) was used to prepare 1x PBS which was used in the lab, except for cell culture needs.

2.1.3 Cell culture reagents

2.1.3.1 General

Plastic tissue culture vessels used in this project were purchased from Nunc (Thermo Fisher Scientific, Loughborough, UK) unless otherwise described in the methods below. Dulbecco's PBS without Ca^{2+} and Mg^{2+}, penicillin-streptomycin, fetal calf serum (FCS; heat inactivated, European origin), fetal

bovine serum (FBS; certified, US origin), Dulbecco's modified eagle's medium (DMEM; high glucose, pyruvate) were all purchased from Thermo Fisher Scientific (Pairlsey, UK). Trypsin (from porcine pancreas) were purchased from Sigma-Aldrich.

2.1.3.2 Transfection

Lipofectamine™ 2000 transfection reagent, Lipofectamine RNAiMAX reagent and Opti-MEM™ I reduced serum medium (1x) were purchased from Thermo Fisher Scientific (Loughborough, UK).

2.1.3.3 Live imaging and mitochondrial staining

Uncoated 50mm dishes with 14mm glass diameter were used for live cell imaging ordered from MatTek (Ashland, MA USA). DMEM supplemented with high glucose and no phenol red was purchased from Thermo Fisher Scientific (Pairlsey, UK). Mito Tracker Orange CMTMRos was ordered from ThermoFisher Scientific. Carbonyl cyanide m-chlorophenylhydrazone (CCCP) was ordered from Sigma-Aldrich (Dorset, UK).

2.1.4 Molecular Cloning reagents

Q5 Site-Directed Mutagenesis Kit was purchased from New England Biolabs, UK. Ampicillin and kanamycin antibiotics were purchased from Sigma-Aldrich. EndoFree Plasmid Maxi kit from Qiagen. Monarch® DNA Gel Extraction kit was purchased from New England Biolabs, UK. 1kb DNA ladder was purchased from Thermo Fisher Scientific (Loughborough, UK). All restriction

enzymes used were from either Roche or New England Biolabs (Hertfordshire, UK). RedSafe™ Nucleic Acid Staining Solution (20,000x, from iNtRON Biotechnology, Rickmansworth, UK) Primers were purchased from Eurofins Genomic, UK and their sequences are displayed on Table 2.2. NEB 5-alpha Competent E. coli cells (High Efficiency) supplied with SOC outgrow media were ordered from New England Biolabs for cloning experiments. DH5-alpha competent cells were kindly provided by Prof Karl Matter from the Institute of Ophthalmology, UCL for sub-cloning and transformations when re-making plasmids. RedSafeTM Nucleic acid staining solution was ordered from iNtRON Biotechnology (Rickmansworth, UK). Alkaline phosphatase and Shrimp Alkaline Phosphatase (SAP), T4 DNA ligase were purchased from Roche Diagnostics (Mannheim, Germany).

Table 2.2 Primers used for site-directed mutagenesis

Name	Primer sequence (5' – 3')	Tm (C^0)	GC-content
Armcx1_F	CTGGTGGTGAAAGTAAAAG (19)	52.4	42.1%
Armcx1_R	AGGAAAGTTGAACTTGCC (18)	51.4	44.4%
Armcx2_F	CTAGTGAACAAATTCTGATTGGTTATGT ACC (31)	62.9	35.5%
Armcx2_R	GGAAAGGGGCGCTTCTGC (18)	60.5	66.7%
Armcx3_F	AAATTCATGGCCAAACTTGC (20)	53.2	40%
Armcx3_R	GGAAGCCCGTTTCTGGAC (18)	58.2	61.1%
Armcx6_F	GAAACCCCTGCCCCATAA (18)	56.0	55.6%
Armcx6_R	ACTGCCATTTTTACAATTTTGAGC (24)	55.9	33.3%

2.1.5 Western Blot reagents

Tris-Glycine-SDS PAGE (10X) (running) and Tris-Glycine Electroblotting (10X) (transfer) buffers were purchased from National Diagnostics Atlanta, US. Immobilon Polyvinylidene difluoride (PVDF) membranes (0.45 µm) were purchased from Milipore. Spectra™ Multicolor Broad Range Protein Ladder was purchased from Thermo Fisher Scientific (Loughborough, UK). Skim milk powder was purchased from Sigma-Aldrich (Germany). Lumi-Light Western

Blotting substrate was purchased from Roche (Mannheim, Germany). Enhanced chemiluminescence (ECL) anti-mouse and anti-rabbit horse radish peroxidase (HRP) conjugated antibodies were purchased from GE Healthcare. X-ray films were ordered from FujiFilm.

2.1.6 Immunohistochemistry reagents

All primary antibodies are listed in Table 2.3 and all secondary antibodies used in this project are listed in Table 2.4. Bovine Serum Albumin (BSA) was purchased from Simga-Aldrich. Mounting Medium with DAPI - Aqueous, Fluoroshield was purchased from abcam (Cambrdige, UK).

Table 2.3 Primary antibodies

Antigen	Antibody	Dilution	Cat number	Manifacturer
Armcx1	Rabbit anti-human/mouse/rat	1:100	SAB2100153	Sigma-Aldrich
Armcx2	Rabbit anti-human/mouse/rat	1:100	12200-1-AP	Proteintech
Armcx3	Rabbit anti-human/mouse/rat	1:100	Ab136061	Abcam
Amrcx6	Rabbit anti-human	1:100	HPA043030	Atlas antibodies
Tom20 (F-10)	Mouse anti-human	1:100	sc-17764	Santa-Cruz
Lamp2	Mouse anti-human	1:100	Sc-18822	Santa-Cruz
RPE65	Mouse anti-human/mouse/rat	1:1000	295957	EMD Milipore
LC3I/II (D3U4C)	Rabbit anti-human/mouse/rat	1:100	12741S	Cell Signalling

Table 2.4 Secondary antibodies

Host species	Target species	Fluorochrome	Dilution	Cat number	Manifacturer
Donkey	Mouse	Alexa Flour™ 488	1:200	A21202	Thermo Fisher Scientific
Donkey	Rabbit	Alexa Flour™ 488	1:200	A21206	Thermo Fisher Scientific
Goat	Mouse	Alexa Flour™ 555	1:200	A21424	Thermo Fisher Scientific
Goat	Rabbit	Alexa Flour™ 555	1:200	A21429	Thermo Fisher Scientific
Donkey	Mouse	Alexa Flour™ 647	1:200	A31571	Thermo Fisher Scientific
Donkey	Rabbit	Alexa Flour™ 647	1:200	A31573	Thermo Fisher Scientific

2.1.6.1 Human tissue staining

Hellendahl jars were purchased from Pyramid Innovation Ltd (UK). Xylene for histological use was from Sigma-Aldrich. Potassium permangantate was order from Amertek, (Farnborough, UK). Oxalic acid was purchased from Sigma-Aldrich. Immedge-hydrophobic barrier pen was purchased from Vectorlabs (US). Leica BONDTM Plus Slides were ordered from Leica (US).

2.1.7 Electron microscopy (EM) reagents

All EM related reagents were kindly provided by Dr Emily Eden from the Institute of Ophthalmology at UCL.

2.2 Methods

2.2.1 Bioinformatics

Armcx sequences were obtained from the National Centre for Biotechnology Information (NCBI) database (Table 9.1 in Appendix). The phylogenetic tree was generated using PhyML (default model) by the master student Alice Kirby (Kirby, 2016). The annotated tree with a presence/absence matrix and the genetic tree circle were constructed from the conserved armadillo repeat part of each gene by using the Orthologous Matrix (OMA) identifier (Roth et al., 2008). This was done with the help of Dr Christophe Dessimoz and his team from the Department of Genetics, Evolution and Environment at UCL. Multiple sequence alignments were generated using MUSCLE (Multiple Sequence Comparison by Log-Expectation) (EMBL-EBI). The putative structural domains within Armc10/Armcx family members from protein sequence information obtained from the UniProt Knowledgebase/Swiss-Prot (UniProtKB/Swiss-Prot) (Boutet et al., 2007). MitoFates was used to verify mitochondrial targeting sequences (Fukasawa et al., 2015). The post-translational modified sites of Armcx were acquired from PhosphositePlus by Cell Signalling Technology (Hornbeck et al., 2015).

2.2.2 Molecular Biology

2.2.2.1 Site-directed Mutagenesis

In order to introduce deletions in Armcx genes, polymerase chain reaction (PCR) based mutagenesis was carried out by using site-directed mutagenesis kit. The exponential amplification was performed in 25 µl volume consisting of

1x Hot Start High-Fidelity 2x Master Mix, which contained the Hot Start High-Fidelity DNA Polymerase (12.5 ul), 1 µM of primers (1.25 µl each), 10 ng of DNA plasmid (1 µl) and the rest of the volume was reached with nuclease-free water (9 µl). The PCR cycle parameters were set up as per manufacturer instructions and respectful of the annealing temperatures of the primers. Amplification was carried out in an Eppendorf Mastercycler gradient starting with 98°C for 30 s for the initial denaturation step, then 25 cycles of primers annealing step at 98°C for 30 s, 50°C for 10 s, 72°C for 3 min and final extension at 72°C for 2 min and then they were hold at 4°C.

Subsequently, 1 µl of the PCR products was mixed with the 2x KLD reaction buffer (5 µl), 10x enzyme mix (1 µl) and nuclease-free water (3 µl) in 10 µl volume at 1x final concentration. This mix contained Kinase, Ligase and DpnI enzymes, which allow phosphorylation, ligation and removing template plasmids, respectively. The mixture was incubated at room temperature for 5 min. Next, 5 µl of the KLD mix was added to NEB 5-alpha Competent E. coli cells which were thawed on ice in advance. The cells were incubated on ice for 30 min, heat shocked for 42 s and then returned on ice for 5 min. Approximately, 950 µl of SOC outgrow media warmed at room temperature was added to the cell mixture for 1 h incubation at 37°C. Lastly, 50 µl of the reaction mixture was spread on a Luria broth (LB) agar plate containing the appropriate antibiotic for selection and returned to the 37°C incubator overnight. On the following day transformation efficiency was determined by counting the number of colonies. Appropriate positive and negative controls were used as provided by the manufacturer. At least ten colonies were picked

from each mutagenesis reaction and were cultured in 3 ml volume of LB media containing appropriate antibiotic and incubated in 37°C shaker at 225 rpm overnight. In the next morning bacterial colonies were pelleted by 1 minute centrifugation and small amount of DNA plasmid was purified (mini-prep kit) (see below).

2.2.2.2 DNA sequencing

The sequences that contained the deleted Armcx regions were all verified by DNA sequencing (Source Bioscience; Cambridge) and subsequently were cloned into the ArmcxGFP-N1 plasmids. The sequence traces were analysed by Chromas Lite software and by comparison with the original sequences obtained from NCBI.

2.2.2.3 Restriction enzyme digest

Verified Armcx mutants and the wt ArmcxGFP-N1 vectors were digested with specific for each plasmid restriction enzymes in the following reaction. Each plasmid DNA was digested in 20 µl volume containing 1 µg of DNA, 2 µl appropriate 10X buffer, 0.1 µl of restriction enzymes and sterile distilled water. Samples were incubated for digestion for 1 to 2 h at 37°C, and the products were subsequently analysed using agarose gel electrophoresis.

2.2.2.4 Agarose gel electrophoresis

According to the molecular weight, DNA fragments were separated by agarose gel electrophoresis. For the gel preparation, 1 g of agarose was melted in 100 ml 1X TAE Buffer (40mM Tris. acetate, 2mM EDTA, from National Diagnostics, Leicestershire, UK) and 2.5 µl of nucleic acid staining solution was added to

the mixture once the temperature was around 35°C. The gel solution was poured in an appropriate size tray fitted with combs and left for an h to solidify at room temperature. Before proceeding to electrophoresis, DNA samples were prepared with the addition of 0.2 volume (4 µl) of 6X loading dye (30% glycerol (w/v), 0.25% xylene cyanol) to 20 µl of restriction enzyme digest mixture. The DNA samples (20 µl), along with 1Kb DNA ladder (12 µl), were then loaded to the wells of the gel and electrophoresed in 1X TAE Buffer at 120-140 V until the fragments were clearly separated. The gel was scanned under long-wavelength ultraviolet (UV) transillumination DR-45M for a short time to minimize the risk of DNA degradation. The appropriate band sizes were cut with a clean sharp scalpel and put into microcentrifuge tubes for DNA gel extraction.

In other cases of gel electrophoresis, gels were scanned under ultraviolet transillumination (Gene Genius Bio Imagine System Syngene, Cambrdige, UK) for visualisation and analysis.

2.2.2.5 Gel extraction

The QIAquick gel extraction kit was used to purify the DNA fragments from the agarose gel. The gel slices were weighted in the tubes, mixed with buffer QG (3 to 1 volume of the gel, i.e., 300 µl = 100 mg) and incubated at 50°C for 10 min until the gel dissolved completely. One volume of isopropanol was added to the samples and mixed well to increase the yield of DNA extraction. Subsequently, the mixture was added to the QIAquick spin column in a 2 ml collection tube and centrifuged at 16000xg for 1 minute. The flow-through was discarded and the column was span again after being washed with 500 µl of

Buffer QG. The column was further washed with 750 µl of Buffer PE and the flow was discarded after another centrifugation. In order to remove any excess of the last wash, the column was centrifuged at 16000xg for 1 minute. The column then was transferred to a clean microcentrifuge tube and the DNA was eluded by adding 10 µl of Buffer EB and centrifuged for 1 minute.

2.2.2.6 Ligation

Prior ligation, the open DNA vector was dephosphorylated with Alkaline Phosphatase in order to prevent self-ligation of the vector. The protocol was carried out according to the protocol for dephosphorylation of 5' – ends in restriction enzyme reaction. Briefly, following a restriction enzyme digest, 1 unit (1 µl) of Shrimp Alkaline Phosphatase (SAP) was added to the restriction digest for 1 h at 37°C. The enzyme reaction was stopped by heat inactivation for 15 min at 65°C. Subsequently, the process of ligation of DNA in a plasmid vector was carried out using T4 DNA Ligase (1 unit/µl) according to the manufacturer's instructions. The molar ratio of vector DNA to insert DNA in a standard ligation reaction was set to be 1:5. The reaction volume was set to be 10 µl and consisted of 1 µl T4 DNA Ligase, 1 µl 10X Ligation Buffer, appropriate amounts of respective insert DNA, vector DNA and sterile distilled water. After overnight incubation at 4°C, the ligation reaction mixture was used directly for transformation of competent cells. A negative control was also set up, where only the plasmid DNA was ligated without an insert, in order to estimate the vector self-ligation rate.

2.2.2.7 Transformation

Each transformation was carried out using 50 µl aliquot of thawed NEB 5-alpha Competent E. coli cells (High Efficiency). Ligation reactions were then added to the cells and incubated on ice for 30 min. This was followed by a 45 s heat shock at 42°C and 3 min incubation on ice. Next, 1 ml of SOC media (supplied by the Site-directed mutagenesis kit) was added to the cell-DNA mixture and incubated at 37°C for 1 h. Two different dilutions (10 ul and 100 µl) were spread onto LB agar plates containing appropriate antibiotic for selection and returned back to the 37°C incubator for an overnight incubation. On the next day, transformation efficiency was determined by counting the number of colonies and the plates were placed back at 4°C to prevent further growth. Large single colonies were picked and cultured in 3 ml of LB medium containing antibiotics and left to grow overnight in a shaking incubator at 37°C.

2.2.2.8 Small scale of plasmid DNA purification (mini-prep)

For analytical purposes, a small scale isolation of plasmid DNA from bacteria culture was carried out using GenEluteTM Plasmid Miniprep Kit (Sigma) as per manufacturer instructions.

Briefly, 1.5 ml of the total 3 ml LB medium overnight culture was pelleted by 1 minute centrifugation. After a complete resuspension of the pellet in 200 µl Resuspension Solution containing RNase, 200 µl Lysis Solution was added and mixed by gently inverting the tube 6 to 8 times. Cell debris were then precipitated by adding 350 µl of Neutralization Solution with the tube once again being gently inverted 4 to 6 times and centrifuged for 10 min. During this time, a GenElute Miniprep Binding Column was prepared by adding 500 µl of

Column Preparation Solution and centrifuged for 1 min to maximize the membrane DNA binding efficiency. The cleared lysate was then transferred to the prepared Binding Column and centrifuged for 1 min to allow the binding of DNA. Following a wash with 750 µl of wash solution and 1 min centrifugation, another further 1 min centrifugation was done to remove any excess of ethanol. The DNA elution was carried out using 100 µl Elution Solution followed by 1 minute of centrifugation. Note, all centrifugation steps were carried out at 12,000xg with flow-through discarded and new collection tubes replaced when necessary. Eluted DNA was used immediately or stored at -20°C.

2.2.2.9 Large scale of plasmid DNA purification (maxi-prep)

To prepare transfection grade plasmid DNA, the EndoFree Plasmid Maxi Kit (Qiagen) was used based on a modified alkaline lysis procedure. A pre-culture from a single bacteria colony was prepared first in 3 ml small volume LB medium containing appropriate antibiotic for 6 h at 37°C shaker of 225 rpm during the day. Subsequently, 120 µl of the pre-culture was diluted in 120 ml of LB medium containing appropriate antibiotic and was left to grow overnight at 37°C shaker of 225 rpm. Bacterial culture was harvested on the next day by centrifugation at 4°C for 15 mintes and the bacterial pellet was completely resuspended in 10 ml of cold Buffer P1 supplemented with RNAseA and LyseBlue colour indicator. The bacterial lysate was next mixed with 10 ml of Buffer P2, inverted gently 6 times and left for 5 min at room temperature. The mixture turned viscous and blue indicating an optimal buffer mixing. Following the incubation, 10 ml of pre-chilled Buffer P3 was added to the mixture to

neutralize the lysis reaction and the tube was inverted gently 6 times. Once the mixture appeared colourless and less viscous it was poured into the QIAfilter cartridge barrel and left at room temperature for 10 min. After the incubation the cell lysate was filtered into a 50 ml falcon tube and mixed with 2.5 ml of Buffer ER and incubated for 30 min on ice. During this time, 10 ml of Buffer QBT was added to QIAGEN-tips to equilibrate them. The filtered lysates were then passed through the tips by gravity flow. The tips were then washed twice with 30 ml of Buffer QC and finally the DNA was eluted with 15 ml of Buffer QN into endotoxin free tubes. The eluted DNA was mixed with 0.7 volume of isopropanol and centrifuged for 30 min at 4°C at 8,000xg speed. Following the spin, the supernatant was carefully discarded not to disturb the DNA pellet. The latter was then washed with 2.5 ml of endotoxin free 70% ethanol and return to the centrifuge for a further 10 min spin. The DNA pellet was then left to dry for maximum 15 min and redissolved in 200 µl Buffer TE. The concentration of the plasmid DNA was determined using Nanodrop spectrophotometer. 10 µg of plasmid DNA aliquots were stored in 2.5 volumes of 100 % ethanol and 0.1 volume of 3M sodium acetate, at 4°C.

2.2.3 Molecular Cloning of ARMC10

Codon optimisation of the open reading frame of Armc10 marsupial was done to surmount the differences of codon usage by different species. Here, since we aimed to introduce the marsupial Armc10 in human cell line, the Armc10 codon sequence was optimised towards human codon preferences. This was done via Integrated DNA technology software (Technologies). Subsequently, gene blocks of Marsupial ARMC10 cDNA were designed with 5’ XhoI and 3’

BamHI restriction enzyme sites for subcloning into the pEGFP-N1 plasmid. The gene block was ordered as a double-stranded gene fragment from IDT Integrated DNA Technologies, BVBA (Belgium). Firstly, the dry gene block was resuspended in 18 µl of water and spin down at maximum speed for 1 minute. Before proceeding towards restriction digestion, 17 µl of the gene block was heated at 55°C for 5 min. For the restriction digest was used 17 µl of the gene block in 20 µl volume reaction, including 2 µl 10x appropriate restriction buffer and 1 µl restriction enzyme (0.5 µl each). The process of restriction digest is the same as explained in section 2.2.2.3. Similarly, to the cloning of the mutant Armcx sequences, the ARMC10 gene block was cloned into the pEGFP-N1 plasmid following the steps explained from section 2.2.2.4 to 2.2.2.9.

2.2.4 Cell culture

Immortalised ARPE-19 human RPE cells were maintained in high glucose (4.5 g/L), pyruvate, DMEM supplemented with 10% FCS, 1% Penicillin/Streptomycin at 37°C and 5% CO_2. ARPE-19 cell cultures were used between passages 25-38. In this study, cells were seeded onto 35mm dishes unless otherwise stated. Differentiation of ARPE-19 was carried out as previously reported (Ahmado et al., 2011) and assessed by the appearance of pigmentation and cobblestone-like cell layer (Figure 2.1). Cells were seeded at a density of 1.5 x 105 cells/cm2 in the maintenance medium. Once the cells reached 90% confluency, they were washed in 1 x PBS and further cultured in differentiated medium (high glucose, pyruvate, DMEM supplemented with 1% FCS). Differentiation media was changed once per week.

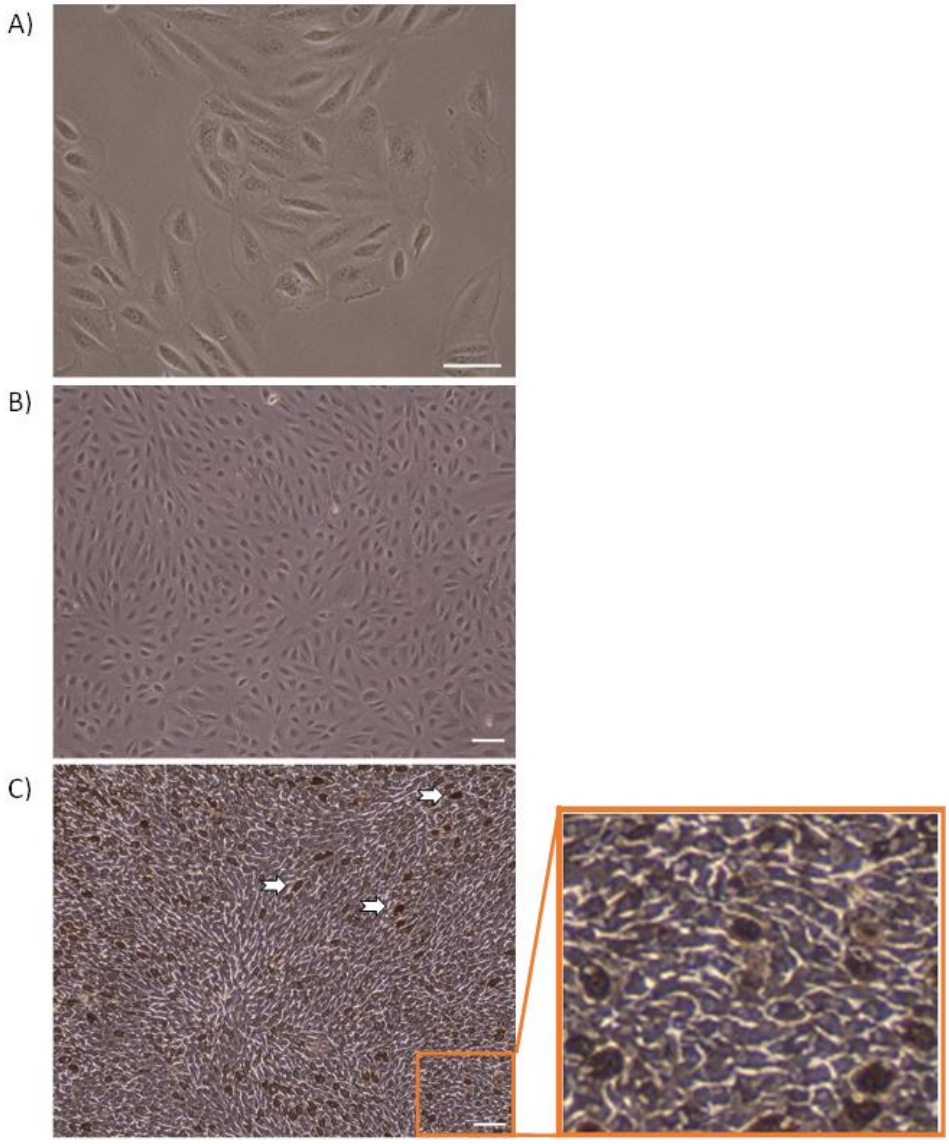

Figure 2.1 D MEM/Pyruvate-mediated differentiation of ARPE-19 cell line. **A)** panel represents non-differentiated, subconfluent cells lacking pigmentation with elongated and fibroblastic morphology; live cell images were taken by Leica DMIL microscope 40x objective; scale bar 100 µm **B)** panel shows non-differentiation confluent cells with lack of pigmentation **C)** panel displays >30 weeks post-differentiated cells with detectable pigmentation (white arrows) and cobblestone-like appearance (zoomed part); B) and C) images were taken by Leica DMIL 10x objectives; scale bar 100 µm.

2.2.5 Plasmid Transfection

ARPE-19 cells were seeded at a density of 1 x 105 cells/cm2 one day prior transfection. A few h prior transfection, cells were cultured in DMEM only

media without FCS and antibiotics. Lipofectamine™ 2000 was left at room temperature for 15 – 20 min prior transfection. Briefly, 1 µg plasmid DNA was diluted into 250 µL of Opti-MEM medium and in a separate tube the lipofectamine was diluted into 250 µL of Opti-MEM medium and both mixtures were incubated for 5 min at room temperature. The DNA mixture was then added to the lipofectamine and the tube was flicked a few times with a finger, then vortexed briefly and spun down quickly. An incubation of 20 maximum 25 min at room temperature was given for the DNA-cationic lipid complex to be formed. The DNA-Lipofectamine mixture was added to the cells dropwise, while the dish was gently swirled. Cells were placed back to the humidified incubator for another 24-48 h prior analysing expression. Six h post-transfection, cells were supplemented with 10% FCS to stimulate growth.

2.2.6 siRNA Transfection

Similarly, to the plasmid transfection, ARPE-19 cells were seeded one day prior transfection. The Lipofectamine™ RNAiMAX transfection reagent was used to transfect siRNA against Armcx1 and 2 and non-targeting siRNA sequence. The transfection reagent was warmed at room temperature for 30 min before transfection. In tube 1, 25 µM siRNA (2.5 µl) was added to 200 µl of OptiMEM media and in another tube (2) 5 µl of RNAiMax was diluted in OptiMEM. Subsequently, mix tube 2 into tube 1 and incubate at room temperature for no more than 20 min. Cell culture media was changed to media without antibiotics. Following the incubation, the siRNA mixture was added dropwise to the cells for at least 24h incubation at 37°C humidified CO_2 incubator and then changed to culture medium.

2.2.7 Mitochondrial staining and CCCP treatment

ARPE-19 cells were incubated with 100 nM Mito Tracker Orange CMTMRos for 40 min at 37°C prior fixation. In order to induce mitochondrial depolarisation, ARPE-19 cells were pre-treated with 20 µM of the uncoupler carbonyl cyanide m-chlorophenylhydrazone (CCCP, diluted in DMSO) for 3, 6 or 24 h.

2.2.8 Immunofluorescence

Prior cell fixation, ARPE-19 cells were washed briefly in 1 x PBS. Cells were fixed in -20°C methanol. Methanol fixed cells were further incubated for 5 min in a freezer. Then methanol was diluted out with 1 x PBS and replaced with blocking buffer (1% BSA in 0.05% Sodium Azide in 1 x PBS). Alternatively, 3.7% formaldehyde in 1 x PBS was added to the cells for 15 min at room temperature. Cells were permeabilized with ice cold acetone for a few s and then washed with 1 x PBS. Then cells were incubated in the blocking buffer for 1 h at room temperature. A dry ring was formed with a folded tissue around the central patch of cells in the 35mm dishes. Antibodies were diluted in blocking buffer and volume of 95 µl was added to the central patch of cells and the dishes were incubated at 37°C for 1 h. Dishes were then washed in 1 x PBS three times for 10 min and then incubated with secondary antibody (1:200 dilution) in blocking buffer for 1 h at 37°C. Dishes were then washed three times for 10 min with 1 x PBS and one time with water. Then, they were mounted with mounting media containing DAPI and coverslips were carefully

placed on top of the cells. At the end, dishes were left to dry for h/overnight and sealed with a transparent nail polish and stored in dark at 4°C.

2.2.9 SDS-PAGE and Western Blot

Cell lysates were prepared as previously described (Turowski et al., 2008). Briefly, cells were washed in 1 x PBS, then any residual liquid was aspirated and cells were lysed with 100 µl 2x lysis buffer (20% glycerol, 8% SDS) containing 1mM DTT. The cell lysates were scrapped and collected in microcentrofuge tubes. Genomic DNA was sheared by syringing the lysates 5 times through a 26G needle. Before separating the proteins on a SDS-polyacrylamide gel, samples were boiled for 10 min at 95°C and centrifuged for 10 min at 10,000 x g. Samples were either proceed to gel electrophoresis or stored at -20°C.

Separating and stacking gels were prepared according to the recipes in Table 2.3. The wells of the gel were washed with running buffer after being assembled within the gel tank system. The molecular marker was loaded (15 µl). Before loading the cell lysates, they were boiled again (if they were frozen) and centrifuged as described above. Electrophoresis was performed at constant amperage of 25 mA through the stacking gel and 50 mA through the separating gel.

Table 2.5 Separating & stacking gels recipes for 7.5%, 10% and 12% gels.

Separating gel 2x	**Stacking gel 2x**

	7.5% (80 kDa)	**10%** (55 kDa)	**12%** (35 kDa)		
Acrylamide	2.5 ml	3.34 ml	4 ml	**Acrylamide**	0.75 ml
1.5 M Tris pH 8.8	2.5 ml	2.5 ml	2.5 ml	**1M Tris pH 6.8**	0.63 ml
Water	4.85 ml	4 ml	3.35 ml	**Water**	3.4 ml
10% SDS	100 µl	100 µl	100 µl	**10% SDS**	50 µl
10% APS	80 µl	80 µl	80 µl	**10% APS**	75 µl
TEMED	4 µl	4 µl	4 µl	**TEMED**	10 µl

KEY: SDS - Sodium dodecyl sulfate; APS - Ammonium persulfate; TEMED - N′-Tetramethyl ethylenediamine

Proteins from the gel were then transferred onto Immobilon membranes using a semi-dry transfer cell (Bio-Rad). First, PVDF membranes were pre-wetted by 15 s of incubation in 100% methanol. The membranes were then washed in water and put in transfer buffer to equilibrate. The transfer is assembled by layering 5 sheets of filter papers soaked in transfer buffer, followed by a membrane, then the gel and finally another 5 sheets of filter papers soaked in transfer buffer placed on top. Any bubbles between the layers were squeezed out using a glass stripette. The transfer was run for 90 min at a constant 12V. Once the transfer was complete, amido black staining solution (40% ethanol, 10% acetic acid, 0.1% (w/v) amido black) was applied to the membranes for a few s and then removed by methanol and then water and finally in 1 x TBS. Membranes were left to dry between filter papers for at least 40 min.

Prior immunoblotting, membranes were blocked in 5 % milk in Tris-Buffer Saline (1xTBS) for two h at room temperature. Depending on the primary antibody, different dilutions were used (see Table 2.3). For the immunoblotting of Armcx2 another antibody was used – Abcam (cat number: ab199170) with 1:500 dilution. All primary antibodies were diluted in 1 x TBS-Tween (0.1%) in 1 x PBS and incubated overnight at 4°C. On the next day, membranes were washed first in TBS-Tween solution for 10 min twice, and once with 1 x PBS-Tween (0.1%). Secondary antibodies were diluted 1:500 in PBS-Tween and added to the membranes for 2 h at room temperature. Following secondary antibody incubation, the membranes were first washed twice in PBS-Tween, then once in TBS-Tween and a final wash in TBS. Enhanced chemiluminescence (ECL) was detected with Lumi-Light western blotting substrate solutions (1:1 ratio) and added to the membrane for 5 min at room temperature. Any excess of the ECL was removed and the membranes were put into cassettes and brought to a dark room where images were acquired using X-ray films and developed.

2.2.10 Life-Cell Imaging

ARPE-19 cells were seed in 50mm dishes with 14mm glass bottom one day before transfection with MitoDSRed plasmid. As described in section 2.2.5 cells were transfected with 1 µg of plasmid and after 24 h, cells were washed in PBS and cultured in DMEM medium with no phenol red. Short videos of the cells were taken using a Nikon Eclipse Ti-E with a 37°C microscope chamber. The system was set up at least two h before imaging for the chamber to warm up. Dishes were left in the chamber to equilibrate for 30 min before imaging.

Time-lapse microscopy was carried out for 10 min with 1 min intervals using the 63x oil objective. Videos and stills were edited by using ImageJ software. The Manual Tracking plugin (Fabrice cordelieres) was used to track the movement of individual mitochondria.

2.2.11 Human Tissue Processing and Staining

2.2.11.1 Donor Tissue Information

Human post-mortem eyes were provided by the Moorfields Eye Biobank (London, UK). Institutional Review Board (IRB)/Ethics Committee approval for postmortem eye tissue collection and storage at the UCL Institute of Ophthalmology was in place. Paraffin-embedded human eye tissues were provided kindly by Prof Marcus Fruttiger. Donor tissue and fixation information is provided in table 2.

Table 2.6 Human eye donor tissue information.

Age	Gender	Cause of death	Fixation delay (h)	Medical history
82	F	intracranial haemorrhage	10	None
83	M	high servical spine injury	16	AMD, dementia

KEY: F – Female; M – Male; AMD – Age-related macular degeneration

2.2.11.2 Paraffin-embedded tissue sectioning

Paraffin-embedded eye tissue was sectioned at 6 µm thickness by using an Anglia AS200 sledge microtome (Cambridge, England). Thin slices were then floated on a 50-55°C bath in distilled water. In order to remove creases, drop of 100% ethanol were added to the water bath from time to time. Subsequently, sections were carefully collected with Leica BONDTM Plus Slides (Leica, US) and drained vertically for some time before being put on a 48°C heating plate to airdry.

2.2.11.3 Immunohistochemistry

In the following section, all the steps are carried out at room temperature unless otherwise stated. The paraffin removal, and antigen retrieval steps were carried out in hellendahl jars. For the paraffin removal, slides were washed two times for 10 min in xylene solution, then rehydrated sequentially in 100%, 70% and 50% ethanol for 10 min each. Finally, slides were washed in distilled water 15 to 20 times.

In order to eliminate the autofluorescence and/or lipofuscin from the RPE layer, subsequent application of autofluorescence block (1% potassium permanganate in 0.3% sulfuric acid and 1% oxalic acid) was applied to the slides. Slides were positioned in a humidified container and first incubated in a few drops of 1% potassium permanganate for 5 min following 3 washes in distilled water. The slides were then incubated in 1% oxalic acid for 5 min and washed again in distilled water 3 times.

Subsequently, slides were emerged in antigen retrieval buffer (90% glycerol and 10% 10mM sodium citrate pH 6) and heated gradually until boiled in a generic microwave. Once, the slides are cooled down at room temperature, they were rinsed well in distilled water 20 at least times.

After washing, slides were put back to the humidified containers and incubated in blocking solution (1% BSA, 0.3% triton x-100, 0.2% sodium azide in 1x PBS) for 1 h at room temperature. The slides were then incubated with primary antibody overnight at 4°C. On the next day, after three times for of 1x PBS washes, each 10 min, slides were incubated with secondary antibody at room temperature for 1 h. Slides were then washed 3 times for 10 min in 1x PBS before mounting with DAPI containing mounting media and put in a dark container to dry out before sealing with a transparent nail polish.

2.2.11.4 Conventional electron microscopy

ARPE-19 cells were seeded on cover glass slips (13 mm VWR, UK) in 35mm dishes as discussed in section 2.2.4 and transfected with siRNA as described in section 2.2.6. The cover slips were carefully removed with forceps from the dishes and placed in four well plates. The rest of the cells in the 35 mm dish were lysed for western blot analysis. The cells on the cover slips were washed in 1 x PBS briefly and fixed with 0.1M cacodylate containing 2% paraformaldehyde/ 2% glutaraldehyde for 30 min at room temperature. Then cells were washed three times in 0.1M cacodylate plus 2x in 0.05M cacodylate. Subsequently, cells were incubated in 1.5% potassium ferricyanide and 1% osmium tetroxide for 1 h on ice in the dark. Following the incubation, cells were washed in distal water two times. Cells then were incubated with 1% uranyl

acetate for 40 min at room temperature, followed by three washes in water. Cells were dehydrated gradually in 70%, then 90% for a few min and then two times in 100% ethanol for 10 min. Subsequently, the cover slips with cells side up were put in foil trays and immersed in neat Epon resin (20 ml araldite resin CY212, 25 ml dodecenyl succinic anhydridie (DDSA) and 0.8 ml DMP30) for 90 min, then transferred to fresh Epon for another h at least. Finally, cover slips with cells side up were put in new foil trays glazed with some Vaseline for easier removal later and inverted a stub full of Epon on top. The stubs were baked in a 60°C oven overnight. On the next day, the specimens were transferred directly into liquid nitrogen and the cover slips were removed from the stab carefully. The specimens were then sectioned on a Leica Ultra Cut 7 microtone (Leica) by Dr Emily Eden. The samples were visualised and imaged by a JEOL1010 transmission electron microscope run at 80 kV with a digital camera (Gatan) controlled by a digital micrograph software (Gatan).

2.2.12 Confocal and Epifluorescence Microscopy

Most of the images in this report were taken with CLSM 700 (Carl Zeiss) with a Z-stack and maximum intensity projections were generated using the Zeiss software. Some of the images were taken with 60x oil objective Axioscope (Carl Zeiss).

2.2.12.1 Statistical analysis

Densitometric quantification of at three or two independent immunblots were calculated by changes of the protein expression content and normalised to tubulin/b-actin. Statistics of the Western blot quantification were performed

using one-way ANOVA with Bonferroni post hoc analysis. To compare two independent conditions, student t test (unpaired) was used. At least three independent experiments were performed and statistical significance was set at 0.05.

Chapter 3 Results: Phylogeny and ARMCX expression

Members of the Armcx family have been first described as tumour suppressors (Kurochkin et al., 2001) and later to regulate mitochondrial dynamics in neurons (López-Doménech et al., 2012), however clear understanding of the physiological roles of each individual protein is currently lacking.

Bioinformatics is a rapid evolving and useful tool to understand better the functions of biological molecules, their interactions, and evolutionary changes (Pellegrini et al., 1999). Here in this chapter, we used bioinformatics platforms to gain better understanding of Armcx gene functions and evolution. We looked closer into the gene and protein sequences of Armcx members and their ancestral Armc10 from Eutherian, non-Eutherian mammals (Marsupial) and from a more distant non-mammals; Teleost fish. In addition, we also included in our analysis another group of genes which are highly homologous to Armcx and are likely to have the same evolutionary origin and thus may be considered as part of the same family of genes. They clustered closely within the same region of X chromosome: known as G-protein-coupled receptor (GPCR) associated sorting proteins (GASPs). GASP gene family consists of three members GASP1, GASP2 and GASP3 (the later also known as BHLH9), which bind to the C-termini of GPCRs and regulate their intracellular sorting to the lysosomes (Winter and Ponting, 2005). Moreover, GASP1 was shown to participate in acute and chronic behavioural responses to cocaine administration, a study done in GASP1 knockout mice. However, their data

indicates that GASP1 triggers receptor recycling rather than degradation upon stimulation (Kargl et al., 2012). Therefore, although GASPs' high homology with Armcx, they appear to have distinct functions to Armcx members, which functions are strongly associated with mitochondrial dynamics and more recently mitophagy. Importantly, it is not clear whether the evolutionary expansion of Armcx constitutes divergence of their ancestral function into separate members or to novel functions.

3.1 Marsupial ARMC10 as an ancestral gene to ARMCX family

Nucleic acid sequences of the Armcx family and related genes were acquired from the NCBI and are compiled in Table 9.1 in Appendix. First, we aimed to look at the evolutionary relationships of Armcx among close related species and we subjected Armcx gene cluster to phylogenetic analysis (Figure 3.1 A). The analysis identified marsupial Armc10 as the ancestral gene, from which two main arms emerged within the Eutheria clade. One of the arms contained Armc10 genes, whilst the other was made up of all Armcx and GASP family members. Notably, Armcx1, 2, 3 and 6 genes clustered as one sub-group within this branch, whilst Armcx4 and 5 were more closely related to the GASP family. The gene related to the ancestor Armc10 is located on chromosome 7 (7q22.1). All derived duplicated genes are all located within a relatively small cluster on the X chromosome (Figure 3.1 B).

We also looked at a global phylogenetic tree of Armc10 and its homologues in vertebrates. Armcx1-6 as well as GASP1-3 were found to diverge from Armc10 via gene duplication events, which arose at the root of Eutheria (Figure 3.1 C).

This analysis was done with the great help of Prof Christophe Dessimoz and Dr Alex Warwick Vesztrocy from Genetics, Evolution & Environment department at UCL. Furthermore, a phylogenetic circle tree analysis suggested that Armcx6 was the first to appear within Eutharia, followed by Armcx3 and Armcx1 and 2. Next, Armcx4, Armcx5 and the GASPs were followed. This further showed that Armcx1, 2, 3 and 6 emerged closer to each other group than Armcx4 and 5, whose were more closely related to GASP members in Eutheria.

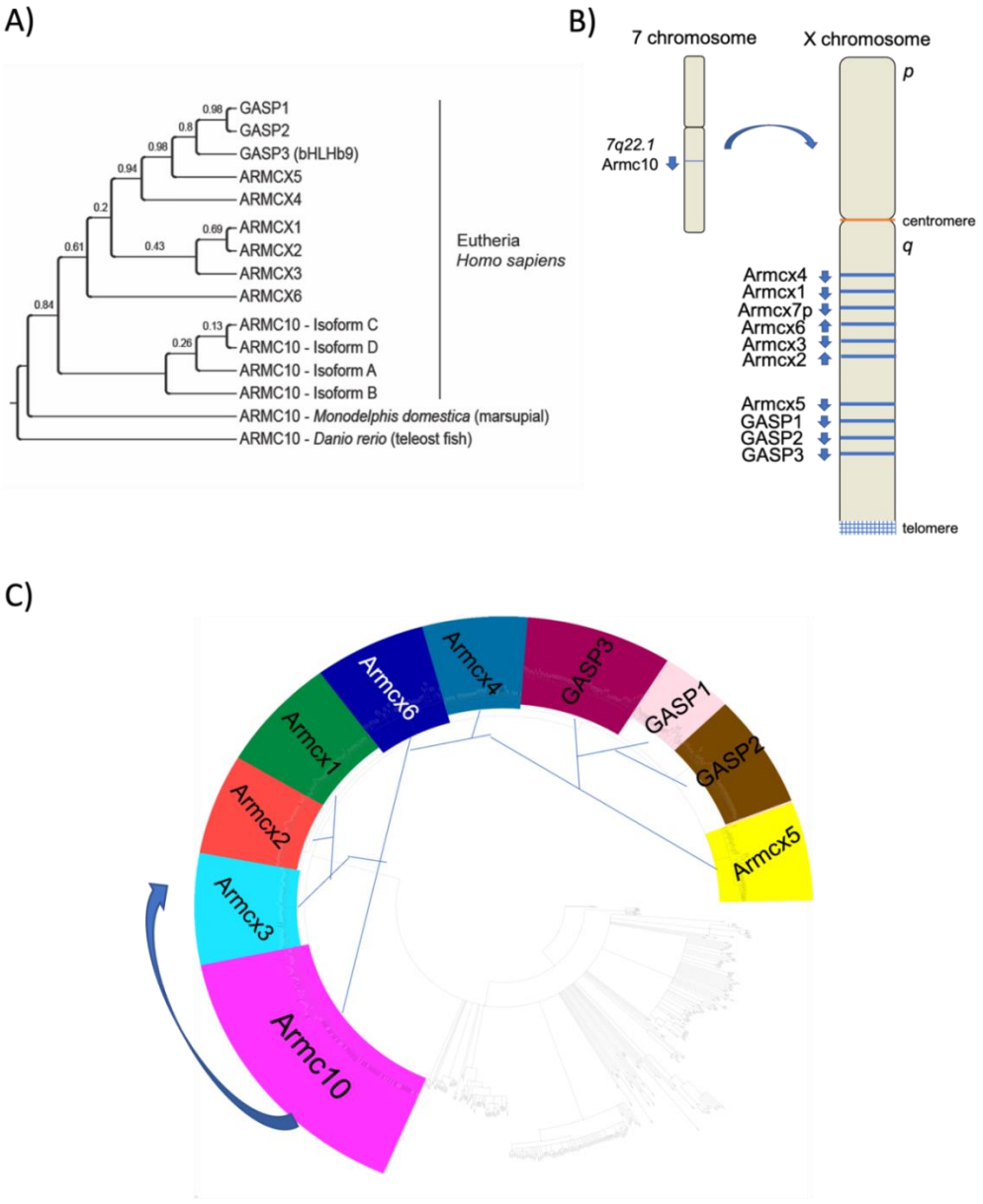

Figure 3.1 Phylogeny of Armcx. **A)** A phylogenetic tree showing Armc10 Marsupial as an ancestral gene to Eutherian Armcx and GASP families. The phylogenetic tree was generated using PhyML (default model) by the master student Alice Kirby (Kirby A 2016). A multiple sequence alignment of the amino acid sequences was performed via PhyML software; numbers represent bootstrap values showing the support of each node, where the closer the number to 1 (100%) the better support **B)** Schematic presentation of the protein-coding gene order of Armcx 1-6 and one pseudo gene (Armcx7p) and GASP1-3 members in human X chromosome and Armc10 on 7th chromosome. Transcriptional orientations are indicated by blue arrows. **C)** The phylogenetic circle tree was generated by using the highly conserved armadillo repeats of each gene. The tree conveys the order of duplication events. The analysis was kindly provided by Prof Christophe Dessimoz at UCL.

3.2 ARMCX genes are highly present in the Eutherian clade

This analysis was done to establish if all current eutharian have all the genes or if some (due to potential functional redundancy) have been lost (Figure 3.2). Armcx members are shown to be present throughout Eutheria with some members more frequently annotated than others, e.g., Armcx5 and ARMC10 have been identified mostly in all Eutherian species whereas other members such as Armcx4 and Armcx3 appear to be lacking in some species. Moreover, looking closely at primates, we observed heterogenous existence of Armcx and GASP members. ARMC10, Armcx5 and GASP1 were highly present, whereas Armcx3, GASP2 and GASP3 appeared mostly absent (Figure 3.2 red box). However, we need to acknowledge here some possibly all of the absences are due to issues with genome sequencing/assembly/annotation; e.g., Armc10 gene as well as GASP3 are present in Dasypus novemcinctus (nine-banded armadillo) from Xenarthra, but are absent in to their close relative species Echinops telfairi (hedgehog; Afrotheria clade). This suggests that both genes have not been properly genome annotated in all species. Another example that is highly likely to be the reason of incomplete genome annotation is the loss of Armcx1 and Armcx3 in Capra Hircus (goat), but they appear in Ovis Aries (sheep) (Figure 3.2). Notably, this problem can only unambiguously be resolved by manual scrolling through and annotation of genome sequences. Furthermore, in some cases the loss is consistent across close related species and therefore are possible older losses e.g., Armcx4 loss in Tarsius syrichta, Tupaia belangeri and Ochotona princeps.

In addition, the taxonomy tree above the presence/absence matrix confirmed that order of appearance of Armcx and GASPs in Eutheria (Figure 3.2).

Overall, we can conclude that all Armc and GASP genes are widely distributed and appear essential for Eutheria.

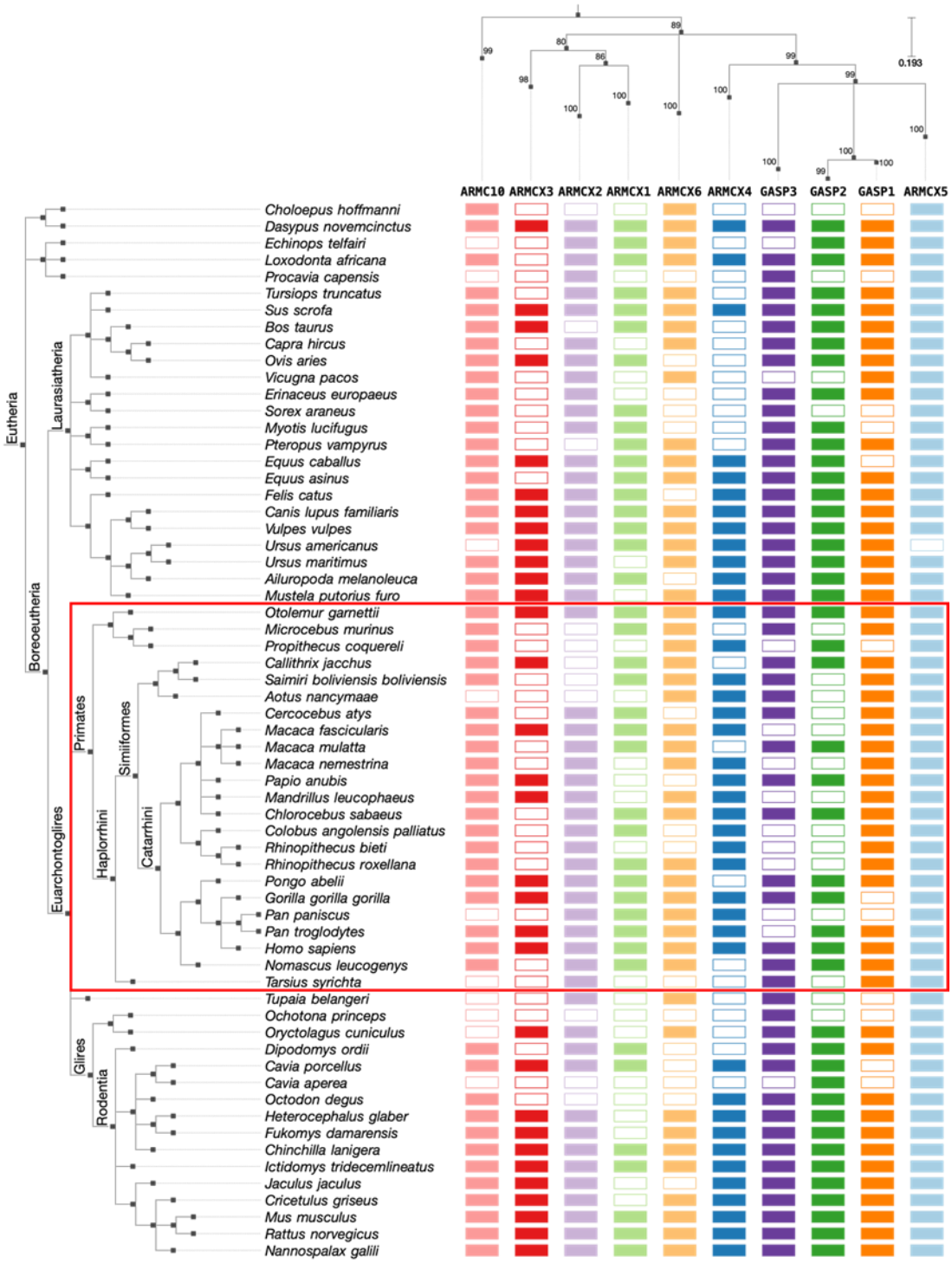

Figure 3.2 Presence/absence matrix of Armcx family and their homologues in Eutheria. The matrix is supported with a taxonomy of Eutheria on the left side. Bootstrap replicates were computed with a support of above 80%. Each column represents different gene member and has a different colour. A filled box indicates the presence of that gene in a particular species and an empty box indicates the absence. The analysis was kindly provided by Prof Christophe Dessimoz at UCL.

3.3 ARMCX sequence analysis

Next, we analysed the putative structural domains within Armc10/Armcx and GASP family members from protein sequence information obtained from the UniProt Knowledgebase/Swiss-Prot (UniProtKB/Swiss-Prot) (Boutet et al., 2007), a public biological database for classifying protein through assigning domain architecture (Doğan et al., 2016). Armc10, all Armcx and GASP members possessed highly conserved C-terminal ARM domains (Figure 3.3 A). N-termini were more variable in size and showed little sequence conservation among all members. Structurally Armc10 and Armcx contained putative mitochondrial targeting sequence (MTS) that overlapped with a transmembrane domain (TM) as well as some nuclear targeting signals (NTS). Armc10, Armcx1, 2, 3 and 6, but not Armcx4, Armcx5 and GASPs, possessed strong MTS at their N- termini. These putative MTS were also predicted by MitoFates (Fukasawa et al., 2015) with 80% confidence. Only Armcx1, 2 and 3, but not Armc10 or Armcx6 had a putative NTS.

Furthermore, we looked more closely at N-termini comprising the MTS and TM of Armcx family. Multiple protein sequence alignment of the N-termini of Armcx1-6, GASPs and Armc10 was generated by MUSCLE (EMBL-EBI) (McWilliam et al., 2013) (Figure 3.1 C). The analysis showed a conserved TM domain with closely arranged Glycine molecules amongst other small amino acid residues such as Alanine, Valine and Isoleucine in most Armcx members, but not the case for Armcx4 and 5, which possess larger hydrophobic (Tryptophan, W) and charged (Aspartic acid, D) amino acids respectively in this region. The existence of G-G motif including other small non-polar amino

acids is a well-known feature of TMs (Walters and DeGrado, 2006). This prototypical TM domain was not apparent in GASP members. Armcx1-3 and 6 also contain putative MTS that spans the TM domain. Importantly, the MTS contains positively charged amino acids (e.g. Lysine, Arginine), which is a hallmark for mitochondrial targeting signal (Walters and DeGrado, 2006). The former MTS part was observed to be highly conserved among Armcx1, 2, 3 and 6 and mammalian Armc10. In contrast, mammalian Armcx4 and fish Armc10 appeared to have uncharged amino acid residues (Glutamine and Serine respectively) instead. In the tail of MTS we observed a well conserved Tyr- Arg/Lys-uncharged residue motif, which was not as strongly conserved in Armcx5. The GASP members did not appear to have conserved MTS with Armc10 and/or Armcx proteins. Overall, Armcx4 and 5 displayed the strongest diversities in the N-termini, specifically in the putative MTSs, compared to the other Armcx family members.

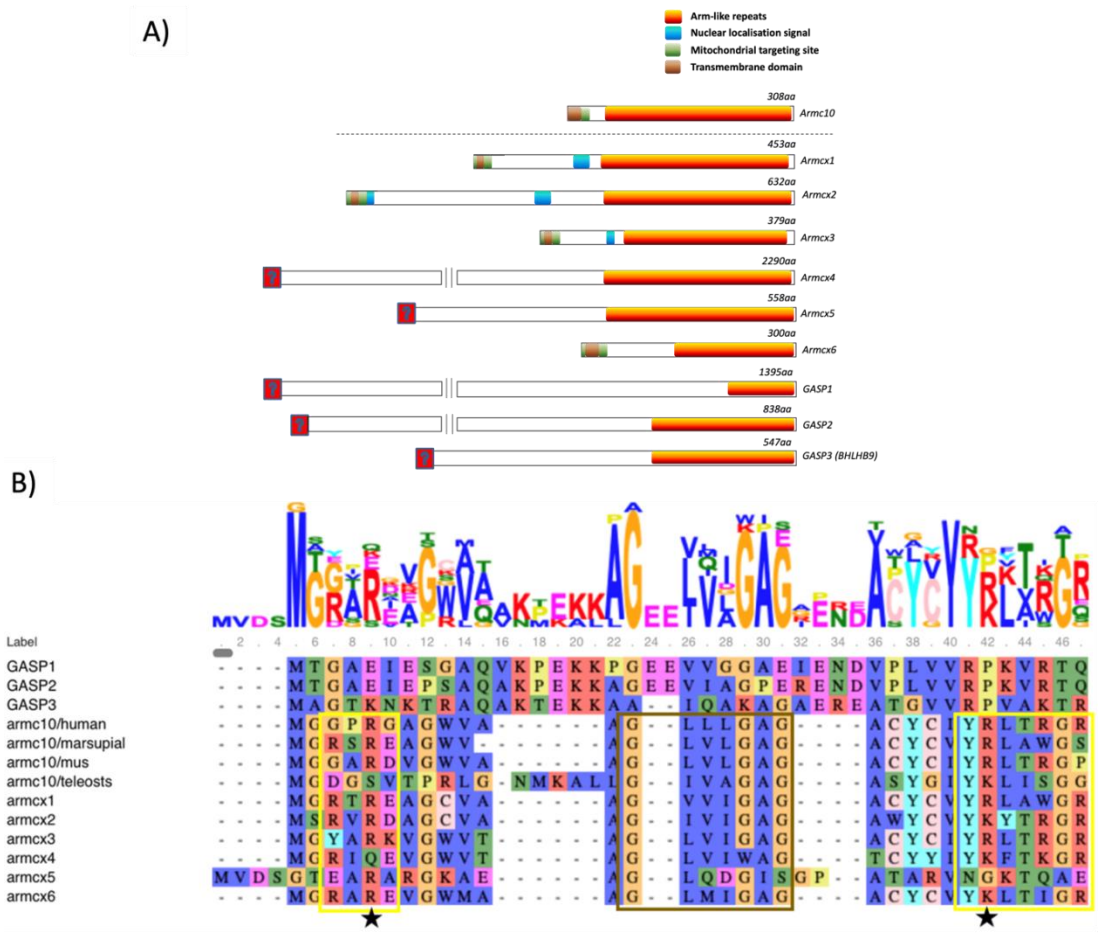

Figure 3.3 Sequence analysis of Armcx and Armc10. **A)** The schematic represents ARMCX and ARMC10 common domains; All members comprise armadillo (ARM-like) domain (orange); putative mitochondrial targeting sequences (MTS) (green) and transmembrane domain (brown apart from Armcx4, 5 and GASPs. Nuclear localisation signal is found in Armcx1, 3 and 2, where the latter appears to have two (blue). All protein domain arrangements were obtained from the UniProt Knowledgebase/Swiss-Prot (UniProtKB/Swiss-Prot). **B)** Multiple protein sequence alignment of Armcx, Armc10 and GASP N-termini was generated by MUSCLE (Edgar, 2004). The alignment shows conserved transmembrane domain (Gx-x-x-G motif, brown box) in Armc10 Armcx1-3 and 6. This motif is spanned by the MTS (yellow boxes) (**R/K**D/E/G----Y**R/K** motif)) with black stars pointing at most conserved positively charged amino acids (R and K residues). They are conserved among all Armcx members except Armcx4, 5 and Armc10 teleosts. GASPs lack the conserved transmembrane motif and the positive amino acid residues found in the putative MTS of Armcx. The consensus of amino acid residues is displayed above the alignment, where the larger the amino acid code the most frequent residues at this position, hence the stronger the conservation among the sequences.

Moreover, we looked at the secondary structure of the MTS of Armcx1, 2, 3 and 6. The secondary structure prediction server PSIPRED (McGuffin et al., 2000) suggested formation of alpha helices in the N-termini of the Armcx members, which feature is described to be important for importing proteins through the mitochondrial membrane (Liu et al., 2011, Okatsu et al., 2015).

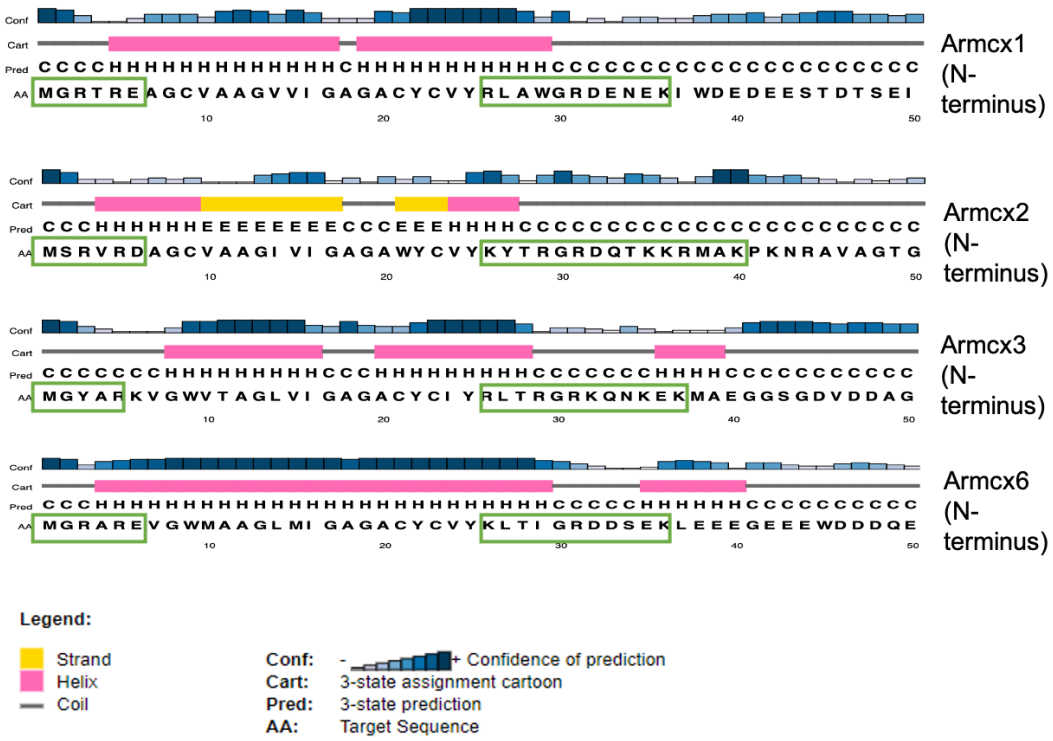

Figure 3.4 N-termini secondary structure analysis of Armcx1, 2, 3 and 6 sequences. N-termini secondary structure analysis of Armcx1, 2, 3 and 6 sequences. Secondary structure prediction of Armcx1, 2, 3 and 6 N-termini showed alpha helices formations within the MTSs; Green box was included to underline the putative MTS; The analysis was created by the PSIPRED server (McGuffin et al., 2000).

3.4 ARMCX gene expression

Subsequently, we looked into Armcx gene expression among tissues using the Genotype-Tissue Expression (GTEx) project, which comprises gene

expression data from 449 human donors across 42 distinct tissues (Consortium, 2018).

Armcx gene family showed high expression levels from non-diseased tissues, particularly among tissues which are rich in epithelial cells such as ovary, breast, prostate, bladder etc (Figure 3.5). Moderate to strong expression levels are seen also in different parts of the brain, where Armcx6 showed the weakest expression among the family. Lowest expression levels of Armcx family are observed in the blood, liver, and skeletal muscle. Armcx3 expression showed ubiquitous expression among all tissues, except from the whole blood. In less extent Armc10 also showed constant expression levels with lowest expression in the blood. GASP1 and GASP2 expression appeared high in the brain, and epithelial-rich tissues, similarly to Armcx1, 2 and 3. However, GASP3 (BHLHB9) revealed relatively low expression among tissues, similarly to Armcx6 (Figure 3.5).

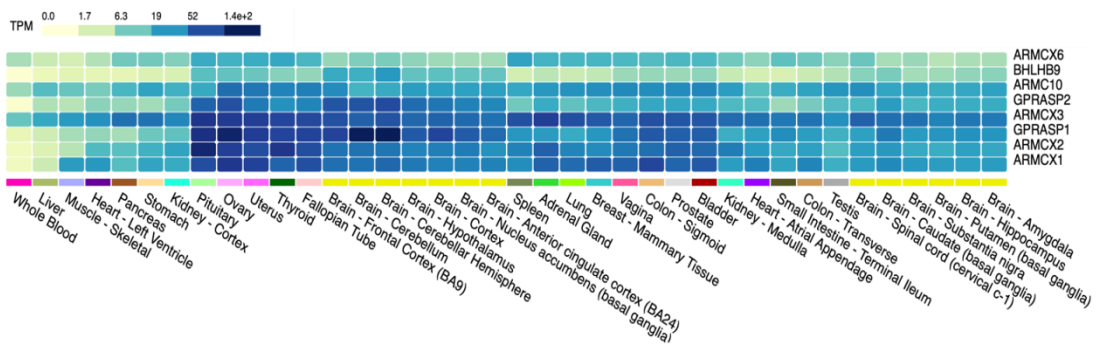

Figure 3.5 Matrix graph of the relative expression levels of Armcx genes in multiple normal tissues determined via GTEx portal. The expression levels are represented by blue colour where the greater the expression the stronger the shade colour. TPM (transcripts per million).

Furthermore, preliminary gene expression data from human fetal RPE cells differentiated *in vitro* indicated Armcx members to be important for RPE maturation *in vitro*. The Armcx/GASP and Arcm10 expression was analysed in a RNAseq data set provided by Dr Monte Radeke (UCSB). The dataset looks at 32 days long differentiation protocol of human fetal RPE cells *in vitro* (Figure 3.6). The dataset shows Armcx1, 2, 3 and 6 to be expressed at similar levels in day 3 post-differentiation RPE cells and with higher expression levels after 32 days differentiation *in vitro*. On the other hand, Armcx4 and Armcx5 were expressed less at day 3 in comparison to the rest of the family and with nearly none to some increase in their expression after 32 days differentiation, respectively. This evidence further indicates Armcx4 and 5 to have diverse functions to the rest of Armcx family. Moreover, the ancestral gene of Armcx, Armc10 shows similar expression levels at day 3 to the rest of the family and displays higher expression after 32 days of differentiation. Notably, GASP1 and GASP2 show strong expression in RPE and very sharp upregulation after 32 days of differentiation of RPE cells. In contrast, GASP3 exhibits little expression levels prior and after *in vitro* differentiation (Figure 3.6).

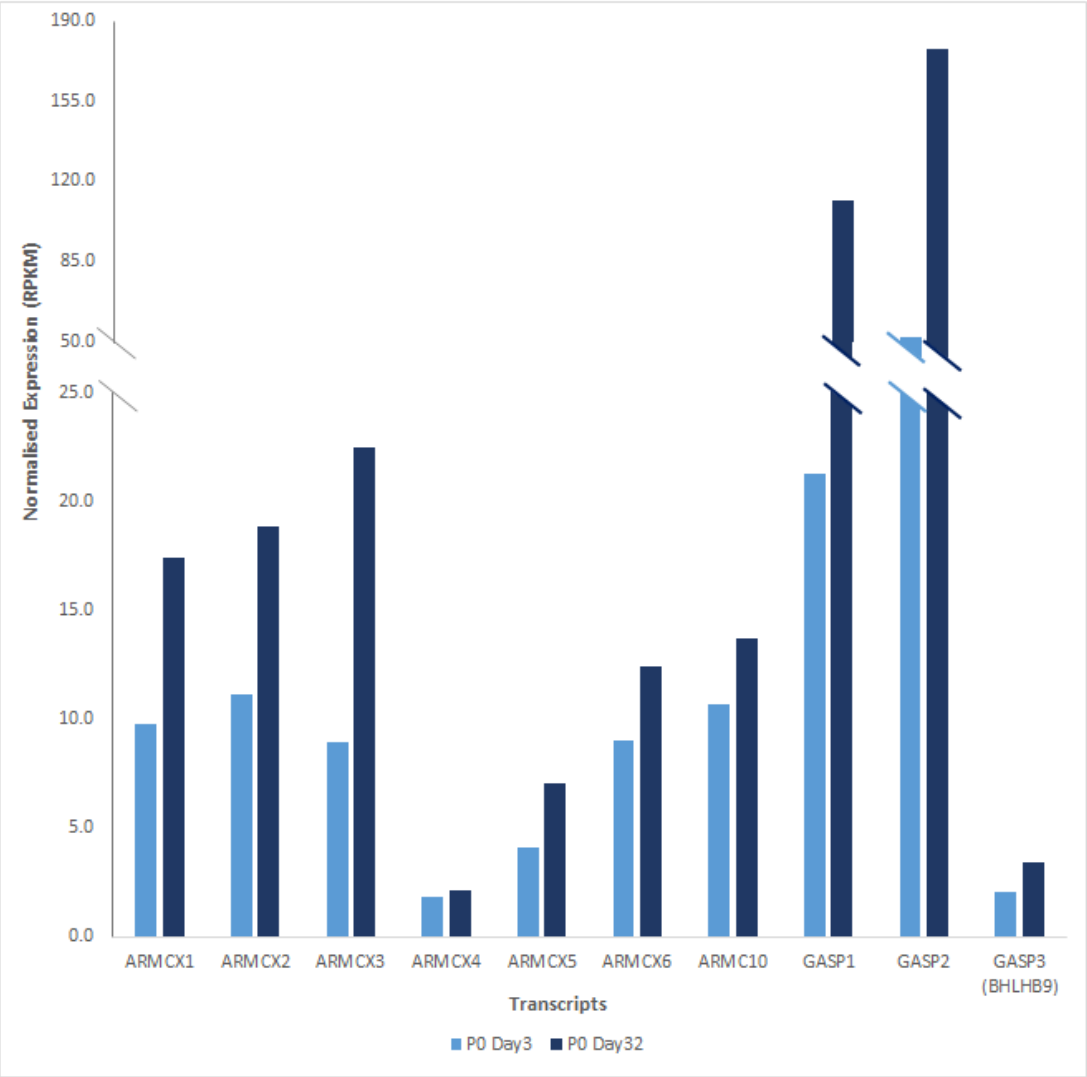

Figure 3.6 Armcx expression profile in fetal RPE differentiation. RNA levels in human fetal RPE cells cultured *in vitro*. RNA expression was determined by RNAseq in non-differentiated (Day 3, light blue column) and differentiated (Day 32, dark blue column). Raw data courtesy of Dr M. Radeke UCSB (unpublished data). RPKM – reads per kilobase of exon per million mapped reads.

In addition, preliminary data provided by a previous master student (Yang, 2013) showed that expression of Armcx members was upregulated during ARPE-19 differentiation *in vitro*. ARPE-19 were differentiated by growth in high-glucose DMEM/pyruvate medium for 1 week, 3 or 7 months, and mRNA expression levels of Armcx1-6 assessed by real-time qPCR. The results

showed an upregulation of the mRNA levels of all Armcx with increased culture time (Figure 3.7).

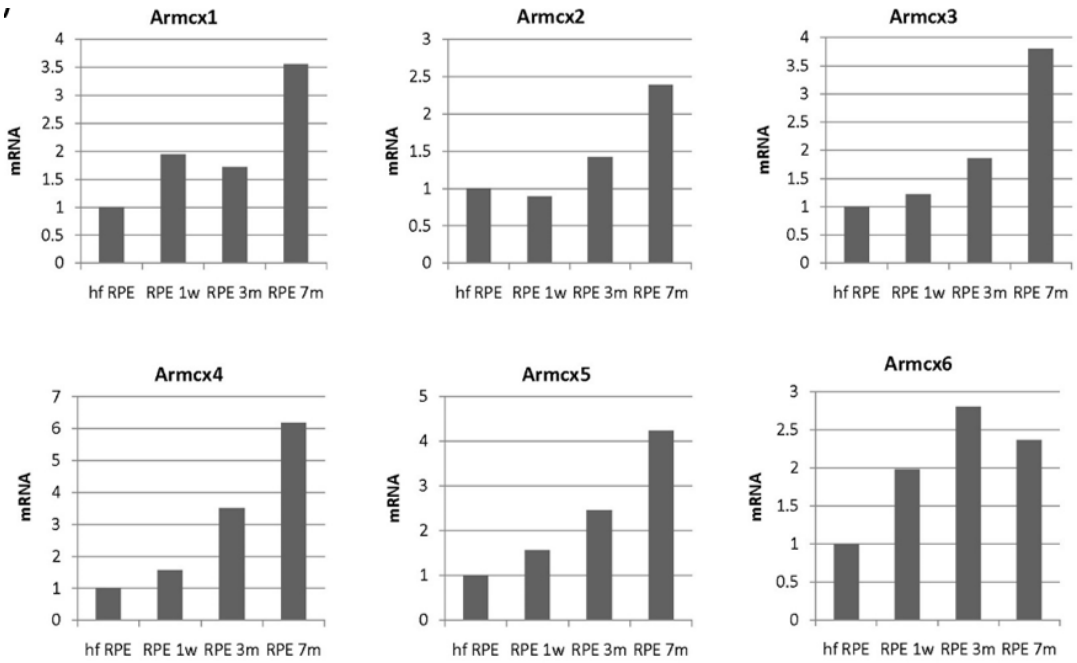

Figure 3.7 Armcx expression profile in ARPE-19 differentiation. RT-qPCR analysis of Armcx levels in ARPE-19 cells; different lengths of cell line culture were tested – 1 week (1w), 3 months (3m) and 7 months. Preliminary data from the master thesis of MingMin Yang (Yang, 2013).

Overall, the Armcx expression profile appears to be ubiquitous among epithelial rich tissues and also to be important for the maturation of an important epithelium cultured *in vitro* – the RPE. Among Armcx family, Armcx4 and Armcx5 showed the least expression upon differentiation of fetal RPE cells suggesting their lack of importance in the process. As, in addition, Armcx4 and Armcx5 appeared to be evolutionary more related to the GASP family, and to lack the conserved MTS residues, hence we decided to exclude them from further analysis in this project.

3.5 Discussion

In this chapter, we explored different bioinformatic approaches to understand better Armcx family evolution, and whether their existence is purely redundant, or different member(s) exhibit different functions.

Our sequence analyses showed that Armcx4 and 5 are clearly different from the rest of the Armcx. In fact, they are more related to GASP family proteins than Armc10. The GASP family possesses highly conserved C-terminal and a 15 amino acid motif amongst them. In contrast their N-termini are highly variable, and no membrane targeting sequences have been identified so far (Abu-Helo and Simonin, 2010). Accordingly, GASP proteins are mostly seen in cell cytoplasm and/or transported to the nucleus (Kiyama et al., 2006). In agreement, our analyses failed to show bona fide transmembrane domains in the N-termini of GASPs, Armcx4 or 5. Transmembrane domains normally consist of stretches of small hydrophobic amino acid residues, with an important presence of glycine residues, which is crucial for transmembrane alpha helix packing (Javadpour et al., 1999). GASPs, Armcx4 and 5 do not show the conserved glycine motif identified in the other Armcx and Armc10. Armcx5 contains aspartic acid where the glycine motif is seen in the rest of the Armcx as well as a proline residue. In fact, the presence of proline residues within hydrophobic stretches disfavour proteins to be arrested within membranes (Meier et al., 2005). Also, the presence of charged amino acids normally is seen to surround the hydrophobic TM sequence (Javadpour et al., 1999). This also is true for the GASP members, which contains a high abundance of hydrophilic residues in this area. Hence, GASP family, Armcx5

and to a lesser degree Armcx4 lack TM domain, which clearly distinguishes them from the other Armcxs and Armc10. In addition, GASPs have previously been characterised with a 15-amino acid WFW-containing motif that was also identified in Armcx5 (Rangachari et al., 2011). This further suggests that Armcx5 may have a function closely related to GASPs receptor sorting. Moreover, the amino acids that indicated a conserved putative MTS in Armcx1, 2, 3 and 6 were absent in Armcx4 and 5. In support to this, exogenous Armcx5 expression showed strong cytosolic and nuclear subcellular localisation and a lack of mitochondrial co-localisation in ARPE-19 cells. Furthermore, GASP1 and 2 transient and endogenous expressions have been found mainly in the cytoplasm and more rarely in the cell nucleus *in vitro* (Beausoleil et al., 2004, Bartlett et al., 2005).

Overall, Armcxs exhibit strong homology with GASPs, however phylogenetic analysis combined with observations from sequence analysis indicates that Armcx4 and Armcx5 have diverged apart from Armc10 and Armcx1, 2, 3 and 6.

Armcx and Armc10 show wide distribution among tissues, except for Armcx6 which is mainly expressed in pituitary gland and spleen as reported previously (Kusama et al., 2010). Moreover, the ubiquitous expression of Armcx members in epithelial rich tissues is not unexpected since this family was first described as tumour suppressors in cancer affecting the epithelium of different tissues (Kusama et al., 2010). Notably, the expression of Armcx1 and 2 are absent in cells from the blood, whereas Armcx3, 6 and Armc10 are expressed at low levels compared to their expression in other tissues. In agreement to

this, Armcxs were previously found to be absent in leukocytes (Kurochkin et al., 2001), further suggesting the importance of Armcx in cell with strong polarisation such as the epithelium.

The development of primary cell cultures of human fetal RPE cells have shown to meet very closely the criteria of RPE characteristics *in vivo* (Maminishkis et al., 2006). Therefore, the observation of Armcx members being strongly upregulated in human fetal RPE cells cultured *in vitro* strongly indicates the importance of Armcx in mature RPE cells. Importantly, we have also seen similar pattern of increased mRNA levels of Armcx members in ARPE-19 cell line differentiated *in vitro*, which further supports the Armcx role in RPE cells. In particular, Armcx1, 2, 3 and 6 transcripts were strongly upregulated in human fetal RPE and the RPE cell line ARPE-19, whereas Armcx4 and 5 mRNA levels were only increased in differentiated ARPE-19, but not in fetal RPE cells. Differences in results between ARPE-19 and fetal cells could be due to the longer differentiation time ARPE-19 were subjected to. Alternatively, this could reflect genuine differences in the gene expression patterns between ARPE-19 and fetal cells. Indeed, whilst ARPE-19 represents a much used alternative to native RPE cells, this cell line fails to replicate all functional characteristics and gene expression patterns of RPE *in vivo* (Samuel et al., 2017). However, despite their flaws, ARPE-19 stands out as a perfect use to analyse Armcx function in RPE further.

Importantly, the heterogenous appearance of Armcx and their homologues in primates suggests that the presence of some members of Armcx family is sufficient to support the maturity of RPE and macula, the latter being

specifically seen only in primates. Notably, humans and macaques both possess genes that are found linked to AMD and other retinal diseases (Picaud et al., 2019), The lack of Armcx3 and Armcx1 in macaques (Macaca nemestrina) suggests that the function of Armcx is probably supported by either their ancestral ARMC10 or the other Armcx members. Nevertheless, as described above we need to account here that these datasets are not conclusive due to issues with genome annotation, and this can be surmounted only by manual scrolling though annotations and genome sequences.

Furthermore, given the fact that Armcx4 and Armcx5 exhibit strong difference from the rest of the Armcx family, and they appear to be expressed differently in the human fetal RPE, this further indicates that these two members play different roles. Therefore, we decided to exclude Armcx4 and Armcx5 from further analysis in this project.

Chapter 4 Results: ARMCX in RPE cells

4.1 ARMCX1, 2, 3 and 6 are mitochondrial targeted proteins in RPE

In the following chapter we focus on studying the connection between Armcx and RPE cells, a subject that has not been studied before. Moreover, we also aimed to select the Armcx members whose phenotypes were considered most promising in affecting RPE function and focus on observing their role in RPE in more depth. As covered in more detail in chapter 1, the loss of RPE layer due to mitochondrial dysfunction is considered to play a pivotal role in the pathophysiology of AMD (Barot et al., 2011). Functionally, Armcx members are described previously as mitochondrial associated proteins, therefore, we aimed to focus on mitochondria targeted Armcx and their detection in RPE. The selection was also based on the quality of commercially available antibodies against Armcx.

There has been a strong urge for the development of *in vitro* cell culture models for RPE in the past decade, mainly due to the increased interest in RPE function and its role in multiple retinal disorders (Maminishkis et al., 2006). The spontaneously arising human RPE cell line (ARPE-19) initially isolated from a 19 years old male donor has been frequently used as an RPE model (Dunn et al., 1996). Nevertheless, ARPE-19 can lack many morphological and developmental traits seen in native RPE cells, including pigmentation, polarity markers and low transepithelial resistance. Notably, the

use of cell substrates and special growth media can promote a more native RPE phenotype in ARPE-19 cells (Zhao et al., 1997, Lund et al., 2001, Ahmado et al., 2011, Hazim et al., 2019), allowing them to be widely used to study a variety of molecular and cellular mechanisms that determined important features of the RPE (Maminishkis et al., 2006, Hazim et al., 2019). In addition, the ARPE-19 cell line has been prioritised in research due to its easy access, manipulation, and low cost in contrast to other RPE cell models, which require more time and resources – e.g. RPE derived from embryonic and induced pluripotent stem cells (Hazim et al., 2019). However, it remains unknown how *in vitro* differentiation of RPE is regulated, thus additional research on RPE differentiation is required which would allow further usage of RPE cell lines and will benefit for RPE-cell based therapies. In respect to this, the preliminary data from human fetal RPE and ARPE-19 cell culture differentiated *in vitro* included in the previous chapter indicates some of the Armcx members to be of importance for the maturation of RPE cells. In addition, in 2004 Turowski et al reported on genes specifically expressed in basement membrane-differentiated ARPE-19 cells. This screen identified upregulation of a number of transcripts with a clear role in epithelial differentiation, but also of genes with a yet unknown role in RPE physiology. Within the latter group, Armcx6 stands out (Turowski et al., 2004). Therefore, in this project we decided to use ARPE-19 cell line to study Armcx roles in RPE function as they are easy to manipulate, economical to use and show to express Armcx when differentiated *in vitro*.

Since there is no data detailing the function of Armcx in RPE, we initially looked at the sub-cellular localisation of exogenous and endogenous Amrcx1, 2, 3 and 6 in both non-differentiated and differentiated ARPE-19 cells. ARPE-19 cells were differentiated by culture media- mediated differentiation as previously described (Ahmado et al., 2011), where cells were cultured for 20 or more weeks supplemented with pyruvate and a low concentration serum-containing medium (1% compared with 10% standard cell culture) to reduce growth factor-dependent cell division. At this point, cells were pigmented (Figure 2.) and this was visible by a naked eye. In sub-confluent or non-differentiated cells, pigmentation was not observed.

4.1.1 ARMCX1 gene encodes for a mitochondrial targeting protein in non-differentiated and differentiated ARPE-19

To study the sub-cellular localisation of the Armcx in RPE, ARPE-19 cells were transfected with pEGFP-N1-Armcx encoding full length Armcx fused at their C-terminus to EGFP (Figure 9.1 in Appendix). In accordance with the predicted protein domains in chapter 3, exogenous Armcx1 co-localised with mitochondria in non-differentiated and differentiated ARPE-19 cells, which was visualised by sub-cellular staining with MitoTracker (Figure 4.1). In some cells, there was nuclear staining occasionally seen in non-differentiated cells (data not shown).

To validate the location of Armcx1 to the mitochondria, mutants of Armcx1-GFP lacking the MTS were created via site-directed mutagenesis. Notably,

since the MTS and TM overlap, deletions of the MTS also affected the TM. Co-localisation with MitoTracker was abolished by expression of the N-terminally truncated Armcx1 in both sub-confluent, non-differentiated and differentiated ARPE-19. Instead, Armcx1 mutant protein was detected in the nucleus and cytoplasm of non- differentiated and exclusively in the nucleus of differentiated cells. Moreover, the mutant Armcx1 also shows some membrane localisation in non-differentiated cells even though the TM is interrupted (Figure 4.1 A lower panel). Notably, expression of Armcx1 lacking the N-terminus/MTS resulted in a less condensed perinuclear mitochondrial network in contrast to non-transfected cells or Armcx1-WT expressing cells (Figure 4.1 A lower panel).

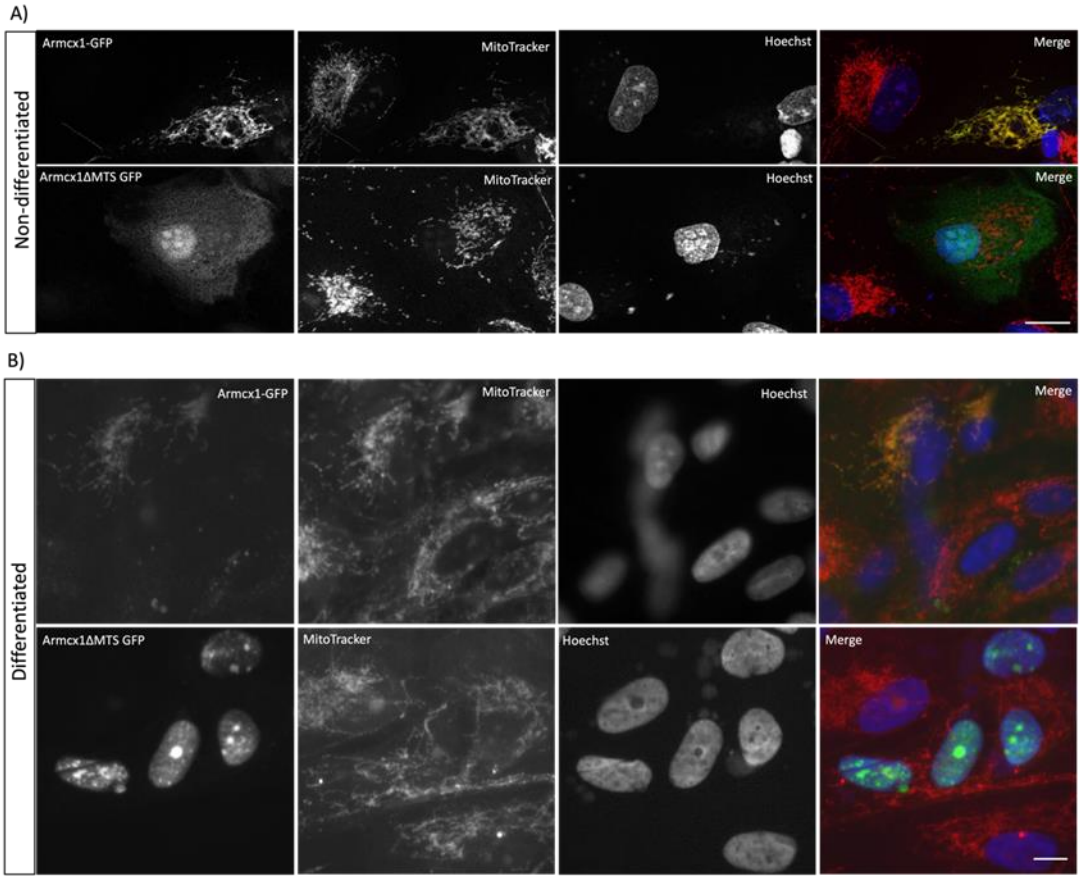

Figure 4.1 Armcx1 N-terminus is necessary for Armcx1 mitochondrial targeting in non-differentiated and differentiated ARPE-19 (>20 weeks). **A)** Armcx1 co-localises with mitochondria in sub-confluent cells (upper panels); Armcx1 mutant lacking N-terminus with the MTS lost mitochondrial targeting signal (lower panels); cells were transfected with 1 µg Armcx1-GFP full length (green) 24 h prior methanol fixation; MitoTracker (red) represents a mitochondrial marker; Hoechst staining (blue) shows nuclei; Images were taken by a ZEISS LSM700 confocal microscopy 63x oil objective; scale bar = 10 µm **B)** Armcx1 co-localises with mitochondria in differentiated cells (upper panels); Armcx1 mutant lacking N-terminus with the MTS lost mitochondrial targeting signal (lower panels); cells were transfected as described above; Images were taken by Zeiss Axioskop 2 63x oil objective. Scale bar = 10 µm. Unfortunately, due to loss of all differentiated ARPE-19 during the Covid-19 pandemic, we were unable to repeat these experiments and take confocal images.

4.1.2 ARMCX2 gene encodes for a mitochondrial targeting protein in non-differentiated and differentiated ARPE-19

Like Armcx1, exogenously expressed Armcx2-GFP also co-localised with MitoTracker in both non-differentiated and differentiated APRE-19 cells. Functionally, Armcx2-GFP expression resulted in mitochondrial perinuclear aggregation (Figure 4.2, upper panels). In a similar way to Armcx1, we performed a deletion of the N-terminus of Armcx2 that included the MTS. Truncation of the N-terminus of Armcx2 abolished mitochondrial targeting of the protein in all ARPE-19 cultures, with the Armcx2 mutant instead localised to the nucleus and cytoplasm (Figure 4.2, lower panels). Notably, the expression of MTS-mutated Armcx2 failed to induce the mitochondrial aggregation seen with the Armcx1 mutant. Moreover, Armcx2 mutant protein also shows some membrane localisation in both non-differentiated and differentiated cells (Figure 4.2, lower panels).

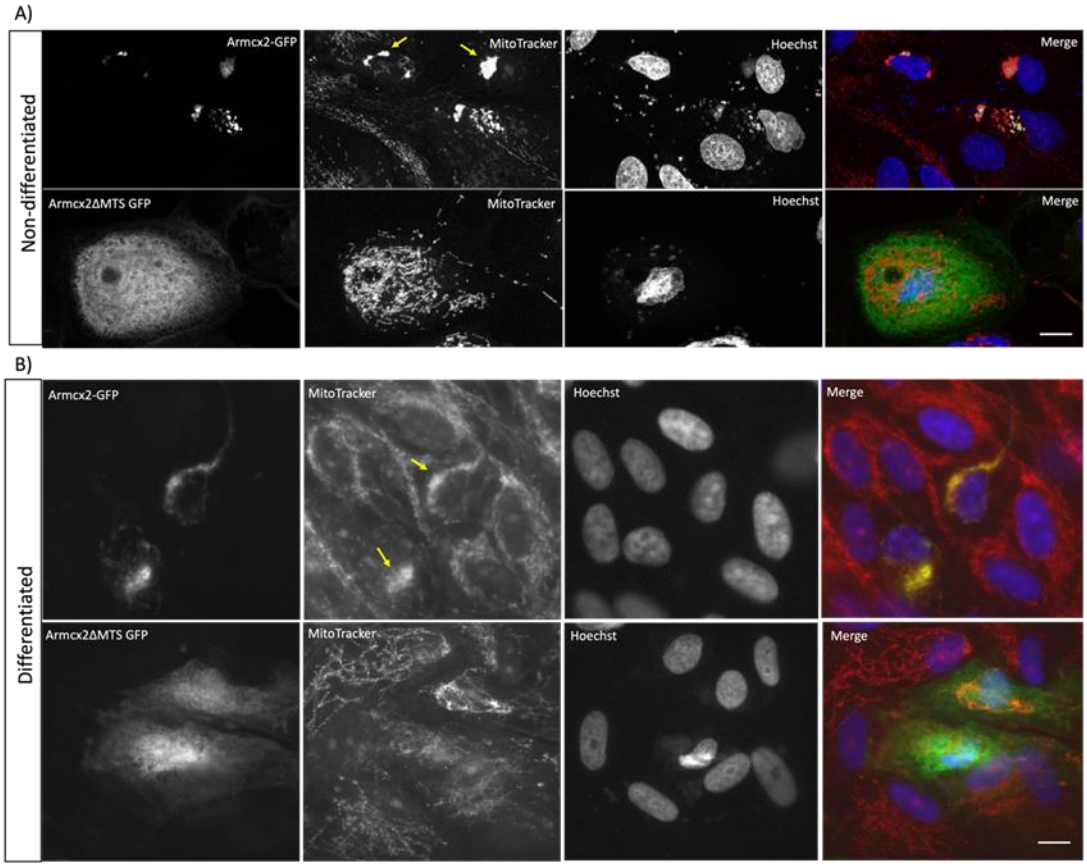

Figure 4.2 Figure 4.2 Armcx2 N-terminus is necessary for Armcx2 mitochondrial targeting in non-differentiated and differentiated ARPE-19 (>20 weeks). **A)** Armcx2 co-localises with mitochondria in sub-confluent cells and caused mitochondrial aggregation (yellow arrows; upper panels); Armcx2 mutant lacking N-terminus with the MTS lost mitochondrial targeting signal (lower panels); cells were transfected with 1 µg Armcx2-GFP full length (green) 24 h prior methanol fixation; MitoTracker (red) represents a mitochondrial marker; Hoechst staining (blue) shows nuclei; Images were taken by a ZEISS LSM700 confocal microscopy 63x oil objective; scale bar = 10 µm. **B)** Armcx2 co-localises with mitochondria in differentiated cells and also results in aggregated mitochondria (yellow arrows; upper panels); Armcx2 mutant lacking N-terminus with the MTS lost mitochondrial targeting signal (lower panels); cells were transfected as described above; Images were taken by Zeiss Axioskop 2 63x oil objective. Scale bar = 10 µm. Unfortunately, due to loss of all differentiated ARPE-19 during the Covid-19 pandemic, we were unable to repeat these experiments and take confocal images.

4.1.3 ARMCX3 gene encodes for a mitochondrial targeting protein in non-differentiated and differentiated ARPE-19

Transfected Armcx3-GFP showed a heterogeneous distribution including mitochondrial, nuclear, and cytoplasmic in sub-confluent ARPE-19 cells, whereas in differentiated cells Armcx3 specifically associated with mitochondria (Figure 4.3, upper panels).

Next, we examined the mitochondrial targeting of Armcx3 by truncating the putative MTS. Indeed, expression of the Armcx3 MTS mutant resulted in no mitochondrial association. Some mutant Armcx3 expressing, non-differentiated cells showed less perinuclear distribution of mitochondria (Figure 4.3 A, yellow arrows, lower panel). Similarly, to Armcx1 and Armcx2, Armcx3 mutant proteins showed some membrane localisation, even though the TM is removed (Figure 4.3, lower panels).

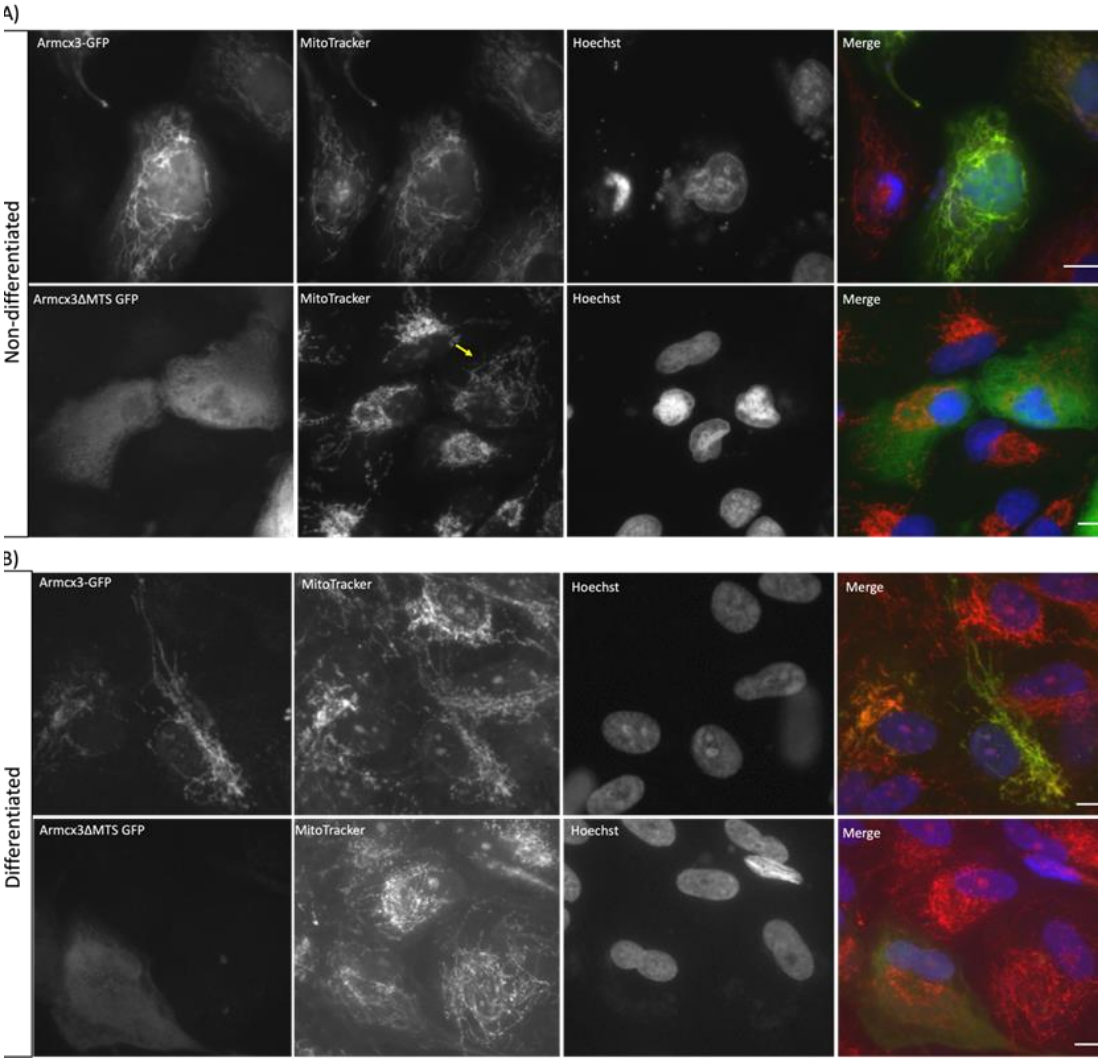

Figure 4.3 Armcx3 N-terminus is necessary for Armcx3 mitochondrial targeting in non-differentiated and differentiated ARPE-19 (>20 weeks). **A)** Armcx3 resulted in hetergenous co-localisation with mitochondria, nucleus and cytoplasm in non-differentiated cells (upper panel); Armcx3 mutant lacking N-terminus with the MTS lost mitochondrial targeting signal (lower panels); cells were transfected with 1 µg Armcx3-GFP full length (green) 24 h prior methanol fixation; MitoTracker (red) represents a mitochondrial marker; Hoechst staining (blue) shows nuclei. **B)** Armcx3 co-localises only with mitochondria in differentiated cells (upper panels); Armcx3 mutant lacking N-terminus with the MTS lost mitochondrial targeting signal (lower panels); cells were transfected as described above; all images were taken by Zeiss Axioskop 2 63x oil objective. Scale bar = 10 µm. The images for Armcx3 were not taken by confocal due to insufficient time to remake the experiments and subsequently take confocal images following the disruptions of Covid-19 pandemic.

4.1.4 ARMCX6 gene encodes for a mitochondrial targeting protein in non-differentiated and differentiated ARPE-19

Imaging Armcx6-GFP revealed nuclear and mitochondrial association in sub-confluent cells and specific mitochondrial localisation in differentiated ARPE-19 cells (Figure 4.4, upper panels). As with the other Armcx proteins, we verified Armcx6 mitochondrial targeting by mutating the N- terminus, which contains the putative MTS. Notably, once the N-terminus carrying the putative MTS was deleted in Armcx6-GFP, the protein was no longer associated with mitochondria. Instead, mutant Armcx6 was detected in the nucleus and cytoplasm (Figure 4.4, lower panels). In addition, the expression of Armcx6 mutant protein caused less distributed perinuclear mitochondria than in control cells and/or in Armcx6-WT expressing cells. It is an interesting observation for Armcx6-WT and mutant being co-localised with the nucleus even though this protein seems not to possess an nuclear localisation signal (NLS). Comparably to the others Armcx tested, Armcx6 mutant protein was also see localised on the plasma membrane.

We conclude that Armcx1-3 and 6 encode for mitochondrial associated proteins suggesting their regulation over mitochondrial function in RPE cells.

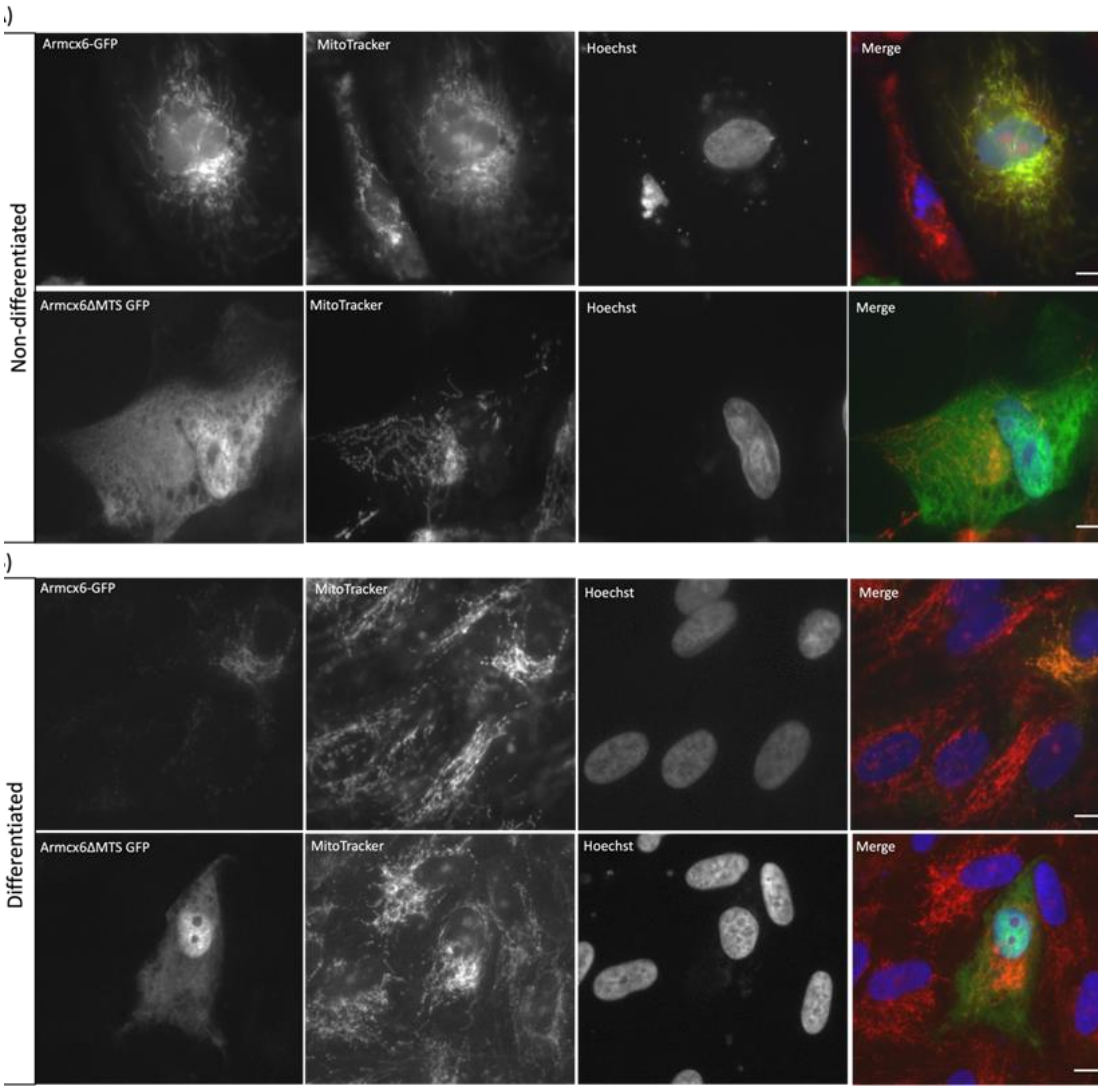

Figure 4.4 Armcx6 N-terminus is necessary for Armcx6 mitochondrial targeting in non-differentiated and differentiated ARPE-19 (>20 weeks). **A)** Armcx6 resulted in nuclear and mitochondrial co-localisation in non-differentiated cells (upper panel); Armcx6 mutant lacking N-terminus with the MTS lost mitochondrial targeting signal (lower panels); cells were transfected with 1 µg Armcx6-GFP full length (green) 24 h prior methanol fixation; MitoTracker (red) represents a mitochondrial marker; Hoechst staining (blue) shows nuclei. **B)** Armcx6 co-localises with mitochondria in differentiated cells (upper panels); Armcx6 mutant lacking N-terminus with the MTS lost mitochondrial targeting signal (lower panels); cells were transfected as described above; all images were taken by Zeiss Axioskop 2 63x oil objective. Scale bar = 10 µm. The images for Armcx6 were not taken by confocal due to insufficient time to remake the experiments and subsequently take confocal images following the disruptions of Covid-19 pandemic.

4.2 Study of endogenous ARMCX in RPE cells

4.2.1 ARMCX antibodies that recognise overexpressed ARMCX-GFP tagged proteins

Specificity and sensitivity of commercially available antibodies for Armcx1, 2, 3 and 6 (see Table 2.1) were screened in multiple ways.

First, their ability to recognise exogenously expressed Armcx-GFP by indirect immunofluorescence in fixed proliferative, non-differentiated ARPE-19 was assessed. Following transfection of Armcx1, 2, 3 and 6-GFP plasmids, all antibodies tested strongly recognised the relevant GFP-tagged proteins in immunofluorescence (Figure 4.5). Antibody staining correlated completely with GFP, indicating that the antibodies showed reactivity to the Armcx they were raised against. Armcx1 antibody showed some staining in cells that lacked Armcx1-GFP expression, which indicates endogenous protein detection. Armcx2 and Armcx6 antibodies also showed some weak staining in cells that were not positive for Armcx2/6-GFP. Armcx3 antibody detected only the exogenous Armcx3-GFP and appeared not to stain any endogenous protein.

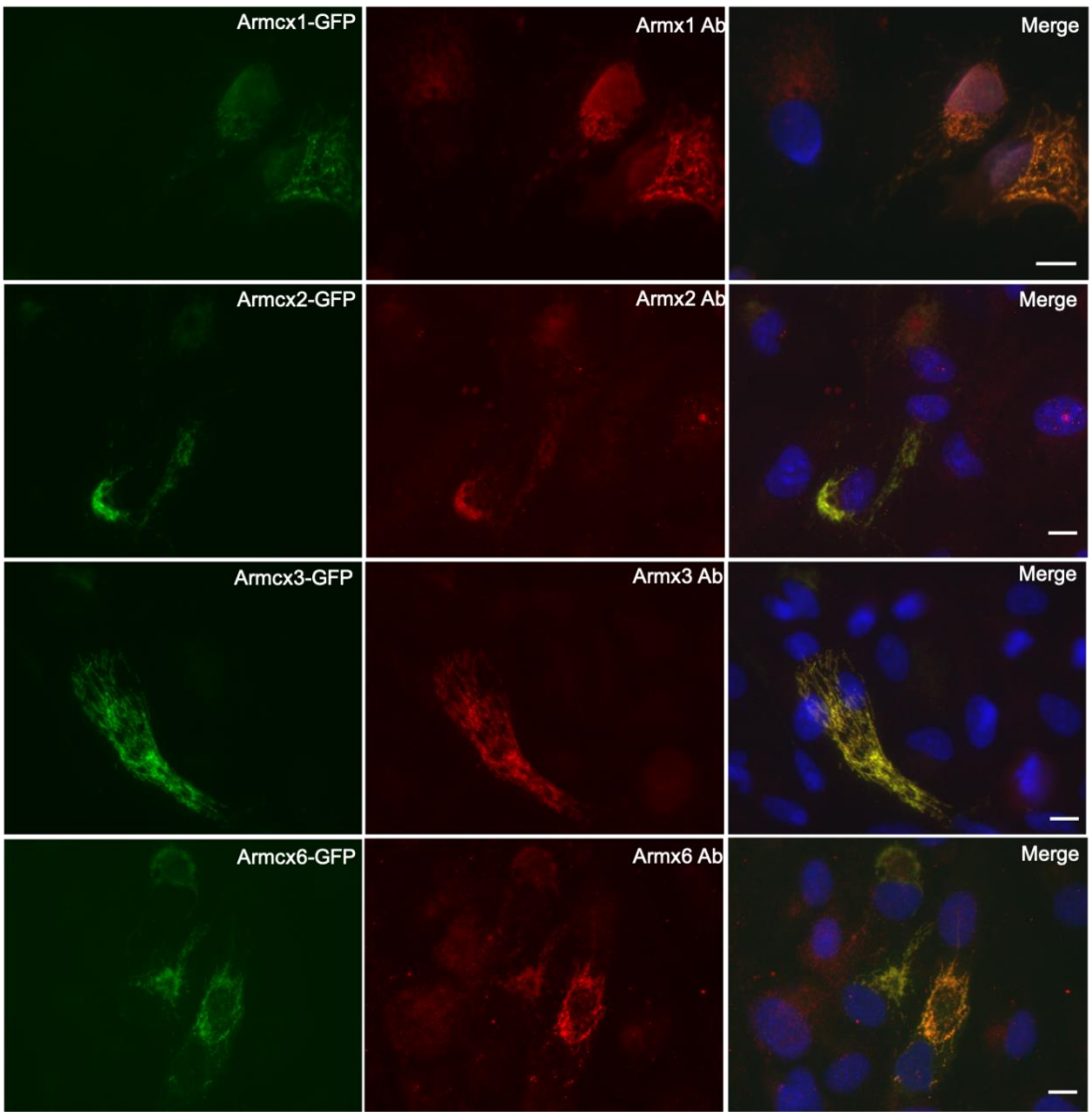

Figure 4.5 Commercial Amrcx antibodies recognise overexpressed Armcx-GFP tagged proteins. Non-differentiated ARPE-19 cells were transfected with 1 µg Armcx-GFP plasmids 24 h prior methanol fixation. Subsequent indirect immunofluorescence was carried out using antibodies against Armcx1-3 and 6. Cells were mounted with mounting media containing Hoechst, which stains the nucleus (blue in the merge, right panels). Subsequently, cells were imaged with the Zeiss Axioskop 2, 63x oil objective and representative images shown. Fluorescence from Armcx-GFP constructs (green, left panels) and corresponding antibody labelling (red, central panels) showed strong colocalisation (yellow in the merge, right panels). Scale bar = 10 µm.

4.2.2 Detection of endogenous ARMCX in differentiated ARPE-19

Next, antibodies were tested for their ability to detect endogenous Armcx1, 2, 3 and 6. Since the expression levels of Armcx were higher in differentiated ARPE-19 (Figure 3.7), we used differentiated ARPE-19 to examine endogenous Armcx expression. ARPE-19 cells following >20 weeks of differentiation were stained with the various Armcx antibodies and counterstained with the mitochondrial marker MitoTracker. Anti-Armcx1 antibody produced filamentous staining in the cytoplasm (Figure 4.6). Staining was strongest in the perinuclear areas. Most if not all of this staining co-localised with mitochondria. Anti-Armcx2 antibodies produced cytoplasmic and nuclear staining. Some of the cytoplasmic staining was filamentous and co-localised with mitochondria. Anti-Armcx3 antibodies resulted in similar cytoplasmic staining, which partially co-localised with mitochondria, but no nuclear staining was observed. In turn, anti-Armcx6 antibody staining was very strong in the nuclei and no visible co-localisation with the mitochondrial marker. In addition, Armcx6 staining showed some possible tight junctions' localisation, however this would need to be supported with a co-staining of a tight junction specific marker (Figure 4.6).

Having tested exogenous and endogenous expressions of Armcx1, 2, 3 and 6 over the mitochondrial network of ARPE-19, we decided to focus on Armcx1 and Armcx2 for further analysis. They both showed mitochondrial association in differentiated ARPE-19. Armcx6 was excluded due to lack of endogenous mitochondrial staining and Armcx3 lacked clear overexpression phenotype

and is also the mostly studied member of Armcx family in the literature. On the other hand, exogenous Armcx2 showed a strong mitochondrial phenotype, which Armcx1 as its closest relative member did not exhibit, thus indicating different functions. Thus, for the remainder of this thesis, we aimed to study Armcx1 and 2 in more depth and their potential roles in regulating the mitochondrial network in ARPE-19.

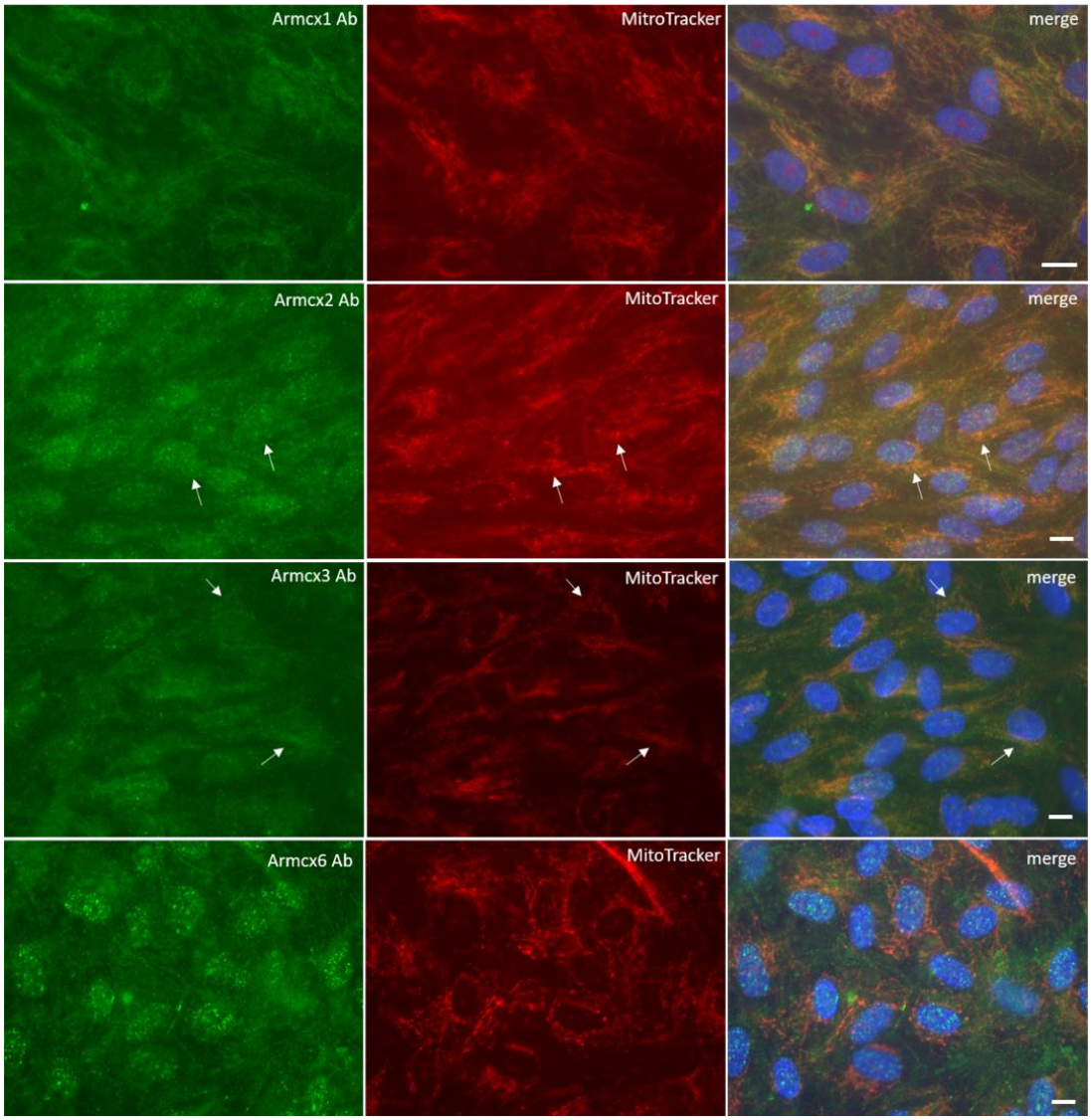

Figure 4.6 Endogenous expression of Armcx in differentiated ARPE-19 (> 20 weeks). Differentiated ARPE-19 were fixed in methanol following indirect immunofluorescence with primary antibodies against Armcx1-3 and 6 (secondary antibody Alexa Fluor 488, green). Cells were mounted with mounting media containing Hoechst, which stains the nucleus. Each row shows a different antibody (Ab) staining, where the first image shows Ab staining, the middle – mitochondria (MitoTracker in red), and the last (right hand side) is merged images of Ab and MitoTracker including nuclear staining (Hoechst in blue). Armcx1 antibody showed strong co-localisation with MitoTracker. Armcx2 and 3 also showed partial co-localisation with MitoTrack. Armcx 2 and 6 showed nuclear staining. Images were taken by Zeiss Axioskop 2 63x oil objective Scale bar = 10 µm.

4.3 Endogenous ARMCX1 and ARMCX2 are mitochondrial associated proteins in RPE

4.3.1 ARMCX1 antibody validation by siRNA

Armcx1 antibody specificity was validated by siRNAs. Four siRNA specific for unique Armcx1 sequences were transfected in ARPE-19 either individually or as a pool. When all four siRNA were transfected as a pool endogenous Armcx1 levels were strongly reduced 72 h post transfection in immunofluorescence and Western blot analysis (Figure 4.7 A, B). Here, we also tested individually the four siRNAs with the aim to distinguish different levels of the knockdown for further functional studies. One of the siRNA (siArmcx1.3) 72 h following transfection resulted in the strongest decrease of Armcx1 protein levels (Figure 4.7 C).

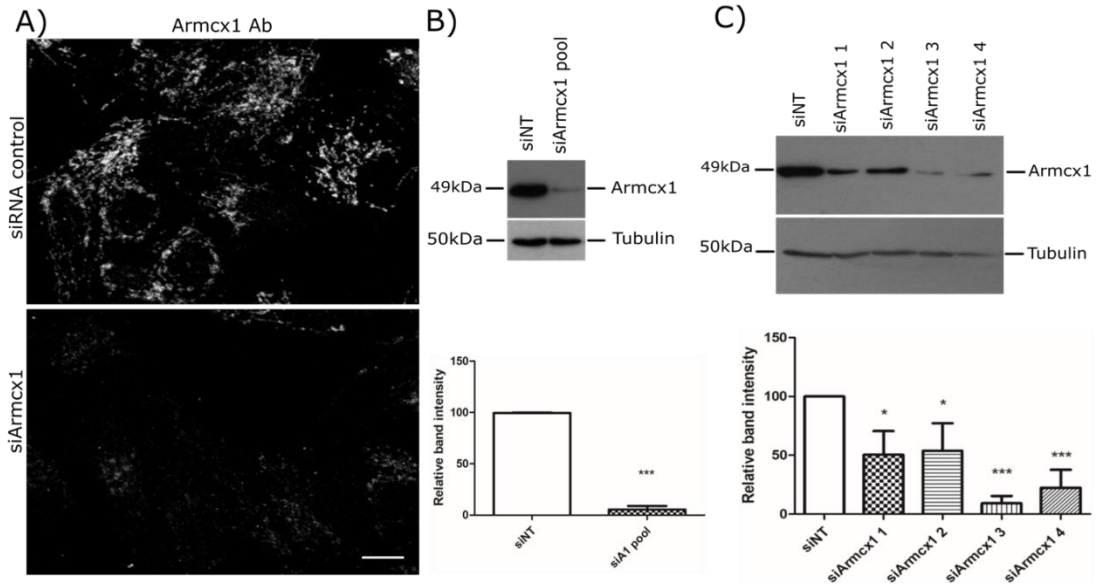

Figure 4.7 Armcx1 antibody validation by siRNA. A and B) Sub-confluent ARPE-19 cells were transfected with a pool of siRNA against Armcx1 (siArmcx1), or with a non-targeting control siRNA (siRNA control in A, siNT in B). **A)** 72 h after transfection, cells were fixed in methanol and stained via indirect immunofluorescence with primary antibody against Armcx1 (green). Images were taken with a ZEISS LSM700 confocal microscope, using a 63x oil objective. Scale bar = 10 µm **B)** Cell lysates prepared 72h post-transfection were analysed by Western blot. Quantification of 2 independent experiments is shown below, with statistical significance established by unpaired t-test (***p=0.0007). **C)** Sub-confluent ARPE-19 cells were transfected with four individual Armcx1-targeting siRNAs (siArmcx1 1-4) or a non-targeting control siRNA (siNT). Armcx1 expression was analysed by Western blot of cell lysates prepared 72h post-transfection. Densitometry quantification is shown below and represents 3 independent experiments; ONE-way ANOVA with Bonferroni post hoc analysis (*p<0.05, ***p<0.001) was used to establish a statistical significance, with tubulin used as a loading control.

4.3.2 ARMCX2 antibody validation by siRNA

Armcx2 antibody specificity was also validated by siRNA. Two different Armcx2 antibodies were validated: one for immunofluorescence and one for Western blot analysis, as we were unable to find one that is universal. A pool of four siRNAs against Armcx2 was tested to silence the endogenous expression level of Armcx2 in ARPE-19 cells. Following 72 h of siArmcx2 pool

transfection, endogenous Armcx2 levels were significantly reduced when compared to the control in both immunofluorescence and Western blot analysis (Figure 4.8 A, B). In addition, individual siRNAs were also tested separately to evaluate different levels of the knockdown and normalised to the loading control β-actin which levels remained unaffected between samples treated with non-targeting siRNA and siArmcx2. siArmcx2.4 resulted in the strongest knockdown of Armcx2 protein levels. (Figure 4.8 C). In fact, it looks as if pool efficiency is nearly entirely due to siARMCX2.4.

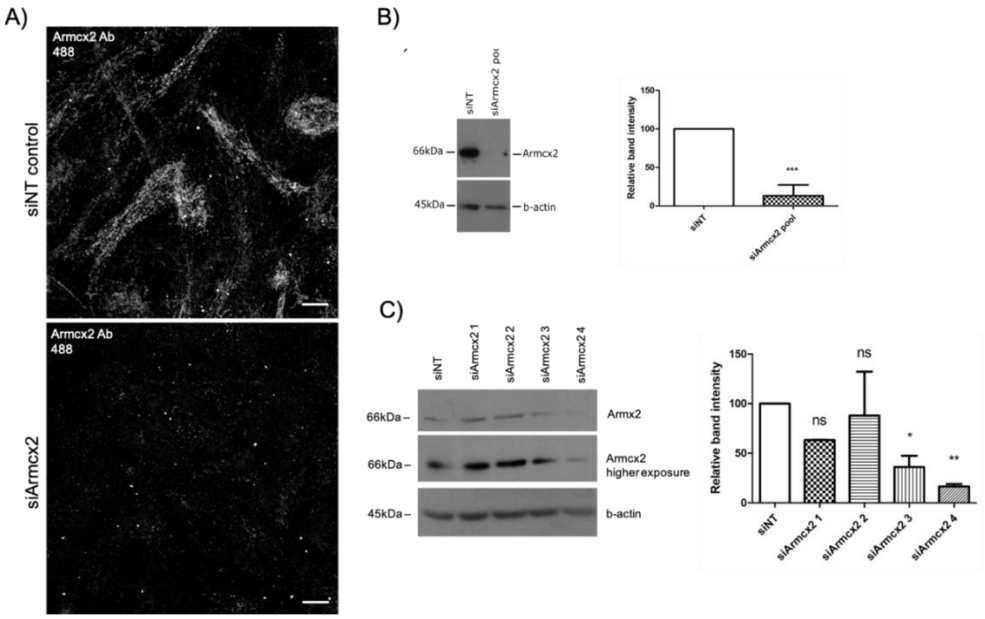

Figure 4.8 Validation of Armcx2 antibody by siRNA. A and B) Sub-confluent ARPE-19 cells were transfected with a pool of siRNA against Armcx2 (siArmcx2) or with non-targeting control siRNA (siNT control); **A)** 72 h after transfection, cells were fixed in methanol and stained via indirect immunofluorescence with primary antibody against Armcx2 (secondary antibody Alexa Fluor 488, green). Images were taken by a ZEISS LSM700 confocal microscopy 63x oil objective. **B)** Cell lysates prepared 72 h post transfection were analysed by Western blot. Quantification of two independent experiments is shown below with statistical significance established by unpaired t-test (***p<0.001). **C)** Sub-confluent cells were transfected with four individual Armcx2-targeting siRNA (siArmcx2 1-4) or non-targeting control siRNA (siNT control); Armcx2 expression was analysed by Western blot of cell lysates prepared 72 h post-transfection. Densitometry quantification is shown below and represents 3 independent experiments; ONE-way ANOVA with Bonferroni post hoc analysis (*p<0.05, ***p<0.001) was used to establish a statistical significance, with tubulin used as a loading control.

4.3.3 Cellular localisation of ARMCX1 and ARCMX2 in RPE

4.3.3.1 Endogenous ARMCX1 and ARMCX2 co-localise with mitochondria in non-differentiated and differentiated ARPE-19

Using these fully validated antibodies, we then studied the expression of Armcx1 and Armcx2 in RPE. We showed that all endogenous Armcx1 was detected in association with mitochondria in both non-differentiated and

differentiated ARPE-19 by confocal microscopy (Figure 4.9). Endogenous Armcx2 similarly co-localised with mitochondria in non-differentiated and differentiated ARPE-19 cells (Figure 4.10). Notably, endogenous Armcx2 staining was also apparent in some of the cell's nuclei and not always completely co-localised with mitochondrial marker Tom20.

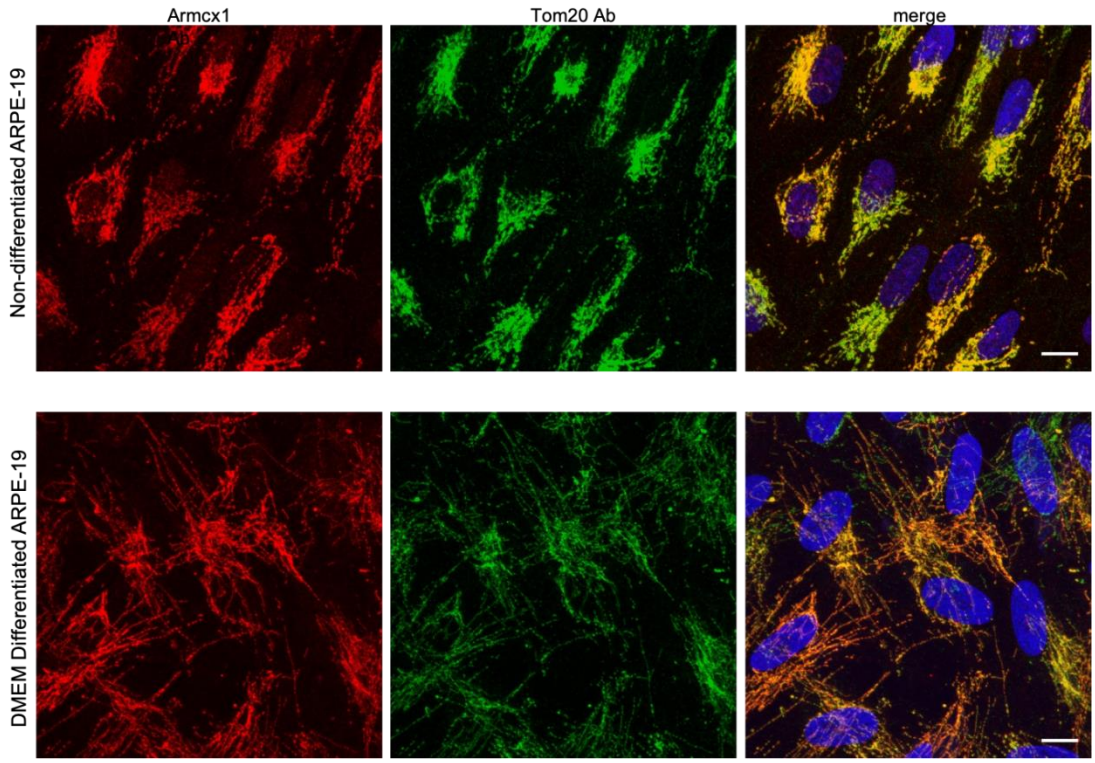

Figure 4.9 Endogenous Armcx1 co-localises with mitochondria in non-differentiated and differentiated ARPE-19 cells. Endogenous Armcx1 co-localisation was studied in non-differentiated (upper panels) and differentiated (>20 weeks) cells (lower panels) via indirect immunofluorescence; cells were fixed in methanol and co-stained with primary antibody against Armcx1 (secondary antibody Alexa Fluor 555, red) and the mitochondrial marker Tom20 (secondary antibody Alexa 488, green); merge image includes Hoechst staining (blue) which labels the nucleus; Scale bar = 10 μm; images were taken by a ZEISS LSM700 confocal microscopy 63x oil objective.

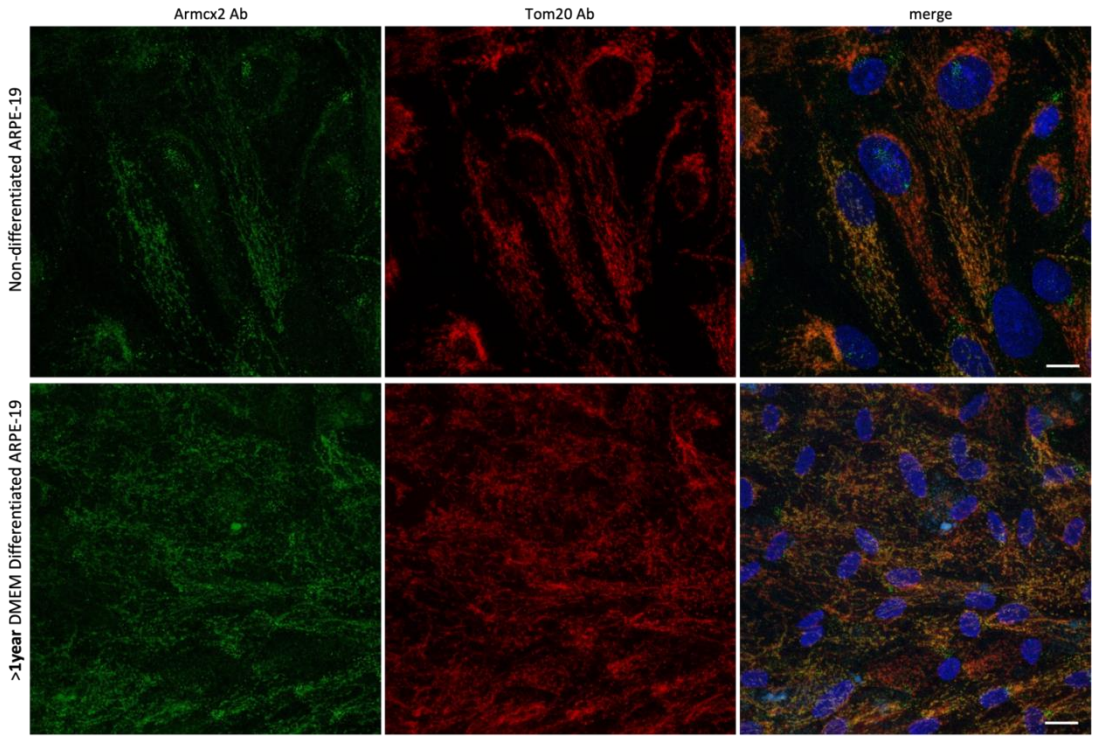

Figure 4.10 Endogenous Armcx2 co-localises with mitochondria in non-differentiated and differentiated ARPE-19 cells. Armcx2 co-localises with mitochondria in non-differentiated and differentiated ARPE-19 cells. Endogenous Armcx2 co-localisation was studied in non-differentiated (upper panels) and differentiated (>1 year) cells (lower panels) via indirect immunofluorescence; cells were fixed in methanol and co-stained with primary antibody against Armcx2 (secondary antibody Alexa Fluor 488, green) and the mitochondrial marker Tom20 (secondary antibody Alexa 555, red); merge image includes Hoechst staining (blue) which labels the nucleus; Scale bar = 10 µm; images were taken by a ZEISS LSM700 confocal microscopy 63x oil objective.

4.3.3.2 ARMCX1 and ARMCX2 localised with RPE65 marker in human control and AMD donor eyes

Next, we analysed if Armcx1 and Armcx2 were expressed in RPE *in situ*. For this, we examined their localisation in the RPE layer in sections of post-mortem human eyes. Sections from control individuals as well as from patients with AMD were analysed by immunohistochemistry. The presence of Armcx1 staining in RPE65-positive cells in both control and AMD sections (Figure 4.11)

indicates that Armcx1 is expressed in the RPE *in vivo* as well as in cultured RPE cell lines.

Furthermore, strong staining of Armcx1 was also observed in the ganglionic cell layer (GCL) of the non-diseased human retinal sections suggesting that this protein may be important for this particular cell layer too (Figure 4.11 A).

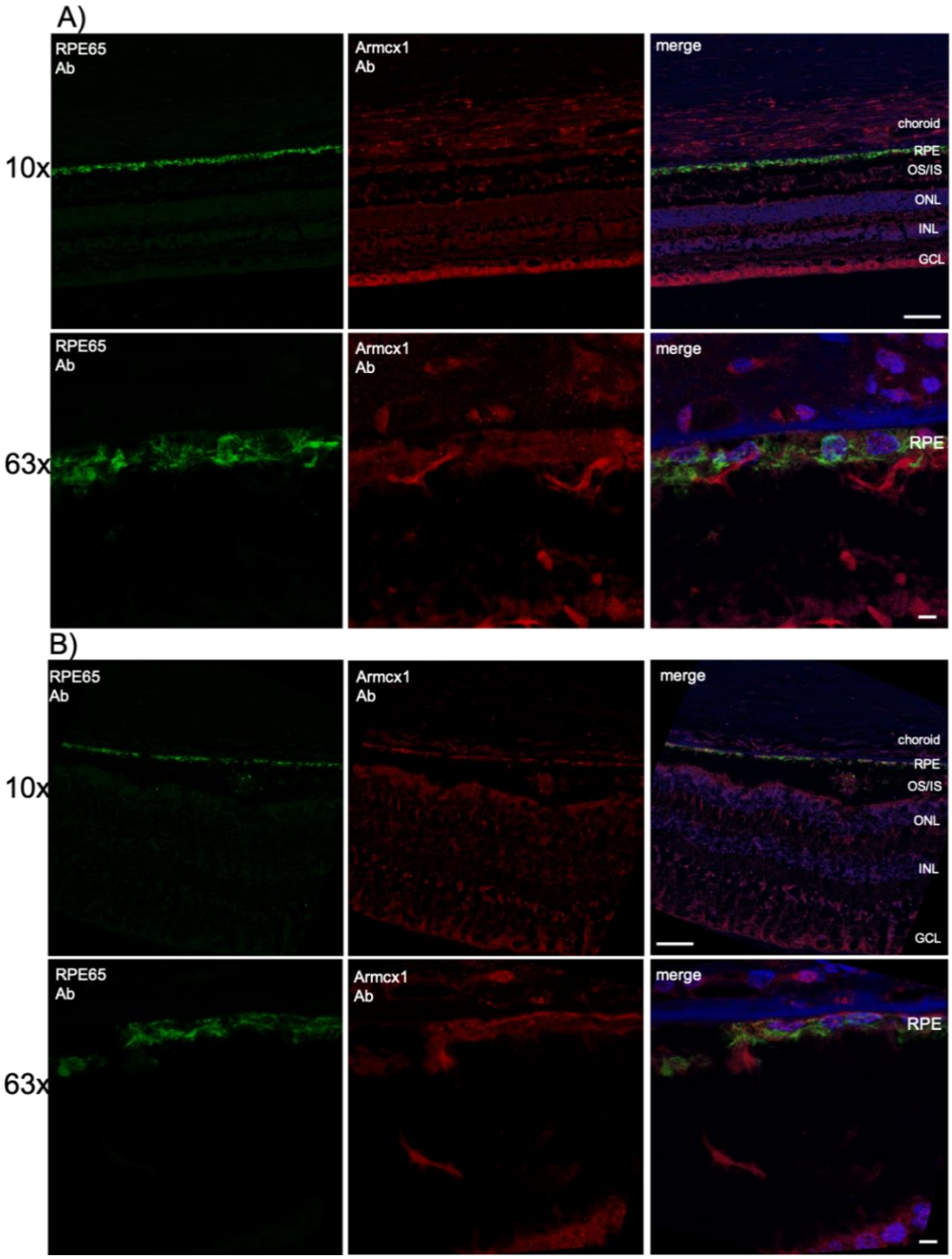

Figure 4.11 Localisation of Armcx1 in Human retinal sections. Indirect immunofluorescence was performed on paraffin embedded retinal tissue of control (A) and AMD (B) diagnosed individuals; sections were co-stained with primary Armcx1 antibody (secondary Alexa 555, red) and RPE65 antibody (secondary Alexa 488, green) and cell nuclei were stained in blue shown on the merge images; the following layers are identified: ganglion cell layer (GCL), inner nuclear layer (INL), outer nuclear layer (ONL), outer/inner photoreceptor segment (ON/IS) two different magnifications were taken at 10x (upper panels) and 63x (lower panels) by a ZEISS LSM700 confocal microscopy; upper panels scale bar = 100 µm, lower panels scale bar = 10 µm.

We also detected Armcx2 immunofluorescent staining in RPE65-positive cells in both control and AMD paraffin sections (Figure 4.12). In contrast to Armcx1, Armcx2 staining was specific to the RPE, with no staining observed in other cellular compartments in the retina.

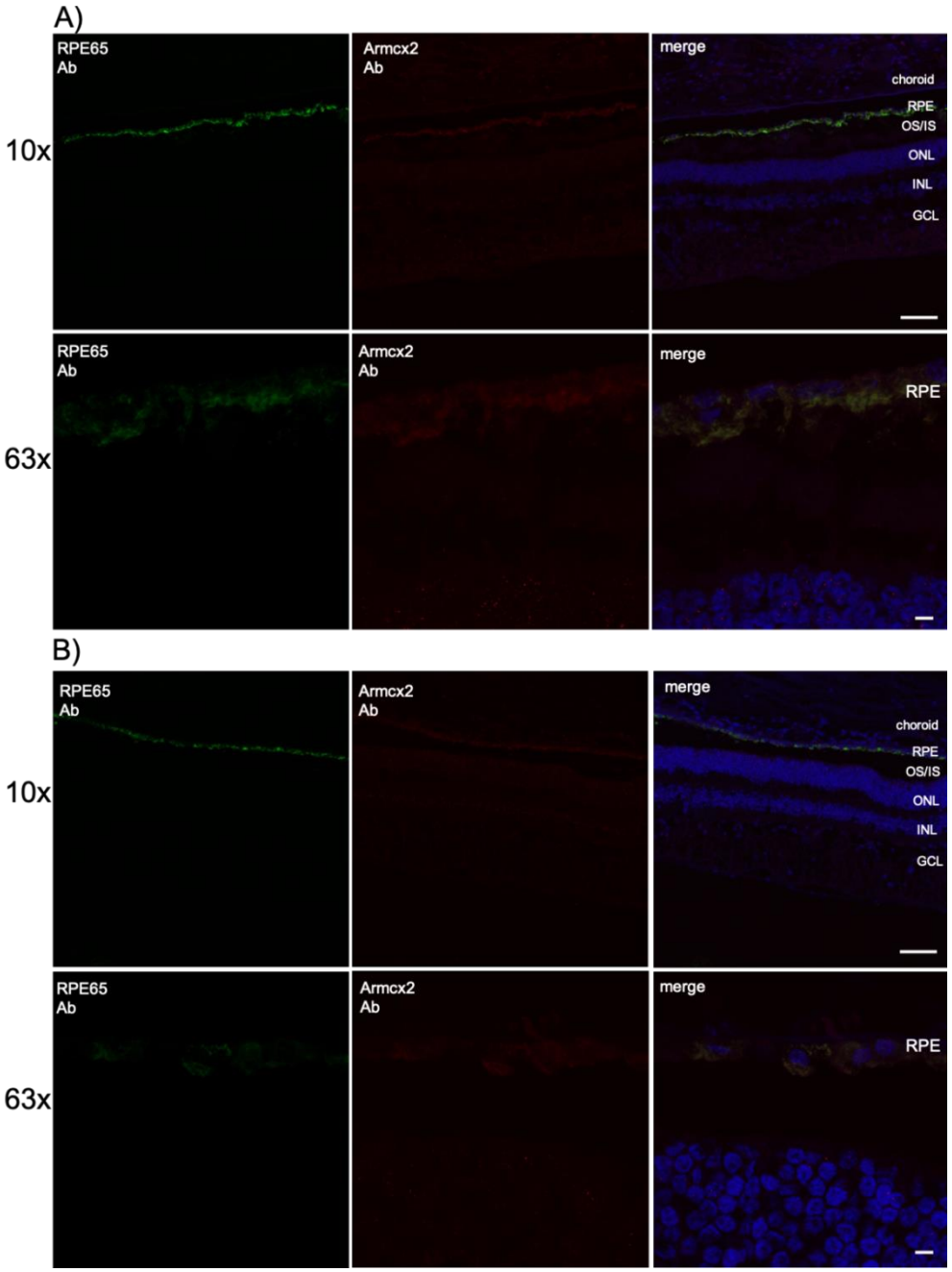

Figure 4.12 Localisation of Armcx2 in Human retinal sections. Indirect immunofluorescence was performed on paraffin embedded retinal tissue from control (A) and AMD (B) diagnosed individuals; sections were co-stained with primary Armcx2 antibody (secondary Alexa 555, red) and RPE65 antibody (secondary Alexa 488, green) and cell nuclei were stained in blue shown on the merge images; the following layers are identified: ganglion cell layer (GCL), inner nuclear layer (INL), outer nuclear layer (ONL), outer/inner photoreceptor segment (ON/IS) two different magnifications were taken at 10x (upper panels) and 63x (lower panels) by a ZEISS LSM700 confocal microscopy; upper panels scale bar = 100 µm, lower panels scale bar = 10 µm.

4.4 Discussion

The Armcx family has been described as mitochondria-associated proteins in neurons (López-Doménech et al., 2012). Indeed, exogenous expression of Armcx1, 2, 3 and 6 in the ARPE-19 cells showed strong association with mitochondria. We fully validated the predicted Armcx MTS by N-terminal truncations of a conserved N-terminal region that included the MTS relevant basic amino acids (lysine and/or arginine) and was predicted to form alpha helices. Deletion of the putative MTS domain of Armcx proteins abolished mitochondrial targeting, with the mutant protein instead being distributed through the cytoplasm and nucleus.

Exogenously expressed full length Armcx1 localised specifically to mitochondria in non-differentiated ARPE-19. Notably, all Armcx members except Armcx6 possess a NLS located downstream from the MTS. Occasionally, there were cells expressing Armcx1WT in the nucleus in addition to the mitochondrial localisation, which indicates a functional NLS, however it appears that the MTS is dominant. Furthermore, indeed, the appearance of the Armcx MTS mutants in the nucleus could be due to short translational product following the removal of the MTS, which possesses only the NLS. Nevertheless, Armcx MTS mutants have their TM domains interrupted by the N-termini deletion, they exhibited some plasma membrane localisation, suggesting Armcx proteins associate with TM proteins or the membrane in RPE cells. Importantly, this was not true only for Armcx1 MTS mutant expressed in differentiated cells where it revealed only nuclear localisation.

Exogenously expressed Armcx2 also co-localised with mitochondrial markers and caused mitochondrial aggregation in ARPE-19 cells, consistent with the mitochondrial aggregation shown to result from Armcx overexpression in neurons (López-Doménech et al., 2012). Notably, endogenous Armcx2 also showed strong nuclear alongside mitochondrial staining. However, this endogenous staining was never fully validated by siRNA in immunostaining analysis, whilst the same antibody delivered clear results in immunoblots. Subsequently, another Armcx2 antibody was validated for immunostaining analysis only.

Full length Armcx3 expression in non-differentiated ARPE-19 showed multiple sub-cellular compartmentalisations. Notably, endogenously Armcx3 showed no nuclear staining in differentiated cells. However, this antibody was not validated by siRNA, thus cannot confirm its endogenous subcellular location. Importantly, Armcx3 has been previously shown to be located at different sub-cellular sites in neurons (López-Doménech et al., 2012) and to interact with transcription factors (Mou et al., 2009) suggesting various biological functions. Alternative mRNA splicing could be the reason for differential localisation, where two or more translational products with the same function are produced, but with changes in the amino acid residues that result into different localisation targeting sequences (Yogev and Pines, 2011, Carrie and Whelan, 2013, Bauer et al., 2015). However, differential splicing has not yet been explored for Armcx. Alternatively, maybe saturation of mitochondrial Armcx3 had been reached following strong exogenous expression.

In our study we detected the expression of full length and mutant Armcx6 in the nucleus, despite the lack of a NLS, which suggests a potential recruitment of Armcx6 to the nucleus via another unknown mechanism. Moreover, endogenous Armcx6 also showed strong nuclear staining. One possible explanation of this “dual targeting” of Armcx6 could be due to a protein-protein interaction. It is well known that Arm repeats contribute to protein-protein interactions (see below), however no interactions of Armcx6 have been documented so far.

All Armcx family members contain a C-terminal armadillo domain consisting of up to six repeats of a highly conserved 42-amino acid motif known to be important in protein- protein interactions (Hatzfeld, 1999, Mou et al., 2009). In 2009 Mou et al have shown that Armcx3 binds Sox10 via its Arm repeats (Mou et al., 2009). Moreover, Armcx3 C-terminus which contains the arm repeats was shown to be responsible for the interaction of Armcx3 with Miro1 in mitochondria in a Ca^{2+} dependent manner. Therefore, the detection of exogenously expressed Armcx proteins in different parts of the cells could also be due to interactions with other sub-cellular proteins.

All expressed Armcx-GFP constructs co-localised only with mitochondria in differentiated ARPE- 19, suggesting some importance for Armcx in the mitochondrial network of mature RPE. The mitochondria in differentiated APRE-19 appeared more elongated and dispersed than in non-differentiated cells. Dynamic changes of the mitochondrial shape have been reported during induced pluripotent stem cells reprogramming and differentiation. During reprogramming mitochondria appeared fragmented but become elongated in

the differentiated state (Seo et al., 2018). In this regards it is interesting that a previous study has shown that overexpression of Armcx3 stops the proliferation of progenitor neuronal cells and induces their differentiation (Mirra et al., 2016). Elsewhere, Armcx2 expression has been shown to play a role in the development of testicular cell differentiation (Smith et al., 2005). In respect to this, Armcx activity is regulated by non- canonical Wnt signalling (Serrat et al., 2013), which is also important for RPE maturation (Kim et al., 2015).

Having expressed full length Armcx-GFP constructs and studied their mitochondrial association, we aimed to distinguish and focus on the members that showed the strongest mitochondrial phenotype in RPE. Armcx3 and 6 showed heterogeneous localisation profiles in ARPE-19 and no strong mitochondrial phenotype, hence they were no longer investigated in this project. In contrast, we identified robust mitochondrial localisation for both over-expressed and endogenous Armcx1 and 2 that was dependent on their MTS. Importantly, Armcx1 and 2 localised to mitochondria in differentiated, as well as non-differentiated RPE, consistent with potential roles in regulating mitochondrial network in RPE. In agreement, Armcx1 and Armcx2 were found localised in the RPE layer of human retinal sections, further supporting a role of these proteins in this retinal layer.

A mitochondrial clustering phenotype was associated with Armcx2 overexpression. The role of Amcx1 and 2 in mitochondrial function is poorly understood, thus we aimed to further investigate this.

Furthermore, for the first time we showed Armcx1 and Armcx2 association with mitochondria in mature RPE cells. It must be noted here, due to loss of all highly differentiated ARPE-19 cell cultures during Covid-19 pandemic, we were unable to repeat, as well as to continue, some experiments that were initially planned to be done in mature RPE cells.

Chapter 5 Results: Effects of ARMCX1 and ARMCX2 knockdowns on mitochondria in RPE

We rely on a limited knowledge about the function of Armcx proteins. Lopez-Domenech et al have contributed to a better understanding of Armcx3 function, however their research was mainly restricted to neurones and did not look at potential functional differences of the other ARMCX family members. Moreover, another angle of research that has not been explored yet is whether Armcx have preserved their ancestral Armc10 function, or they evolved into new physiological roles. The function of Armc10 is described to be important for the neuronal development in the chicken spinal cord partially via inhibiting the canonical Wnt/b-catenin pathway, which is a major player in inducing proliferation of the dorsal spinal progenitor cells (Mirra et al., 2016). Moreover, Armc10 mRNA was found widely expressed in the nervous system during zebrafish early embryonic development (Liu et al., 2017). A recent study has found Armc10 to play a role in mitochondrial dynamics and to interact with and to be phosphorylated by AMPK, an important regulator of cellular energy homeostasis (Chen et al., 2019). In addition, Heo et al found in a large proteomic study that Armcx2, 3 and Armc10 form a cluster from a depolarized mitochondria-autophagosome synapse, which could suggest that they fulfil similar functions (Heo et al., 2019). Therefore, research thus far indicates a role for Armc10 in development of the nervous system and also to be

conserved in this aspect, and similarly to Armcx3 to be involved in mitochondrial dynamics and/or mitophagy *in vitro*.

To this point, we showed Armcx1 and Armcx2 genes encode mitochondrial targeting proteins and their endogenous expression in ARPE-19 cells. Here, in this chapter we explored further the effects of Armcx1 and Armcx2 on mitochondria. In addition, we investigated whether the ancestral Armc10 from marsupial clade can rescue Armcx1 and Armcx2 functions.

Exploring mitochondrial network and dynamics via fluorescence imaging has been widely used in research. Initially, quantification methods were only based on the appearance of mitochondria categorised as “fused”, “fragmented” and “intermediate” (Mitra et al., 2009). More recent approaches include software-based analysis, which allow better assessment and quantitation of the dynamic mitochondrial network (Valente et al., 2017). However, some of these approaches require machine-learning practices and access to commercial software that are cost dependent. Among the open-source alternatives there are limitations based on the type of mitochondrial phenotype studied; for example, Mito-Morphology Image macro is designed to capture elliptical shapes only, however mitochondria exist also in elongated and tubular networks (Dagda et al., 2009); other applications such as MitoMap uses only three-dimensional datasets (Schneider et al., 2012), which are not always available. Recently, Valente et al developed the Mitochondrial Network Analysis tool (MiNa) adapted to the ImageJ platform and freely available for use online. MiNa is designed to distinguish both elongated/tubular and individual/fragmented mitochondria and quantify their numbers (Valente et al.,

2017). Therefore, we used MiNa macro as an analytic tool to investigate the effect of Armcx1 and Armcx2 on the mitochondrial network in RPE cells.

5.1 ARMCX1 and ARMCX2 have different effects on mitochondrial network

5.1.1 ARMCX1 and ARMCX2 knockdown resulted in single, isolated mitochondrial network

As shown in the previous chapter endogenous Armcx1 and Armcx2 were nearly exclusively localised to mitochondria in cultured ARPE-19 cells. Furthermore, ectopic expression of both genes as GFP fusions also induced morphological alterations of the mitochondrial network, which were particularly pronounced following expression of Armcx2-GFP. To investigate potential functions in maintaining a healthy and stable mitochondrial network, these were analysed following silencing of Armcx1 and Armcx2.

In cells treated with non-targeting control siRNA mitochondria appeared mostly packed around the nucleus or if found at more peripheral areas, they resembled elongated tubular network (Figure 5.1, 5.2 upper panels). Interestingly, the mitochondrial network appeared less continuous and more fragmented in cells depleted of Armcx1 (Figure 5.1 lower panels).

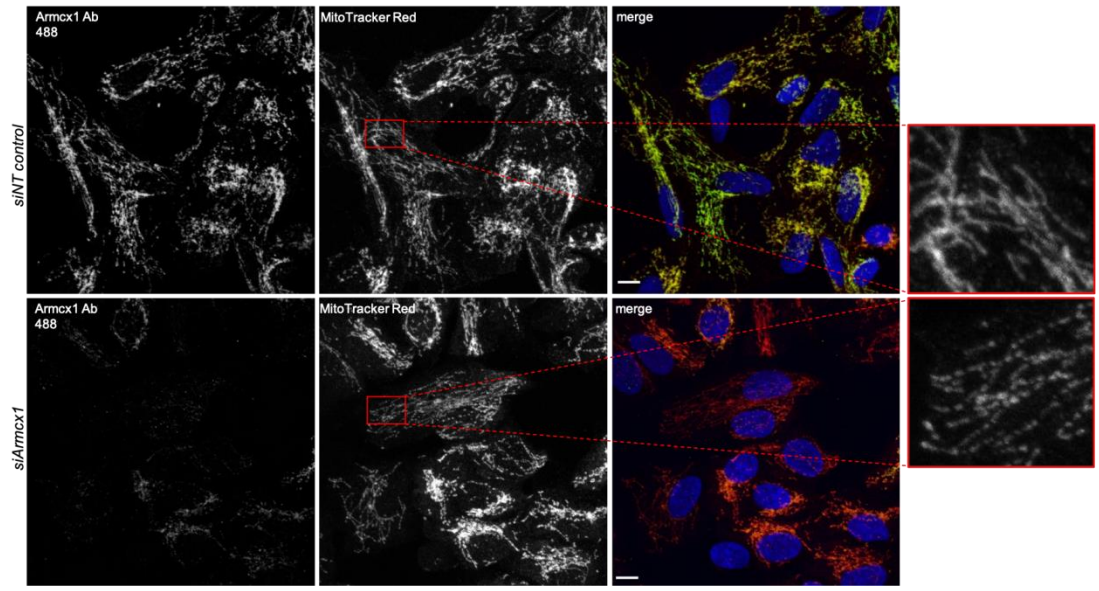

Figure 5.1 The effect of Armcx1 knockdown on mitochondrial network in non-differentiated ARPE-19. Non- differentiated ARPE-19 cells were transfected with a pools of non-targeting control siRNA (siRNA control – upper panels) or siRNA targeting Armcx1 (siArmcx1 – lower panels); 72h after transfection, cells were stained with MitoTracker (red) for mitochondrial visualisation before methanol fixation; Armcx1 staining was by indirect immunofluorescence with primary antibody against Armcx1 (secondary antibody Alexa Fluor 488, green); red boxes show zoomed areas for better visualisation. Images were taken by a ZEISS LSM700 confocal microscopy 63x oil objective; scale bar = 10 μm.

Notably, only the cells that have completely lost Armcx1 showed this discontinuity of the mitochondrial network, whereas cells with some residual Armcx1 staining appeared to retain perinuclear mitochondria.

Moreover, cells treated with siRNA against Armcx2 exhibited a strong mitochondrial phenotype, where mitochondria appeared rounded, as single mitochondria and lack the elongated network seen in control cells (Figure 5.2 lower panels). However, in contrast to siArmcx1 phenotype, mitochondria appear more condensed and accompanied by a complete lack of filamentous characteristics within the cells. In addition, mitochondria in siArmcx2

transfected cells looked enlarged compared with those observed in Armcx1 knockdown cells.

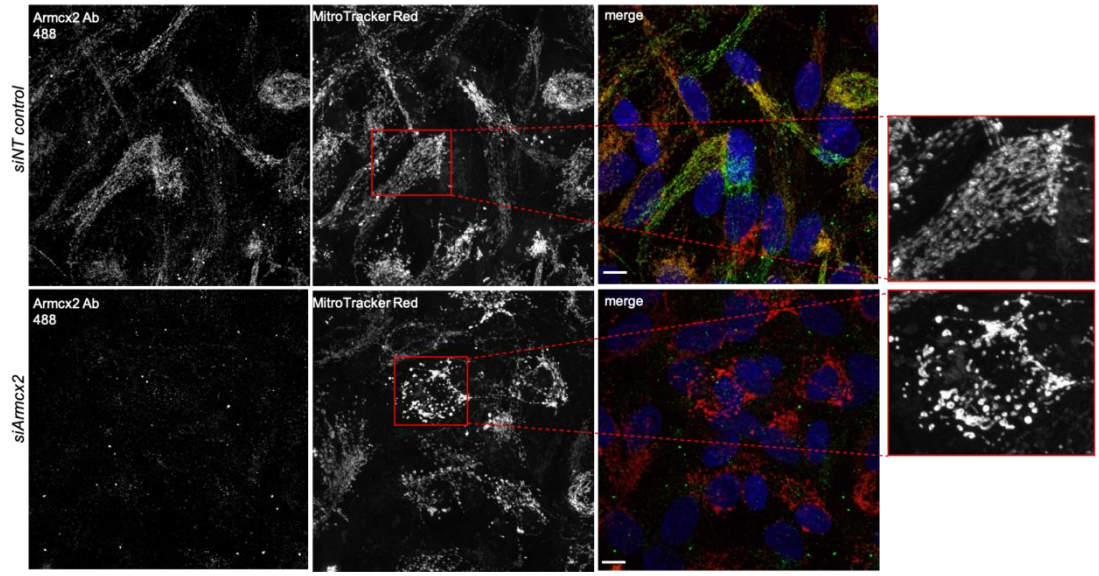

Figure 5.2 The effect of Armcx2 knockdown on mitochondrial network in non-differentiated ARPE-19. Non- differentiated ARPE-19 cells were transfected with pools of non-targeting control siRNA (siRNA control – upper panels) or of siRNA targeting Armcx2 (siArmcx2 – lower panels); 72h after transfection, cells were stained with MitoTracker (red) for mitochondrial visualisation before methanol fixation; Armcx2 staining was by indirect immunofluorescence with primary antibody against Armcx2 (secondary antibody Alexa Fluor 488, green); red boxes show zoomed areas for better visualisation. Images were taken by a ZEISS LSM700 confocal microscopy 63x oil objective; scale bar = 10 μm.

Since Armcx1 and Armcx2 knockdowns exhibited two different mitochondrial phenotypes, this clearly indicated that they fulfil distinctive functions in ARPE-19 cells. In accordance with these mitochondrial changes, we initially performed a more subjective quantification method by scoring cells based on a specific mitochondrial phenotype. In this case we distinguished three types of mitochondria – small punctate mitochondria, more rounded and isolated and elongated/tubular (Figure 5.3).

The elongated mitochondrial network was observed mostly in the control cells and least detected in the Armcx2 knockdown cells. In cells treated with siRNA against Armcx1, mitochondria were mainly small and punctate resembling “beads-on-a-string” with very little elongated mitochondria. The large and round mitochondria were identified mainly in the cells transfected with siRNA against Arcmx2 (Figure 5.3). In the non-targeting control siRNA cells, we observed rarely small punctate and/or big and round mitochondria.

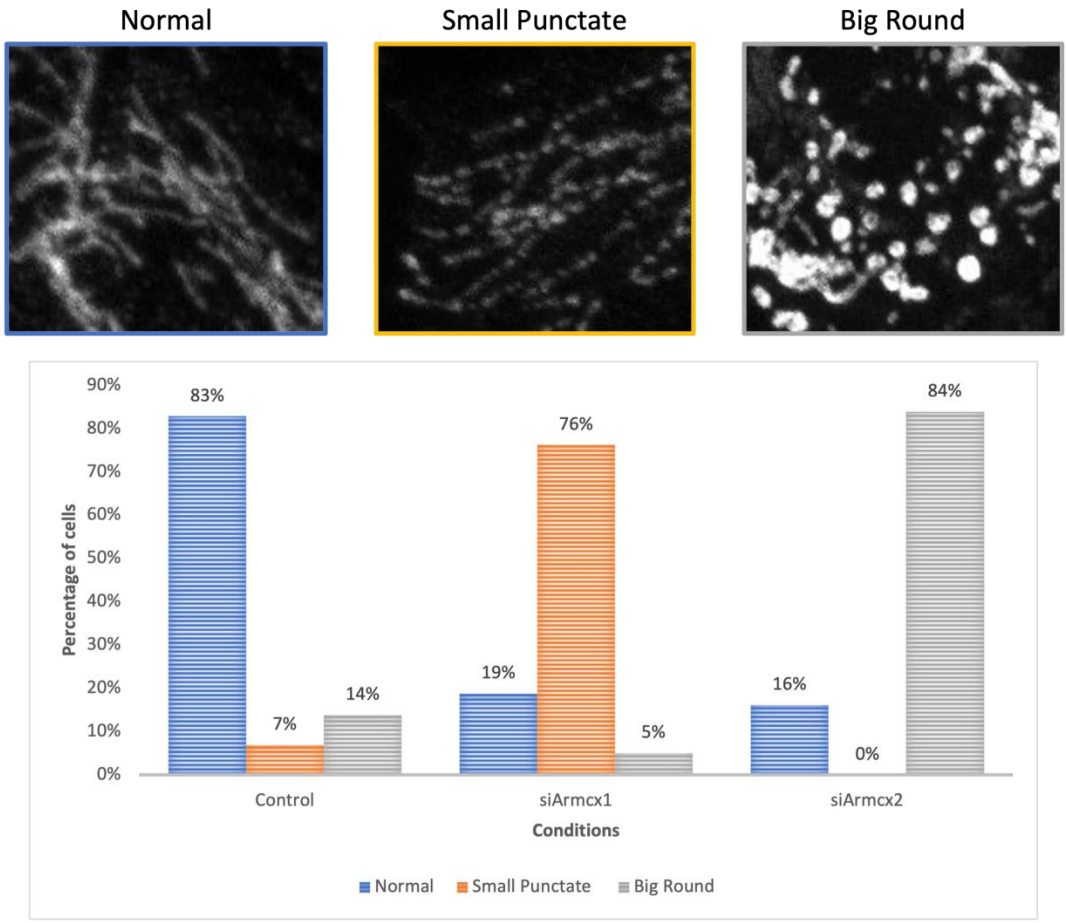

Figure 5.3 Quantification and graphical representation of the mitochondrial phenotypes induced upon Armcx1 and Armcx2 knockdowns. Cells were scored depending on the mitochondrial phenotype they have in control, siArmcx1 and siArmcx2 conditions. Between 30-80 cells from two independent experiments were counted and the graph represents percentage of cells possessing specific mitochondrial phenotype (normal mitochondria, small punctate ("beads-on-a-string"-like) or big round mitochondria).

Furthermore, we used a less subjective method of quantification of the mitochondrial phenotype caused by the lack of Armcx1 and Amrcx2 in APRE-19 cells. According to the observed mitochondrial phenotype and the quality of images we have, we chose the MiNa macro toolset. In the knockdown treated cells, we analysed only those cells which clearly lacked endogenous staining and thus the silencing had worked. Figure 5.4 shows the method of image processing and final morphological model prior quantitation analysis.

Image pre-processing steps are carried out to sharpen the quality of images and to subtract any noise that may present from the fluorescent labelling.

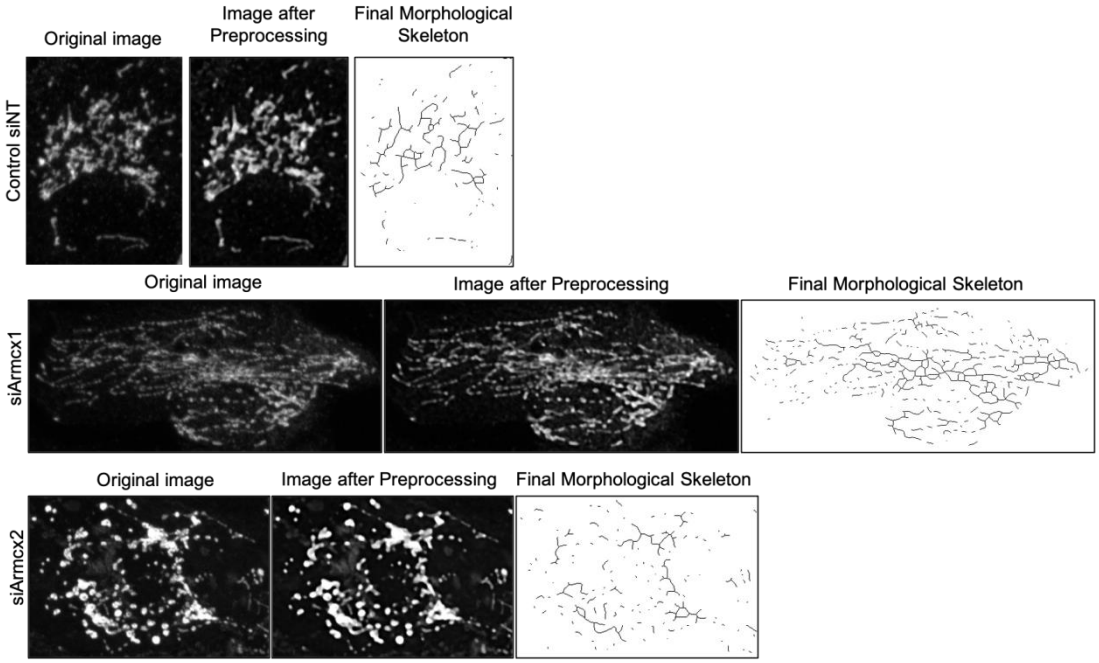

Figure 5.4 Preparation for mitochondrial network feature analysis by ImageJ macro–Mitochondrial Network Analysis (MiNA) toolset. In the MiNA workflow images from non-targeting control siRNA (control siNT), siArmcx1 and siArmcx2 were pre-processed to improve quality before binarizing (not shown) and skeletonizing which is the final step before quantification; subsequently the descriptive parameters are calculated from the skeletonised image. The image preparation was strictly followed as described in Valente et al., 2017 (Valente et al., 2017). MiNa is freely available at https://github.com/StuartLab.

Following MiNa analysis, we observed an increase in the total, individual and mitochondrial networks in Armcx2 knockdown cells when compared to the control cells. There was not a significant change in the mitochondrial features of Armcx1 knockdown cells (Figure 5.5B). There was no change also in the mitochondrial branch length in cells lacking Armcx1, in contrast to Armcx2 knockdown cells, where their length was decreased (Figure 5.5C).

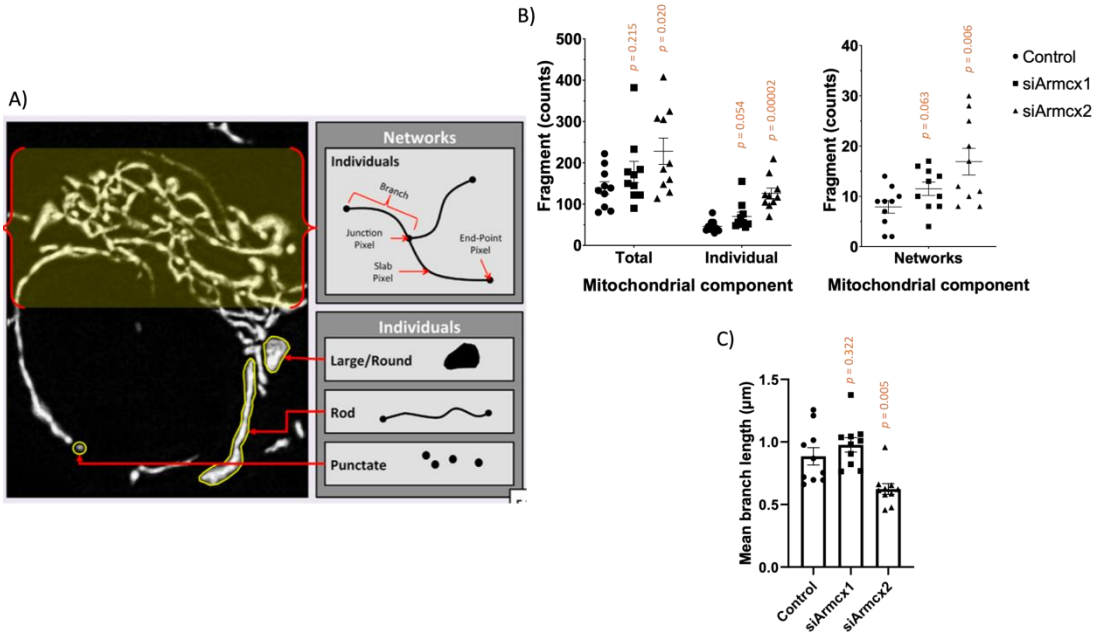

Figure 5.5 Common mitochondrial network features recognised and analysed by MiNa. **A)** An example image with schematic representation of the types of mitochondrial features that the micro tool recognises – networks and individuals; Individuals are punctate (a single pixel in the skeletonized image), rods (unbranched features with two or more pixels), and round structures (which are reduced to rods or rarely as small networks); Networks are structures with at least a single node and three branches. The figure is adapted from Valente et al., 2017. **B)** Quantification analysis of the number (counts) of mitochondrial components (total, individual and networks) between control siRNA (noted with black circle), siArmcx1 (noted with black squares) and siArmcx2 (noted with black triangle); 10 cells were analysed from each condition. **C)** Column graph representing quantification of the mean branch length (in µm) of mitochondrial structures in control siRNA, siArmcx1 and siArmcx2.

Moreover, we looked closer at mitochondria and more particularly their length by conventional electron microscopy in cells lacking Armcx1 and Armcx2. We observed decreased mitochondrial lengths in cells treated with siArmcx1(Figure 5.6 siArmcx1), which was expected since we revealed more small punctate mitochondria in these cells by immunofluorescence analysis compared to the control cells. Consistent with our immunofluorescence-based observations, in Armcx2-depleted cells, mitochondria were less tubular and more rounded (Figure 5.6, siArmcx2). However, whereas mitochondria

appeared larger by immunofluorescent analysis in Armcx2 knockdown cells than those lacking Armcx1, by EM mitochondria in siArmcx2 measured slightly smaller (Figure 5.6 B). Overall, this could be due to the presence of more elongated mitochondria in Armcx1 knockdown cells than in Armcx2 knockdown and/or incomplete knockdown in some siArmcx1 treated cells.

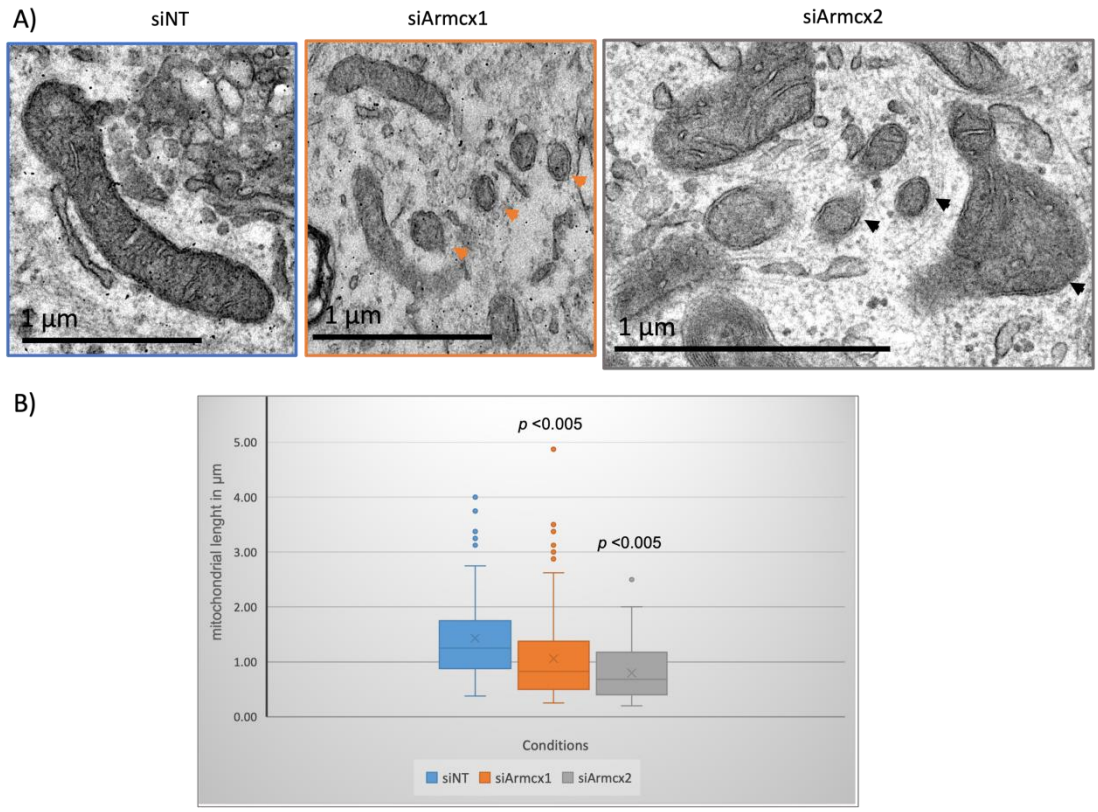

Figure 5.6 Mitochondrial length in Armcx1 and Armcx2 knockdown. **A)** Electron microscopy micrograph of ARPE-19 cells treated with control siRNA (siNT), siArmcx1 or siArmcx2; arrow heads indicate small mitochondria; difference in the scale bar in siArmcx2 is due to images being taken at a higher magnification. **B)** Box plot show quantification of the mitochondrial length (µm) in control, siArmcx1 and siArmcx2; between 118 – 261 mitochondria were measured from 7 to 10 cells per condition; experiment is n=1; p values are indicated on the plot.

5.1.2 Mitochondrial mobility is affected differently by ARMCX1 and 2 knockdowns

Mitochondria are dynamic organelles which travel to different sub-cellular locations to meet specific energy demands of the cell (Shen et al., 2018). Since we observed phenotypic changes in mitochondria upon silencing Armcx1 and Armcx2 in RPE cells, we next wanted to examine whether mitochondrial mobility was affected. To address this, we used live-cell imaging. Armcx1 and Armcx2 knockdown cells were transfected with mitochondrial-targeted DsRed plasmid and cells were recorded over a 10-min period (Figure 5.7). Individual mitochondria were tracked, and the overall velocity was calculated by using the Manual Tracking plugin for ImageJ. Mitochondrial movement was increased in cells lacking Armcx1 when compared to control cells. In support to this, previous data in our lab showed that Amrcx1 overexpression decreased mitochondrial motility in ARPE-19 cells (Figure 9.2 in Appendix). Interestingly, Armcx2 knockdown caused less mitochondrial mobility (Figure 5.7), although previously Armcx2 overexpression had resulted in decreased movements (Figure 9.2 in Appendix). So far measurements have been conducted from a single experiment, thus further knockdowns are needed for firm conclusions.

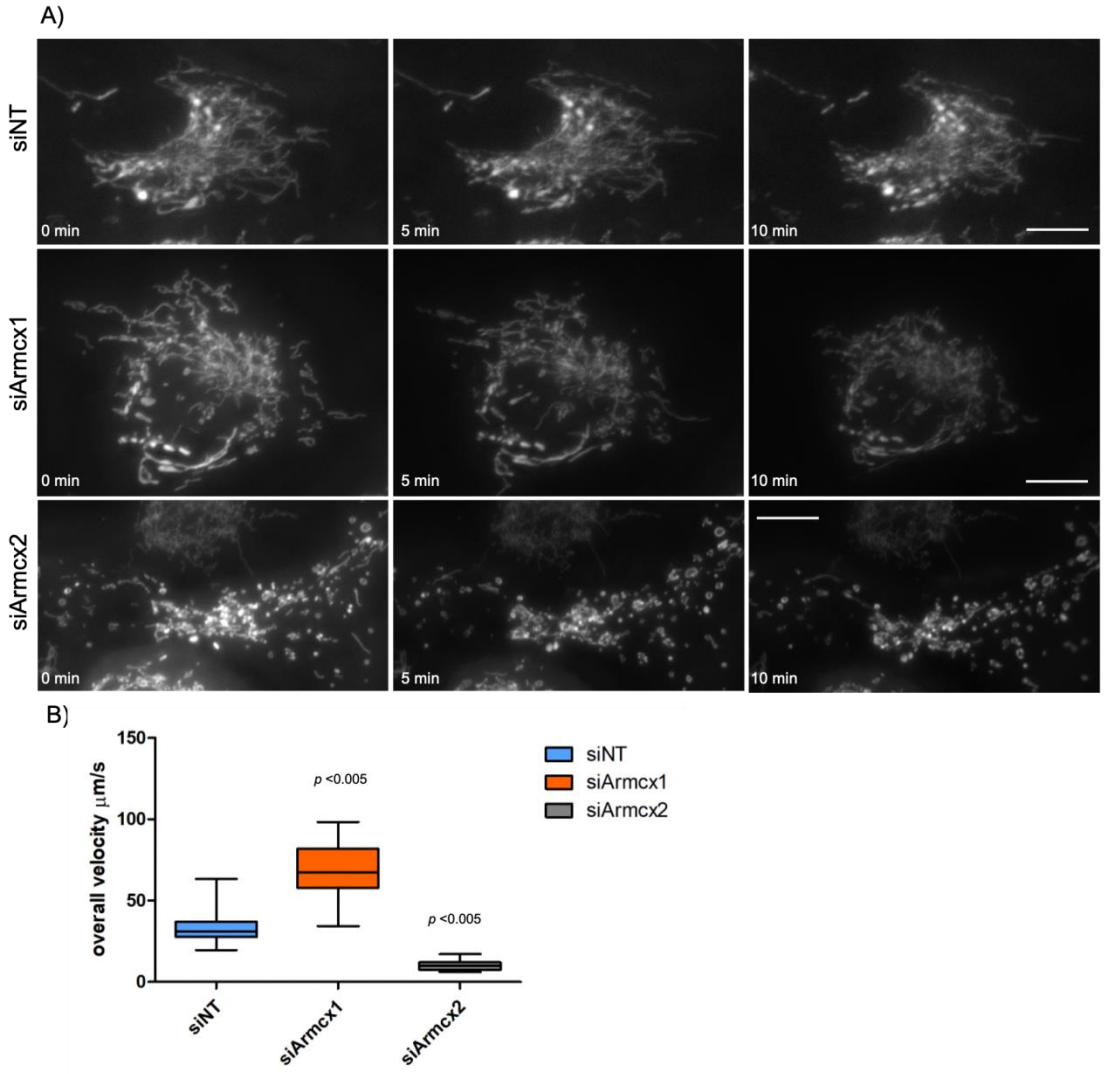

Figure 5.7 Armcx1 and Armcx2 affect mitochondrial motility differently. **A)** Stills from time-lapse live cell fluorescent microscopy of ARPE-19 cells treated with non-targeting control siRNA (siNT), or siRNA targeting Armcx1 (siArmcx1) or Armcx2 (siArmcx2). 72 h after siRNA transfection, cells were co-transfected with 1 µg of MitoDsRed plasmid for mitochondrial visualisation in live cells; time lapse videos were taken after 24 h. Mitochondrial movements can be seen over time at 0 min, 5 min and 10 min in control, siArmcx1 and siArmcx2; scale bar = 10 µm; **B)** Box plot displays results from Manual Tracking plugin used to trace mitochondrial movements in time (overall velocity travelled expressed as µm per second). At least 3 mitochondria were counted per cell and overall cell count was between 15-30 per condition; n=1; p values are indicated on the plot.

5.2 Compensatory mechanism by marsupial ARMCX

5.2.1 The rescue effects of marsupial ARMC10 over ARMCX1 and ARMCX2 knockdown mitochondrial phenotypes

Since we established such strong mitochondrial phenotypes when Armcx1 or Armcx2 were silenced, we were interested in revealing whether their ancestral gene marsupial Armc10 can rescue these phenotypes. This can indicate whether the Armc10 function is retained during evolution of the Armcx members in Eutheria or novel functions have emerged. To study this, we expressed exogenously the full length of marsupial Armc10 fused to the C-terminus of a EGFP carrying plasmid in Armcx1 and Armcx2 knockdown. Similarly, to Armcx-GFP, marsupial Armc10-GFP expression was found co-localised to mitochondria in non-differentiated ARPE-19 cells (Figure 5.8 A). The ectopic expression of marsupial Armc10 appeared unable to rescue the "beads-on-a-string" mitochondrial phenotype caused by the lack of Armcx1 based on the immunofluorescent analysis (Figure 5.8 B). In addition, MiNa analysis showed no significant differences among mitochondrial components between siArmcx1 treated cells and control siRNA expressing marsupial Armc10 (Figure 5.9), similarly to what we observed on the Armcx1 knockdown MiNa analysis (Figure 5.5). On the other hand, the exogenous expression of marsupial Armc10 in cells with reduced Armcx2 expression, did not exhibit the round and isolated mitochondria. In agreement to this, the numbers of individual and network mitochondria as well as the mean mitochondrial branch lengths were similar to the control based on MiNa analysis. Unfortunately, due to insufficient images of these experiments we are unable to conclude the

presence or absence of rescuing effect by Armc10 of the mitochondrial phenotypes caused by siArmcx1 and siArmcx2.

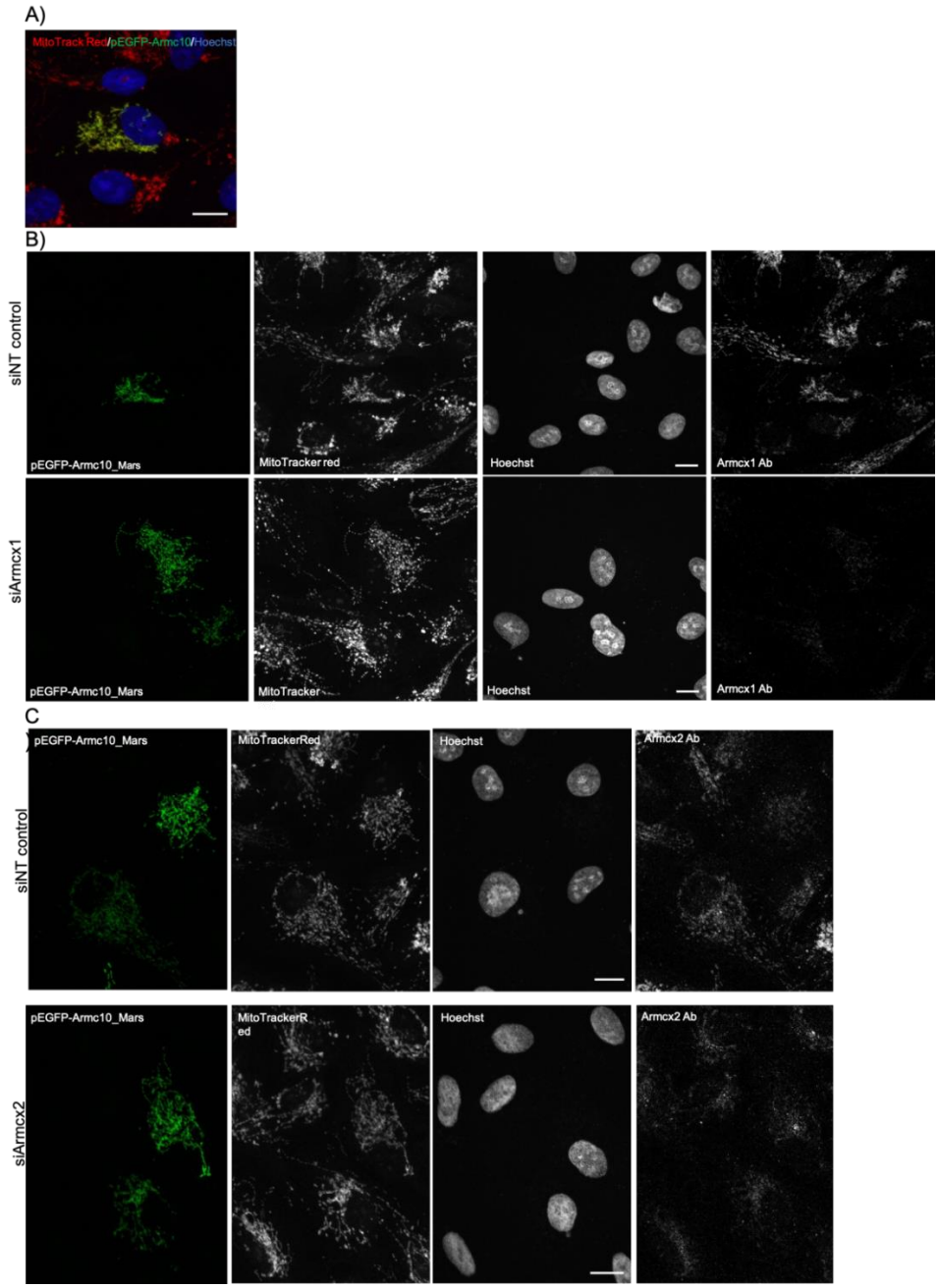

Figure 5.8 The effect of exogenous marsupial ARMC10 expression in Armcx1 or Armcx2-depleted RPE cells. A) marsupial Armc10 co-localises with mitochondria in RPE cells. B) 72 h after siRNA transfection against Armcx1, cells were transfected with 1 µg of pEGFP-Armc10 marsupial plasmid; 24 h later cells were stained with MitoTracker (red) before methanol fixation; Armcx1 staining was done by indirect immunofluorescence with primary antibody against Armcx1 (secondary antibody Alexa Fluor 647, far red). C) similar steps were undertaken as in B), but siArmcx2 transfection and Armcx2 antibody staining were carried out instead. Images were taken by a ZEISS LSM700 confocal microscopy 63x oil objective; scale bar = 10 µm.

Therefore, marsupial Armc10 exhibit rescuing function over the knockdown effect of Armcx2 effect on mitochondrial morphology. However, further experiments and analysis are required in order to make firm conclusions.

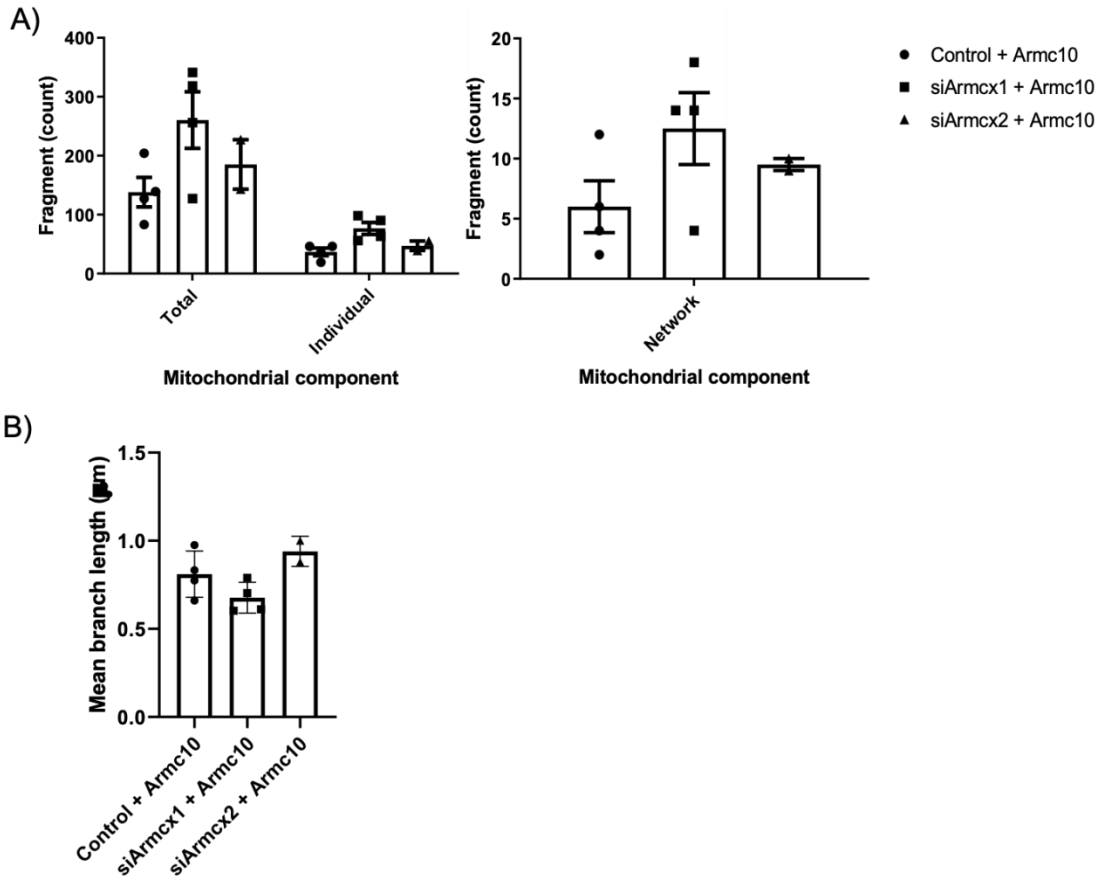

Figure 5.9 Quantification analysis of mitochondrial components by MiNa toolset. **A)** The number (counts) of mitochondrial components (total, individual and networks) between control siRNA (noted with black circle), siArmcx1 (noted with black squares) and siArmcx2 (noted with black triangle); 4 cells from siArmcx1 and 2 cells from siArmcx2 were analysed. **B)** Column graph representing quantification of the mean branch length (in µm) of mitochondrial structures in control siRNA, siArmcx1 and siArmcx2.

5.3 Discussion

In this chapter we have firmly established that Armcx1 and Armcx2 are involved in the regulation of the mitochondrial network in RPE cells. Following Armcx1 knockdown we found on immunostaining analysis that mitochondria were more fragmented and exhibited a “beads-on-a-string” like-phenotype with less tubular network. This statement was supported with smaller mitochondria in length which were observed on the EM analysis in Armcx1 depleted cells. Although, we were able to distinguish an objective difference in the mitochondrial phenotype (small punctate/”beads-on-a-string”) when Armcx1 is absent in RPE cells, MiNa analysis was unable to show differences in the mitochondrial components between control and knockdown cells. Notably, MiNa toolset has limitations which may apply in our analysis to some extent, such as, structures that are small and in very close proximity might be merged into a bigger structure (Valente et al., 2017). Indeed, in Armcx1 knockdown cells, single mitochondria are located close to each other, based on the immunostaining analysis. Importantly, fragmented mitochondria have been widely associated with fluctuations in mitochondrial membrane potential and ROS production, processes that leads to mitochondrial fission and subsequent mitophagy (Lee and Yoon, 2014, Breckwoldt et al., 2014, Cho et al., 2017).

Furthermore, Armcx1 knockdown led to increased mitochondrial movement, whereas overexpression resulted in decreased mitochondrial movements in cultured RPE cells. Previously, Armcx3 was found to interact with the Miro/Trak2 complex and to regulate mitochondrial trafficking in neurones

(López-Doménech et al., 2012), therefore, Armcx1 could also be involved in mitochondrial dynamics in RPE.

As a result of Armcx2 knockdown in RPE cells, mitochondria appeared big, round, and isolated and with no longer elongated and tubular phenotype. In accordance, MiNa analysis showed a significant increase in the number of individual mitochondria and a decrease in their length, which supports the single and isolated mitochondrial phenotype observed on the immunostaining analysis. This was also supported by decreased mitochondrial length in Armcx2 depleted cells on EM analysis. In respect of mitochondrial mobility, the absence of Armcx2 resulted in less mobile mitochondrial when compared to the control cells. However, when overexpressed Armcx2 also led to a decrease in mitochondrial movements. Comparably to what we observe for Armcx2 in RPE cells, Armcx3 overexpression and downregulation showed reduced mitochondrial mobility in neurones and as discussed above, Armcx3 interacts with the Miro/Trak2 complex (López-Doménech et al., 2012). The loss of function of Miro/Trak2 complex was previously associated with decreased mitochondrial movements (Saotome et al., 2008, Brickley and Stephenson, 2011). This confirms Armcx3 as an important assisting protein in the mitochondrial tethering complex and thus mitochondrial transport. Thus, Armcx2 may also be involved, similarly to Armcx3 in neurones, in a complex structure that support mitochondrial transport in RPE. In respect to overexpression findings, this indicates further the involvement of Armcx2 in mitochondrial mobility, presumably having a dominant negative effect on recruitment and/or regulation of other proteins. Another possible explanation

may involve the aggregation of mitochondria upon overexpressing Armcx2 resulting in less mobile mitochondria. Moreover, Armcx2 was found to interact with vimentin (Goehler et al., 2004), an important cytoskeleton component that reduces mitochondrial motility (Sripathi et al., 2016).

Moreover, Ca^{2+} concentration in mitochondria has been shown to be very important in the formation of the mitochondrial tethering complex. Studies in neurons show that low Ca^{2+} tend to increase mitochondrial mobility, whereas increased Ca^{2+} levels in mitochondrial matrix result in the arrest of mitochondrial transport (Chang et al., 2011, Zheng et al., 2019). Notably, Lopez-Domenech et al revealed that the interaction of Armcx3 with Mito/Trak2 requires low Ca^{2+} concentration and the elevated Ca^{2+} resulted in reduced interaction (López-Doménech et al., 2012).

Importantly, the large and round mitochondrial phenotype in Armcx2 knockdown cells, was associated with swollen mitochondria following a treatment with an oxidative stress inducer that allows permeability transition pore opening and Ca^{2+} induced mitochondrial swelling (Leonard et al., 2015). The link between swollen mitochondria and increased Ca^{2+} levels would also agree with the decreased mitochondrial motility which is a result of elevated Ca^{2+} concentration as discussed above. Therefore, establishing major differences between Armcx1 and Armcx2 in mitochondrial network in RPE, we can assume that both proteins act via a different mechanism(s) and/or through Ca^{2+} concentration and/or via contacts with other assistant proteins with separate functions. In addition, here, in this project we looked into potential rescuing effect of the ancestral Armc10 from marsupial, the closest

mammalian clade lacking Armcx. Although, we are unable to make firm conclusions, it appears that Armcx1 and Armcx2 differ in respect to retaining Armc10 function. Armcx2 seems to have preserved Armc10 function through evolution, in contrast Armcx1 appears to have lost its ancestral function and/or gained a new one.

Furthermore, the accumulation of mitochondrial Ca^{2+} and expected swelling as well as ROS production are found to act synergistically in the induction of cell death (Lemasters et al., 2009). Mitochondrial fragmentation is generally accepted as a stress response following which mitochondrial fission and/or mitophagy had occurred (Miyazono et al., 2018). Thus, this led us to next investigate whether Armcx1 and Armcx2 are involved in mitochondrial degradation in RPE cells.

Chapter 6 Results: Mitophagy regulation by ARMCX in RPE

As discussed in more detail in chapter 1, mitophagy is a selective autophagic mechanism of eliminating aged and/or damaged mitochondria via specific selection and engulfment of mitochondria for subsequent lysosomal degradation (Hyttinen et al., 2018, Ma et al., 2020). Any failure to maintain functional mitochondrial turnover results in accumulation of dysfunction mitochondria which is linked to accelerated aging and aging-related diseases including AMD (Sridevi Gurubaran et al., 2020). Upon severe damage in mammalian cells, mitophagy is mediated via the PINK1-Parkin pathway, the most studied mitophagy related mechanism so far (Ma et al., 2020). There are toxic chemicals such as CCCP that are commonly used to trigger mitophagy. They are able to cross the inner mitochondrial membrane (IMM) and increase the proton permeability leading to disruption of the electron transport chain and thus impairment of oxidative phosphorylation. As a result, mitochondrial removal is prompted (Park et al., 2018). Nevertheless, proton ionophores are widely used, they embrace several limitations such as affecting the protonophoric activity of other membranous organelles – plasma membrane, lysosomes resulting into general cellular stress and eventually to cell death (Palikaras et al., 2018).

In addition, antibiotics are also used to induce mitophagy. Antimycin A and oligomycin act via different mechanisms and are generally used in a combination to enhance mitochondrial damage. The former antibiotic blocks

parts of the respiratory chain complex promoting excessive generation of mitochondrial ROS. However, it is shown that antimycin A stabilises the mitochondrial membrane potential by activating the ATP synthase. Here, the usage of oligomycin becomes valuable as it selectively blocks the ATP synthase enzyme resulting in mitochondrial depolarisation and subsequent mitophagy initiation (Georgakopoulos et al., 2017, Palikaras et al., 2018, Killackey et al., 2020). Indeed, CCCP has been widely used to trigger Parkin-dependent mitochondrial degradation. Briefly, the process involves PINK1 stabilisation on the outer-mitochondrial membrane, which is degraded under normal conditions, and subsequently recruits Parkin form the cytosol to mitochondria. Located at mitochondria, Parkin then ubiquitinates several substrates which in turn initiates degradation of mitochondrial outer proteins and mitophagy (Ham et al., 2020).

Furthermore, CCCP treatment was previously shown to be successful in inducing mitophagic flux in ARPE-19 cells (Devi et al., 2019). We therefore used CCCP-induced mitochondrial depolarisation as a mitophagy inducer in this project.

Since, mitochondrial fragmentation and fission are described as a prerequisite for mitophagy (Pi et al., 2013, Li et al., 2018) next we wanted to determine whether Armcx1 and Armcx2 play a role in mitophagy in ARPE-19 cells.

6.1 ARMCX1 and ARMCX2 localisation during mitophagy in RPE

6.1.1 ARMCX1 co-localises with mitochondria in non-differentiated and differentiated ARPE-19 during CCCP treatment

We first assessed the effect of mitochondrial degradation-inducing agent CCCP on the mitochondrial morphology in non-differentiated and differentiated ARPE-19. Simultaneously, we also investigated the endogenous Armcx1 sub-cellular co-localisation upon CCCP treatment in non-differentiated and differentiated ARPE-19. The outer mitochondrial membrane marker Tom20 was used to label mitochondria. Treatment of non-differentiated and differentiated ARPE-19 with CCCP resulted in increased mitochondrial fragmentation (Figure 6.1 A, B). Moreover, less mitochondrial staining was observed in non-differentiated and to a lesser extent in differentiated cells upon CCCP treatment. However, differentiated cells revealed stronger mitochondrial fragmentation following CCCP, than non-differentiated cell. Mitochondria in non-differentiated cells retained some of the perinuclear mitochondria, whereas in differentiated RPE cells, mitochondrial networks appeared completely destructed (Figure 6.1 A, B).

In addition, we also investigated endogenous Armcx1 in response to CCCP treatment. Armcx1 remained associated with the mitochondrial outer membrane marker Tom20 in both non-differentiated and differentiated ARPE-19 and mimicked Tom20 staining following CCCP treatment (Figure 6.1A, C).

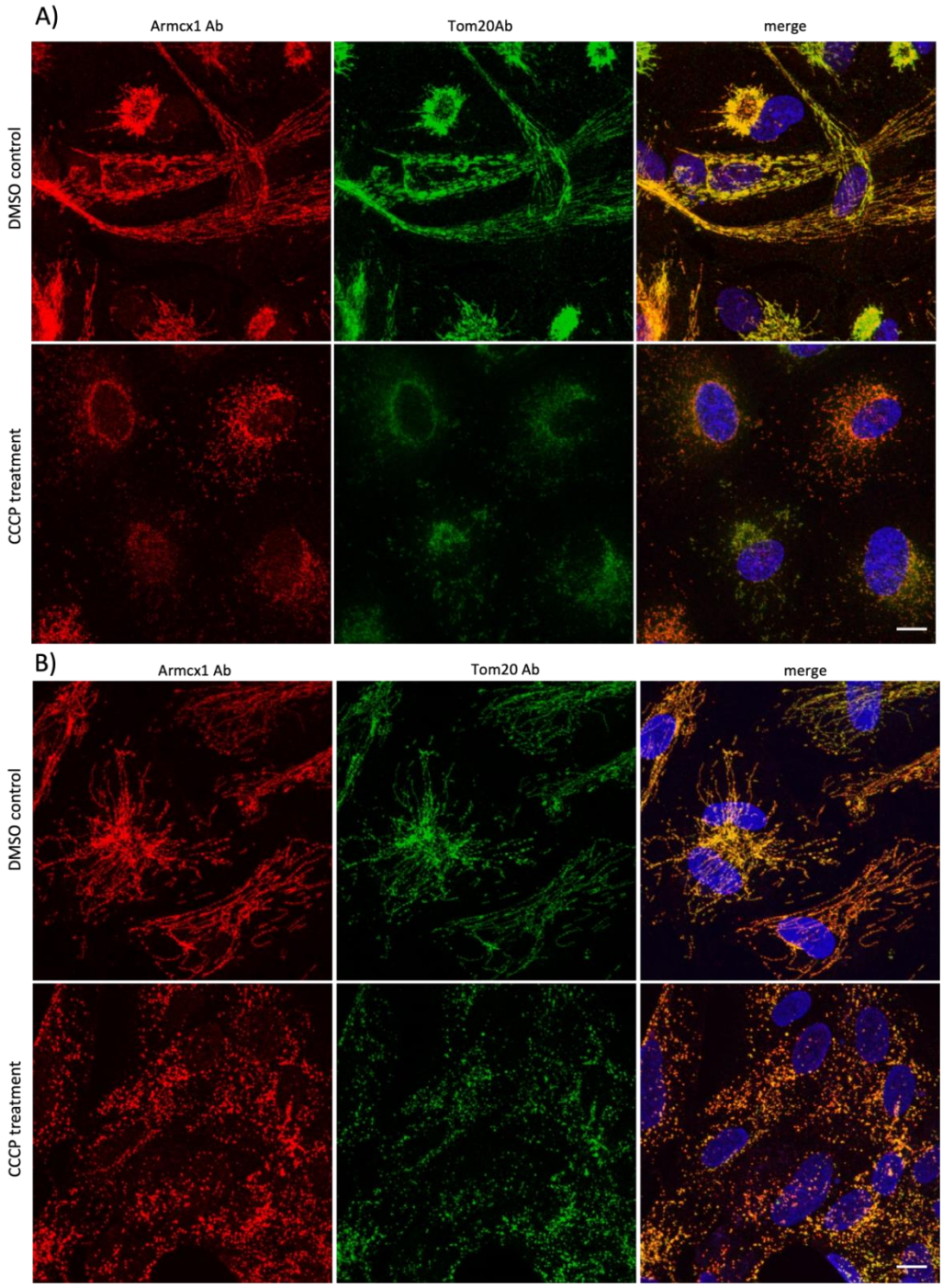

Figure 6.1 Armcx1 remained associated with Tom20 even after inducing mitochondrial degradation in non-differentiated and differentiated ARPE-19. AREP-19 cells were treated with 20 μM CCCP or DMSO (control) for 24h prior to methanol fixation and dual immunostaining with Armcx1 (secondary Alexa Fluor 488) and Tom20 (secondary Alexa Fluor 555) antibodies. Images were taken by a ZEISS LSM700 confocal microscopy 63x oil objective; merge images include Hoechst staining indicating the nucleus. A) Non-differentiated cells B) Cells differentiated for >20 weeks. Scale bar = 10 μm.

6.1.2 ARMCX2 co-localises partially with mitochondria in non-differentiated ARPE-19 during CCCP treatment

Armcx2 remains associated with the mitochondrial marker Tom20 in non-differentiated after treatment with CCCP (Figure 6.2). Reduced mitochondrial staining based on the Tom20 signal was observed following CCCP treatment. However, Arcmx2 staining appeared relatively unchanged. Notably, these observations are based on epifluorescence microscopy and need to be verified on a confocal microscopy. Unfortunately, we were unable to test Armcx2 expression in CCCP-treated differentiated ARPE-19 due to the fact that Armcx2 antibody validation was achieved at a later stage than Armcx1 and then a further obstacle was the subsequent loss of cells that had been differentiated for >20 weeks during the Covid-19 pandemic.

Overall, these results indicate that Armcx1 and Armcx2 are attached to fragmented mitochondria during CCCP treatment.

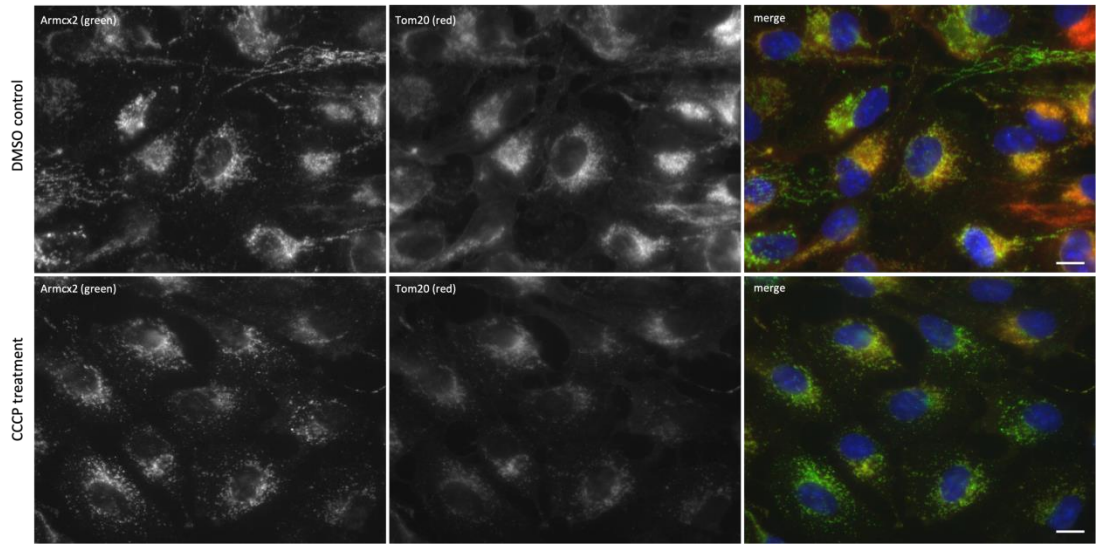

Figure 6.2 Armcx2 remained associated with Tom20 even after inducing mitochondrial degradation in non-differentiated ARPE-19. Non-differentiated ARPE-19 cells were treated with 20 μM CCCP or DMSO (control) for 24h prior methanol fixation and dual immunostaining with Armcx2 (secondary Alexa Fluor 488) and Tom20 (secondary Alexa Fluor 555) antibodies. Images were taken by a Zeiss Axioskop 2 63x oil objective; merge images include Hoechst staining indicating the nucleus; scale bar = 10 μm

6.2 ARMCX1 and ARMCX2 effects on Parkin activity upon mitophagy induction

6.2.1 CCCP treatment induces recruitment of Parkin to mitochondria in RPE cells

Next, we wanted to analyse mitophagy more directly in ARPE-19 cells by tracking exogenously expressed Parkin. First, we assessed mitophagy by expressing mCherry-Parkin and detecting its activation (its recruitment to mitochondria) upon CCCP treatment in ARPE-19 cells. We tested two different time points 3 and 6 h of CCCP treatment with the aim to establish moderate mitochondrial degradation, so that both weakening and exacerbation could be distinguished following manipulation of Armcx1 and Armcx2. In control cells,

Parkin signal was diffuse and distributed across the entire cytoplasm. Upon mitochondrial depolarization with CCCP treatment, Parkin translocated to the mitochondrial membrane as identified by co-localisation with the mitochondrial marker Tom20. High resolution images using a confocal microscope are required for better analysis of the results.

Parkin puncta represent mitochondria tagged for removal. Thus, their quantification can be used as a direct measure for mitophagy (Thai et al., 2019). There was a significant increase of Parkin puncta formation following 3 and 6 h of CCCP treatment as expected (Figure 6.3). We decided to work with a 3 h CCCP incubation for further experiments due to the clear Parkin activation and moderate mitochondrial degradation.

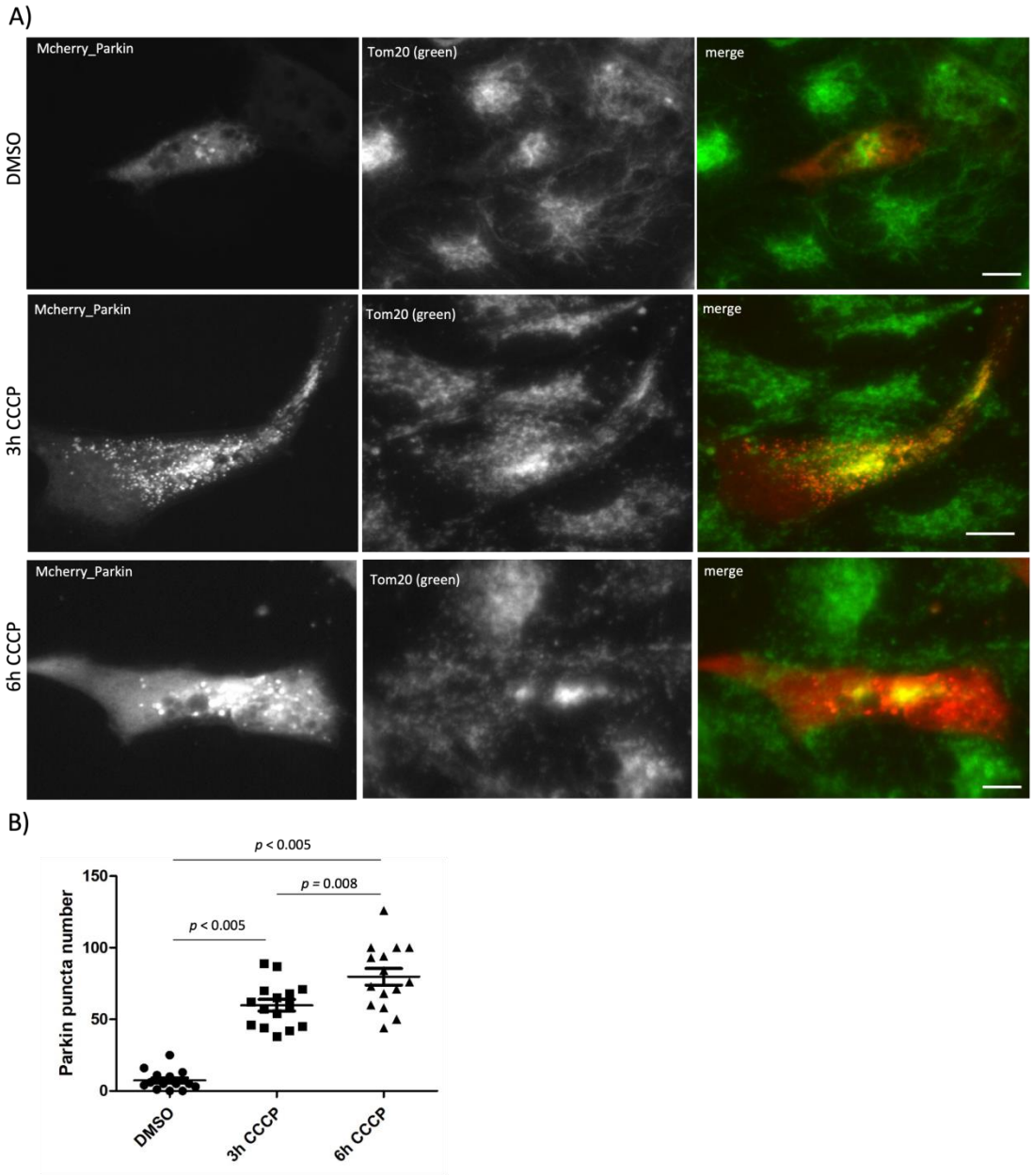

Figure 6.3 MCherry-Parkin activation following CCCP treatment in ARPE-19 cells. **A)** ARPE-19 cells were transfected with 1 µg of mChery-Parkin 24 h prior treatment with DMSO or 20 µM CCCP for 3 or 6 h. Following the treatment, cells were fixed in methanol and subsequently indirect immunostaining was carried out with Tom20 (secondary Alexa Fluor 488) antibody; images were taken by a Zeiss Axioskop 2 63x oil objective; merge images do not include nuclear staining; Scale bar = 10 µm. **B)** mChery-Parkin puncta were quantified from 15 cells in 1 experiment; p values are presented on the plot.

6.2.2 The effect of ARMCX1 or ARMCX2 knockdown on Parkin activation in CCCP-treated cells

In order to investigate whether Armcx1/2 are involved in Parkin-dependent CCCP-induced mitophagy, parkin puncta formation was quantified in Armcx1/Armcx2 knockdown cells.

Similarly, to the above experiment, we investigated mitophagy by expressing mCherry-Parkin and observing its translocation from cytoplasm to mitochondria following 3 h of CCCP treatment in cells lacking Armcx1/Armcx2. Quantification of mCherry-Parkin translocation and thus parkin activation was performed by counting manually the parkin puncta and the overall number from each cell was plotted on a scatter dot plot (Figure 6.4 B, Figure 6.5 B).

Armcx1 knockdown on its own did not induce Parkin activation in the control (DMSO) treatment based on the lack of Parkin puncta and their co-localisation with mitochondria, the latter being identified with the Tom20 marker (Figure 6.4). However, once mitophagy was induced by CCCP treatment, we established an increase Parkin activation in Armcx1 knockdown cells. In addition, we observed a strong aggregated mitochondrial phenotype in some cells, as determined by Tom20 staining (Figure 6.4 A yellow arrow). Comparably, Armcx2 knockdown did not induce mitochondrial removal in the control DMSO treated cells (Figure 6.5 A). Moreover, even following mitochondrial depolarization with CCCP, Parkin puncta numbers were not increased in cells lacking Armcx2 (Figure 6.5 B).

Overall, lack of Armcx1 enhanced drug induced but not baseline mitophagy. In contrast, Armcx2 knockdown did not significantly increase Parkin activation, indicating different functions for Armcx1 and Armcx2 in Parkin-dependent mitophagy.

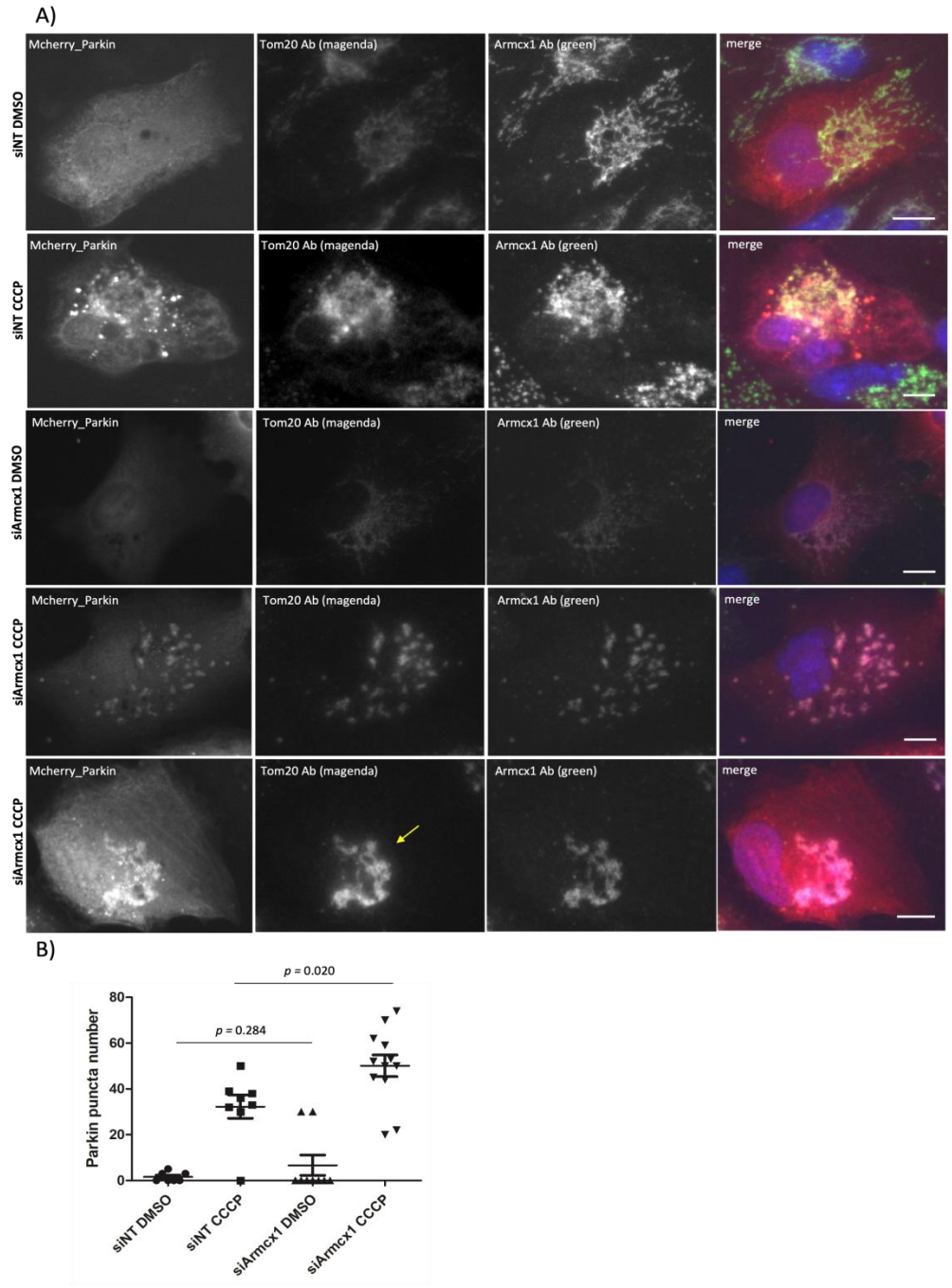

Figure 6.4 Armcx1 knockdown effect on Parkin activation upon CCCP treatment in ARPE-19 cells. **A)** cells were transfected with a pool of non-targeting siRNA (siNT) or siRNA targeting Armcx1 (siArmcx1) 72h prior to transfection with 1 µg of mChery-Parkin. 24 h later cells were treated with 20 µM CCCP or DMSO (control) for 3 h, fixed in methanol and immunostained with Armcx1 (secondary Alexa Fluor 488) and Tom20 (secondary Alexa Fluor 647) antibodies. Images were taken with a Zeiss Axioskop 2 63x oil objective; merge images include Hoechst staining indicating the nucleus; Scale bar = 10 µm. **B)** mChery-Parkin puncta were quantified from 8-12 cells in 1 experiment; p values are presented on the plot.

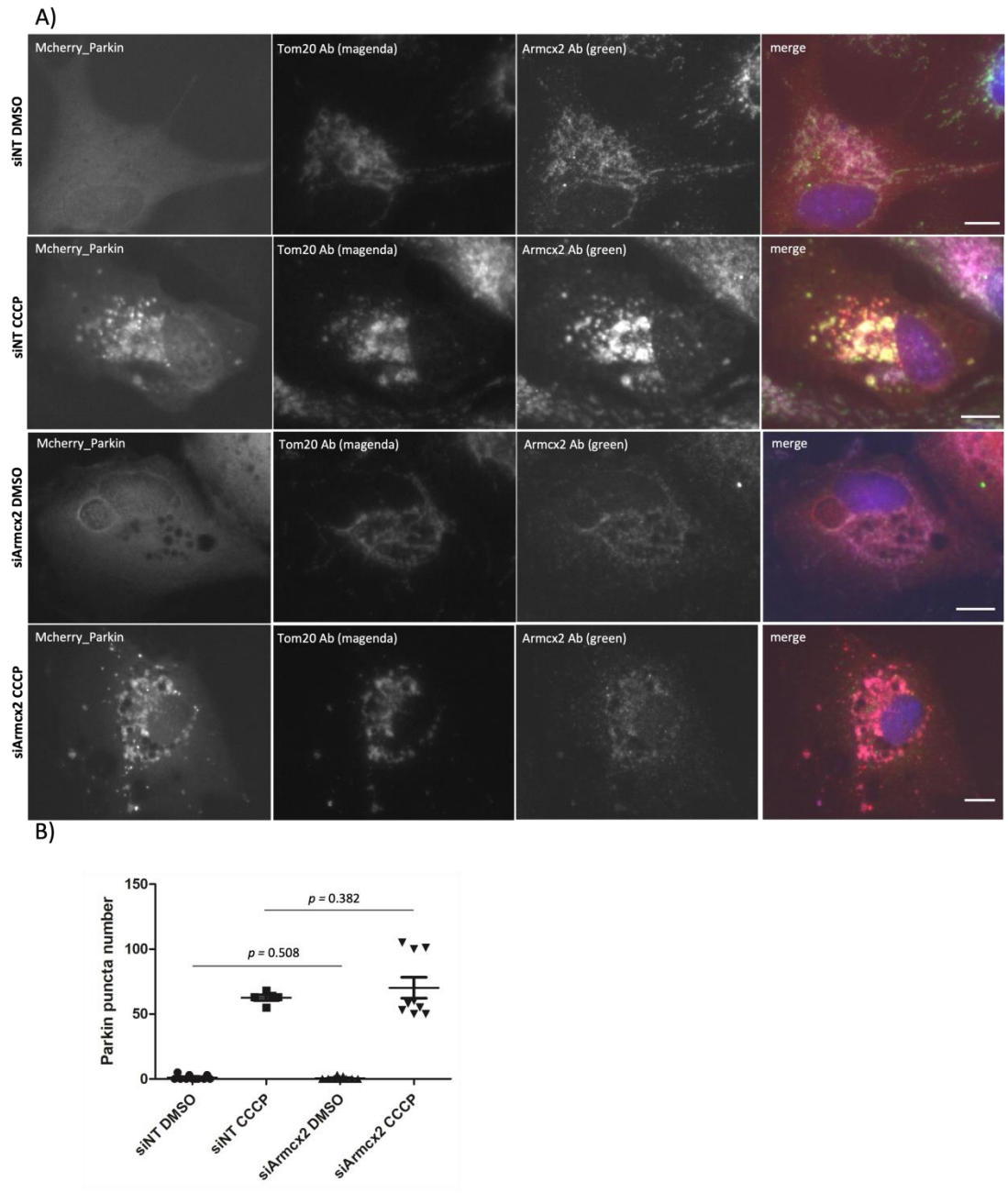

Figure 6.5 Armcx2 knockdown effect on Parkin activation upon CCCP treatment. **A) cells** were transfected with non-targeting siRNA (siNT) or siRNA targeting Armcx2 (siArmcx2) 72h prior to transfection with 1 µg of mChery-Parkin. 24 h later cells were treated with 20 µM CCCP or DMSO (control) for 3 h, fixed in methanol and immunostained with Armcx2 (secondary Alexa Fluor 488) and Tom20 (secondary Alexa Fluor 647) antibodies. Images were taken with a Zeiss Axioskop 2 63x oil objective; merge images include Hoechst staining indicating the nucleus; Scale bar = 10 µm. **B)** mChery-Parkin puncta were quantified from 5-14 cells in 1 experiment; p values are presented on the plot.

6.2.3 The effect of exogenous expression of ARMCX1, 2 or marsupial Armc10 on Parkin activation in CCCP-treated cells

To further assess the role of Armcx1/Armcx2 in Parkin activation upon CCCP-induced mitochondrial degradation, plasmid constructs carrying Armcx1/Armcx2 or marsupial Armc10 were co-transfected with mCherry-Parkin. We also included marsupial Armc10 in this experiment to further observe whether Armcx1 and Armcx2 have retained the function in Parkin activation from their ancestor.

The ectopic expression of Armcx1 and Armcx2, as well as marsupial Armc10 did not induce Parkin activation in control (DMSO) treated cells (Figure 6.6 A, B). Following CCCP treatment, Parkin activation was increased in non-transfected, Armcx1 and Armcx2-overexpressed cells compared to the control (DMSO) cells. Moreover, overexpression of all Armcx tested led to a decrease in CCCP-induced Parkin activation, with Armcx1 reducing only weakly and Armcx2 more strongly. In contrast, Armc10 expression blocked it altogether. Armcx1 overexpression resulted in a different number of Parkin puncta formation with some cells exhibiting more condensed Parkin signal. However, there were cells with overexpressed Armcx2 that lacked Parkin activation upon CCCP treatment.

Overall, Armcx1 knockdown increased Parkin activation, whereas Armcx1 overexpression reduced it, clearly indicating a role of Armcx1 in Parkin dependent mitophagy in RPE cells. Although, Armcx2 knockdown did not

change the number of Parkin puncta formation, Armcx2 ectopic expression decreased Parkin activation in RPE cells, also suggesting an important role in this process. Furthermore, marsupial Armc10 appeared to halt completely Parkin activation upon CCCP treatment, suggesting that Armcx1 and Armcx2 may have lost some ancestral function and/or instead gained new functions.

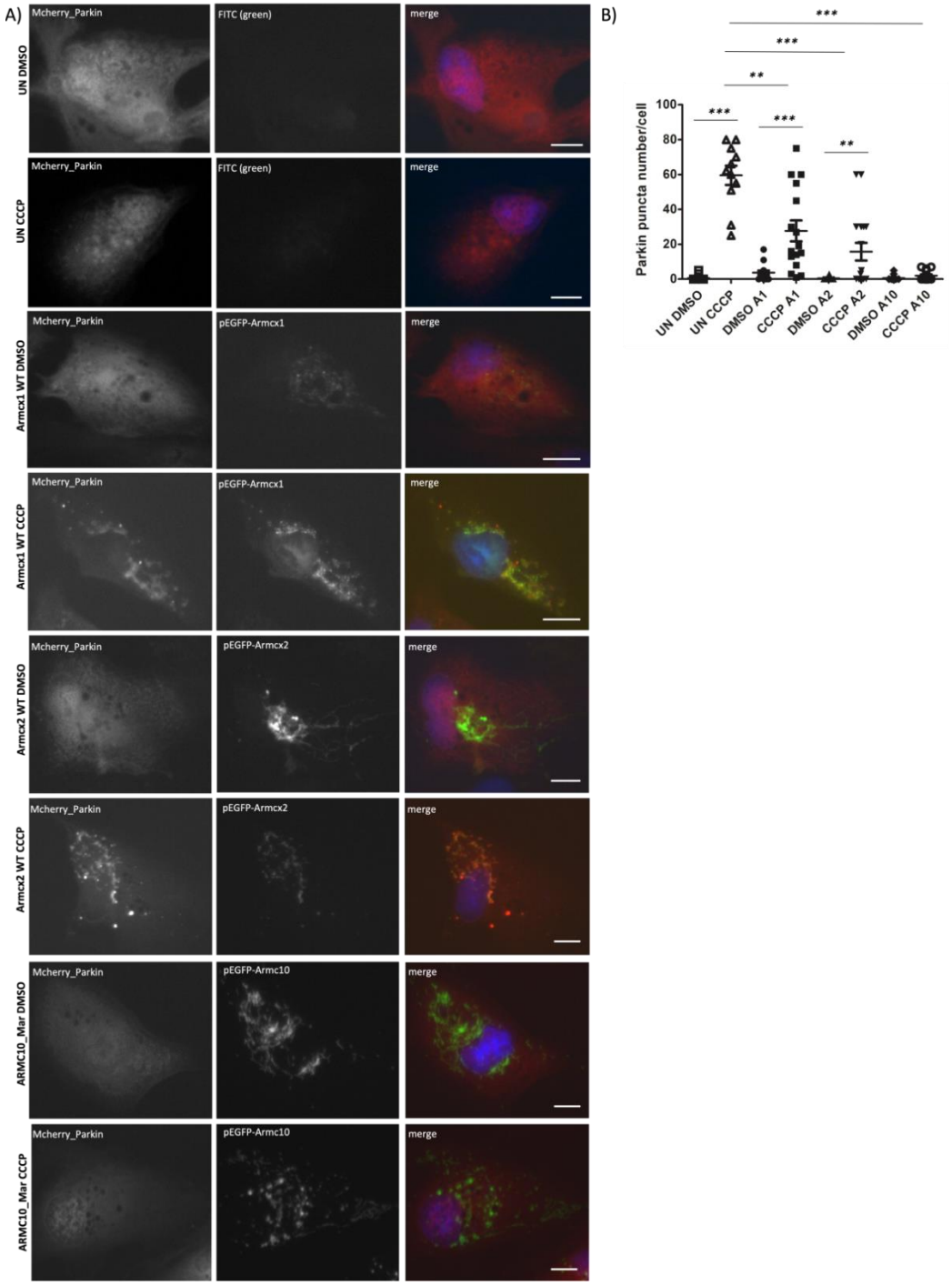

Figure 6.6 The effect of exogenous Armcx and marsupial Armc10 expression over Parkin activation in CCCP treatment. **A)** ARPE-19 cells were co-transfected with 0.1 µg of mChery-Parkin and 0.9 µg of Armcx/Armc10 24 h prior CCCP or DMSO (control) treatment for 3 h. Cells were subsequently fixed in methanol and imaged with a Zeiss Axioskop 2 63x oil objective; merge images include Hoechst staining indicating the nucleus; Scale bar = 10 µm. B) mChery-Parkin puncta were quantified from 11-15 cells in 1 experiment; p values are presented as *p<0.05, **p<0.01, ***p<0.001.

6.3 ARMCX1 and ARMCX2 affect differently endogenous LAMP2, an important regulator of autophagy

Having investigated whether Armcx1/Armcx2 are involved in the Parkin activation process, we also wondered whether they play a role in later stages of mitochondrial degradation, such as the final lysosomal digestion stage. We investigated the regulation of the lysosomal membrane-associated protein 2 (Lamp2), an important component of the lysosomal membranes and regulator of autophagy (Cui et al., 2020) following Armcx1 and Armcx2 knockdown and overexpression.

Interestingly, when we knocked down Armcx1, endogenous Lamp2 protein levels were significantly increased based on Western blot analysis (Figure 6.7 A). Subsequently, we looked into whether Armcx2 and marsupial Armc10 could rescue effects of Armcx1 depletion on Lamp2 expression. Exogenous Armcx2 was able to return Lamp2 to its basal levels in the Armcx1 knockdown cells, but Lamp2 levels remained increased following expression of marsupial Armc10 (Figure 6.7 B).

In contrast, endogenous Lamp2 was significantly downregulated in Armcx2 knockdown by Western blot analysis. Exogenous Armcx1 expression was unable to rescue Lamp2 phenotype and instead Lamp2 remained significantly reduced when compared to the control lane (Figure 6.7 C). Notably, marsupial Armc10 expression efficiently restored Lamp2 levels in Armcx2-silenced cells (Figure 6.7 C). Moreover, we also investigated Lamp2 levels upon Armcx1, Armcx2 and marsupial Armc10 exogenous expression. Endogenous Lamp2

expression was significantly reduced when exogenous Armcx1, Armcx2 and Armc10 were present (Figure 6.7 D).

Overall, we revealed another function of Armcx1 and Armcx2 where they appear to show diversity. Overexpression of either protein resulted in an apparent reduction in Lamp2 protein. However, whereas Lamp2 was increased in Armcx1-depleted cells, loss of Armcx2 reduced Lamp2, suggesting different functions in the regulation of Lamp2 expression, an important factor in the degradative capacity of the lysosome and therefore degradation of damaged cellular organelles.

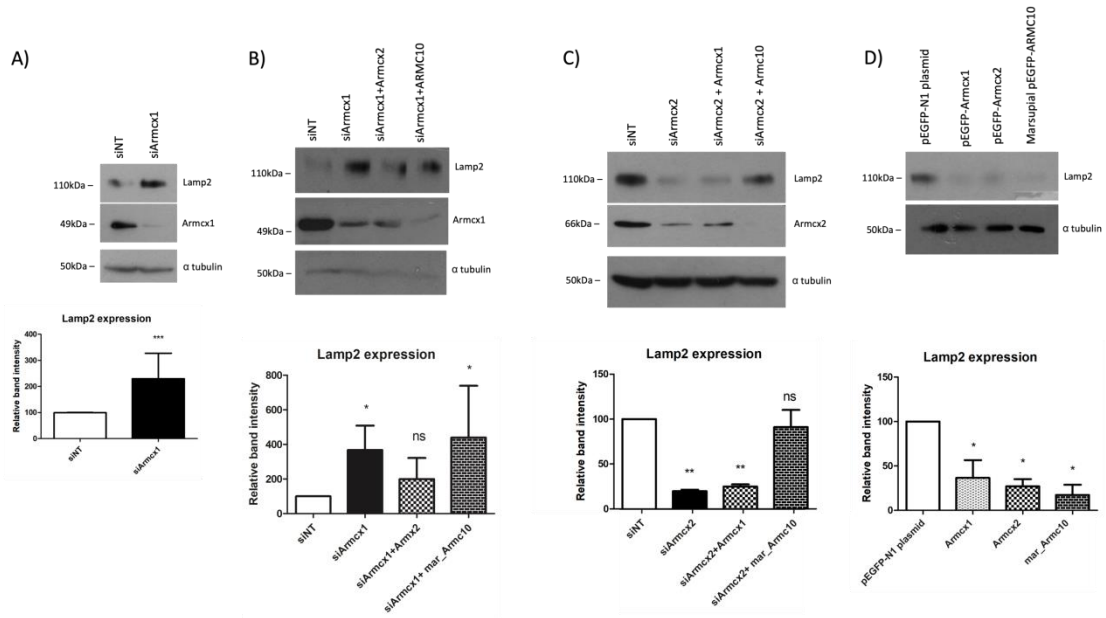

Figure 6.7 Endogenous Lamp2 expression affected differently by Armcx1 and Armcx2. Sub-confluent ARPE-19 cells were transfected with a pool of non-targeting siRNA (siNT) or siRNA targeting Armcx1 (A and B) or Amrcx2 (C). 72 h post-transfection cells were transfected with 1 µg of Armcx1/Armcx2 or Armc10-GFP plasmids (B and C) and on the following day cell lysates were prepared and analysed by Western blot. D) ARPE-19 cells were transfected with 1 µg of empty GFP plasmid/Armcx1/Armcx2 or Armc10-GFP plasmids and 24 h later cell lysates were prepared and analysed by Western blot. Densitometry quantifications of 2 independent experiments are shown below each blot, with statistical significance established by unpaired t-test (***p<0.001; **p<0.01; *p<0.05; ns – non-significant).

6.4 Discussion

Armcx1 strongly co-localised with mitochondria in both non-differentiated and differentiated ARPE-19 upon the induction of mitochondrial degradation using CCCP treatment. CCCP treatment is reported to reduce the number of mitochondria (Wang and Klionsky, 2011, Zilocchi et al., 2018). As expected, mitochondrial staining with Tom20 was decreased in non-differentiated ARPE-19 cells following treatment with CCCP. However, this should be supported with protein levels of mitochondrial markers on Western blot analysis. In contrast, mitochondrial staining was not reduced in differentiated ARPE-19

cells following CCCP treatment suggesting that differentiated cells might take longer to fully eliminate damaged mitochondria than non-differentiated cells, which would cause accumulation of dysfunctional mitochondria. In addition, mitochondrial fragmentation appeared more severe in differentiated ARPE-19. As seen in other post-mitotic cell types, this could be due to differentiated cells being more susceptible to mitochondrial damage having higher energy demands (Doxaki and Palikaras, 2020).

As postmitotic cells, differentiated RPE cells are well known to accumulate waste materials such as lipids and oxidized proteins as a result of their prolonged life span and higher energy demand. In contrast, frequently proliferating non-differentiated cells with short life span do not accumulate large amounts of waste products, likely due in part to dilution during cell division, and therefore can easily degrade damaged cellular products (Terman et al., 2010). Therefore, RPE cells need mechanisms in place to efficiently process damaged particles, which would otherwise delay and/or prevent the process of degradation and removal (Brown et al., 2019). With age, some material seems to escape clearance mechanisms and aged RPE cells were found to be more susceptible to oxidate stress, with reduced mitophagy and accumulation of damaged mitochondrial DNA (Diot et al., 2016, Gouras et al., 2016).

Although better quality imaging is required to make conclusions, while the mitochondrial Tom20 marker was reduced upon mitophagy induction, no decrease in Armcx2 staining was observed. Armcx2 was identified as an outer mitochondrial membrane protein in a wide proximity proteomic study in HeLa

cells (Heo et al., 2019). Moreover, immunogold-EM images of Armcx3 overexpressed in HEK293 cells, suggest that its localisation is restricted to the outer mitochondrial membrane and specifically to areas in close contact to other organelles (López-Doménech et al., 2012). This is in line with emerging evidence that shows a multi-organelle relationship between mitochondria, lysosomes and ER that governs mitochondrial dynamics (Friedman et al., 2011, Wong et al., 2018, Sugiura et al., 2014).

Our data suggests that Armcx1 and Armcx2 expression can affect Parkin-dependent mitophagy following mitochondrial depolarisation in RPE cells. We uncovered a role for Armcx proteins in the regulation of Parkin activation and recruitment to puncta at mitochondria. Armcx1 depletion/overexpression increased/reduced Parkin puncta respectively in mitophagy-induced cells, indicating a regulatory role for Armcx1 in Parkin-mediated mitochondrial degradation. Ectopic expression of Armcx2 similarly reduced or even abolished Parkin activation in some cells. This could, however, be due to loss of mitochondria in these cells resulting from a combination of the severe mitochondrial aggregation phenotype observed with Armcx2 overexpression, in addition to effects of CCCP treatment. Further experiments including Tom20 staining are needed in order to draw any conclusions. In contrast to Armcx1 however, when Armcx2 was silenced Parkin puncta number did not change upon CCCP treatment, suggesting that although overexpressed protein can, to some extent, arrest Parkin activation upon CCCP treatment, endogenous Armcx2 may not play an regulatory role in mitophagy, but further experiments and higher cell numbers are needed to make a firm conclusion. Importantly,

the ectopic expression of marsupial Armc10 completely blocked Parkin activation following mitophagy induction, suggesting an important function for Armc10 in Parkin translocation from the cytoplasm to mitochondria. The first indication that Armcx/Armc10 might be involved in the process of Parkin-dependent mitochondrial degradation came from a large proteomic study in HeLa cells that identified human Armc10, Armcx2 and Armcx3 as Parkin substrates (Heo et al., 2019). Here, our data provides further evidence that Armcx members and their ancestor Armc10 from marsupial species are involved with the Parkin-dependent mitophagy mechanism. However, the exact mechanism(s) through which Armcx/Armc10 might regulate Parkin-dependent mitophagy is still at its very early stage of understanding.

In this chapter functional diversities between Armcx1 and Armcx2 continue to emerge, also in respect to whether they are a result of divergent evolution towards additional functions of their ancestral Armc10 or they have been divided into distinct descendant proteins. We have uncovered a novel role for Armcx proteins in the late lysosomal degradation pathways. As mentioned above, Armcx2, Armcx3 and Armc10 have recently been linked to Parkin-dependent mitophagy (Heo et al., 2019). Depletion of Armcx1 enhanced the expression of Lamp2, whereas Armcx2 knockdown suppressed the lysosomal membrane protein in ARPE-19 cells. The overexpression of Armcx1 resulted in a decrease Lamp2 expression, suggesting Armcx1 as an important regulator of this lysosome-associated protein. Importantly, exogenous expression of Armcx2 in Armcx1 depleted cells, rescued Lamp2 upregulation, suggesting that Armcx2 share similar function with Armcx1 over the regulation

of Lamp2. However, whereas Armcx1 depletion increased both Parkin puncta and Lamp2 protein, this was not the case when Armcx2 was depleted. Indeed, Lamp2 was reduced in cells lacking Armcx2, suggesting that if anything, endogenous Armcx2 may have an opposing effect from Armcx1. Consistent with divergent functions, ectopic Armcx1 was unable to rescue Lamp2 decrease, indicating that Armcx1 have either lost a function that Armcx2 possesses or Armcx2 have acquired a new one. Moreover, since no effect was observed on Parkin puncta formation in Armcx2-depleted cells, it is possible that Armcx2 is involved in a Parkin-independent mechanism of Lamp2 regulation, possibly by acting as a dominant negative and/or deregulating other interacting molecules. Similarly, marsupial Arcm10 expression produced comparable response to Armcx2 overexpression, consistent with a similar function for Armcx2 to that of its ancestor. Lamp2 plays important roles in lysosomal function and autophagy and interestingly, Lamp2 deficiency was found to accelerate RPE dysfunction and the accumulation of extracellular deposits that are a hallmark of AMD (Notomi et al., 2019).

Functionally, this data supports the evolutionary analysis indicating that Armcx are paralogues that occurred after a duplication event of their ancestral gene Arcm10, exhibiting different sequence compositions and functions.

Chapter 7 General Discussion and Future Perspectives

7.1 Molecular functions of ARMCX1 and ARMCX2

Among Armcx family members, Armcx3 is the most widely studied one. Armcx3 has been found to localise to the outer mitochondrial membrane in mouse neurons and to interact with and mediate the transport of Sox10 transcription factor from the nucleus to the mitochondria (Mou et al., 2009). Armcx3 also causes mitochondrial aggregation and affects mitochondrial dynamics and trafficking via interaction with the Kinesin/Miro/Trak2 complex in hippocampal neurons (López-Doménech et al., 2012). These findings are in line with observations that Armadillo domains are involved in regulating vesicular traffic between the ER and Golgi apparatus (An et al., 2009), strongly suggesting that Armcx family are involved in sub-cellular organelle trafficking mechanisms.

In our study we showed strong association of both exogenously expressed and endogenous Armcx1 and Armcx2 with mitochondria in ARPE-19 cells. As has previously been shown for Armcx3, we also observed a mitochondrial aggregation in response to Armcx2 overexpression. Moreover, both Armcx1 and Armcx2 knockdown resulted in fragmented mitochondria and affected mitochondrial mobility in ARPE-19 cells. Since Armcx3 interacts with Miro/Trak2 proteins, which, in complex with kinesin mediate mitochondrial traffic, Armcx1 and Armcx2 may also be involved in modulating mitochondrial

dynamics in ARPE-19 cells through interaction with the Miro-1/Trak2 complex. However, Armcx3-mediated mitochondrial aggregation was independent of Miro1, but a similar mitochondrial aggregation phenotype has been observed following overexpression of Mitofusin-1 (Mfn1), an important mediator of mitochondrial fusion (Santel and Fuller, 2001), suggesting that Armcx proteins may act through Mfn1 to mediated mitochondrial aggregation. It would be interesting to evaluate both of these potential interactions via co-immunoprecipitation analysis. Continuous coordinated fusion and fission events form a highly dynamic mitochondrial network that is important for maintaining mitochondrial abundance, quality and function. Effects on the mitochondrial fission machinery could also explain the influence of Armcx1 and Armcx2 on the mitochondrial network. Dynamin-related protein (Drp-1) is a major regulator of mitochondrial fission (Tian et al., 2018). It has been shown that Cyclin C interacts with and increases the activity of Drp-1, thus resulting in mitochondrial hyperfission network (Ganesan et al., 2019). Furthermore, phosphorylation of Drp-1 by AMPK results in mitochondrial fragmentation via Drp-1 recruitment (Toyama et al., 2016). Importantly, Armc10 was shown to be phosphorylated by AMPK and involved in regulating mitochondrial dynamics in HEK293 cells (Chen et al., 2019). Therefore, it would be interesting to see whether there is a regulatory effect of Armcx1/2 on Drp-1 function. In addition, since Armcx1 and Armcx2 appear to affect mitochondrial dynamics, it will be important to evaluate whether both proteins play a role in mitochondrial respiration, mitochondrial DNA number and Ca^{2+} homeostasis, all of which can be important in mitochondrial dynamics (Santel and Fuller, 2001).

Mitochondrial fission contributes to mitochondrial degradation and is a prerequisite for ubiquitin-mediated mitophagy (Ma et al., 2020). Armcx2 and Armcx3 were identified as Parkin targets in a large proximity proteomic study, strongly suggestive of a role in mitophagy (Heo et al., 2019). In our study, knockdown of Armcx1 in ARPE-19 increased the number of fragmented mitochondria, suggesting mitophagy induction. We also observed that Armcx1 and Armcx2 affected Parkin activation following mitochondrial depolarisation. Parkin activation was increased in Armcx1 knockdown cells upon mitochondrial depolarisation, and Parkin activation was decreased when Armcx1 was overexpressed. Notably, Armcx2 overexpression also decreased Parkin activation, but Armcx2 depletion did not change the activation levels of this ubiquitin ligase. Notably, Armcx1 was upsent from the published parkin proximity data set (Heo et al., 2019). This may reflect the incomplete coverage of such proteomic approaches due to technical limitations. Alternatively, this could be due to the very narrow strategy used in their study and is highly likely that their list of interactions is not complete. Alternatively, Armcx1 may not be a target of Parkin but may instead restrict Parkin activity in a looser, more indirect way. Taken together our data strongly showed that Armcx1 was involved in Parkin activation, but a formal demonstration of direct interaction or Parkin-dependent ubiquitination of Armcx proteins is required for a more detailed mechanistic insight.

Furthermore, we showed for the first time that Armcx1 and Armcx2 played a role in a functionally connected downstream pathway, namely lysosomal degradation. Specifically, we found that Lamp2 was significantly upregulated upon Armcx1 knockdown. In sharp contrast, Armcx2 depletion led to

decreased levels of this lysosomal marker. Lamp2 deficiency leads to the development of Danon's disease, characterised clinically with cardiomyopathy and is associated with accumulation of undigested, autophagic material in the myocytes (Nishino et al., 2000, Liu et al., 2020). Under conditions of cellular/metabolic stress, including CCCP-induced mitophagy, the transcription factor EB (TFEB) translocates to the nucleus and activates transcription of the Coordinated Lysosome Expression and Regulation (CLEAR) network (Ivankovic et al., 2016). Parkin/PINK1 signalling can induce TFEB nuclear translocation and activation of the CLEAR network resulting in upregulation of lysosome and autophagy proteins (Ivankovic et al., 2016). Regulation of Parkin by Armcx proteins is therefore likely to underly effects on Lamp2 expression. As well as mitophagy, CCCP treatment can also stimulate mitochondrial repair mechanisms through the formation of mitochondrial-derived vesicles (MDVs) (McLelland et al., 2014). Damaged mitochondrial membrane can bud away from mitochondria into MDVs that go on to fuse with lysosomes for degradation. This process is also dependent on Parkin, suggesting that Armcx may be regulating multiple Parkin-dependent mitochondrial quality control mechanisms (Brown et al., 2019). Intriguingly, Lamp2 was found recently to be dispensable for PINK1/Parkin-mediated mitophagy in HeLa cells (Liu et al., 2020), suggesting that the effect of Armcx1/Armcx2 over Lamp2 is either downstream, or independent of effects on PINK1/Parkin. Therefore, it is possible that Armcx1 and Amrcx2 regulate Parkin-dependent mitophagy differently and this regulatory process could be dependent or independent of Lamp2.

However, additional experiments looking at the immunostaining levels of Lamp2 as well as immuno-EM analysis would be beneficial in supporting the regulatory function of Armcx1/2 of Lamp2. Further experiments are needed to better understand how Armcx1 and Armcx2 are involved in Parkin-dependent mitophagy. For instance, this could include looking at aggregation of PINK1 protein on the OMM. Aggregated PINK1 at the OMM recruits Parkin to the mitochondria, eliciting the PINK1/Parkin complex formation that triggers mitophagy (Parzych and Klionsky, 2014). Additionally, it would be informative to determine how Armcx1/2 expression levels affect TFEB nuclear translocation and the subsequent activation of CLEAR. The autophagosome marker LC3 should also be measured both by Western blot and immunofluorescence analysis upon Armcx1 and Armcx2 knockdown, which will further indicate the role of these proteins in mitochondrial degradation. In cells depleted of Armcx1 Parkin formed puncta at the mitochondria, suggesting enhanced mitophagy. Increased LC3 colocalisation with mitochondria by fluorescence microscopy, or lipidation by western blot, would provide further evidence of mitophagy. Lipidation of LC3, by addition of phosphatidylethanolamine (PE) is a marker of autophagy and can be detected by western blot due to the increased migration rate of lapidated LC3 on a gel (Parzych and Klionsky, 2014). In addition, it would be interesting to investigate whether Armcx1/Armcx2 cause any changes in the mitochondrial membrane potential upon CCCP treatment, as this is an important factor of driving further mitochondrial degradation.

A direct link has been described between mitochondrial dynamics and mitophagy, where upon bioenergetic stress and/or oxidative stress mediators

from the mitochondrial dynamic machinery are activated (Ma et al., 2020). However, a recent study revealed that Drp-1-mediated mitochondrial fission was important in the progression of reperfusion injury in neurones, but independent of PINK1/Parkin mitophagy flux (Anzell et al., 2021), suggesting that mitochondrial dynamics and mitophagy might not always be integrated. Therefore, from our data Armcx1 and Armcx2 appear to be involved in the regulation of mitochondrial dynamic and/or degradation, however the exact mechanism(s) still remain to be elucidated.

7.2 Oxidative and metabolic stress in RPE and potential regulation by ARMCX

Accumulating evidence indicates that mitochondrial damage in the RPE is involved in the degeneration of the macula and AMD development (Feher et al., 2006, Terluk et al., 2015). Indeed, a recent study looked at genetic variants associated in human fetal RPE in conditions linked to AMD and found hundreds of loci which are associated with mitochondria oxidation and increased lipid biogenesis (Liu et al., 2019). Since, Armcx proteins have been described as mitochondria-associated proteins (López-Doménech et al., 2012) and our lab has previously published selectively expressed genes in differentiated RPE cells among which was Armcx6 (Turowski et al., 2004), this provides a strong rational for understanding the role of the Armcx family in regulating the mitochondrial network in the RPE. Furthermore, Armcx3 was shown to be regulated by Wnt5a signalling pathway in epithelial cells (Serrat et al., 2013), a signalling cascade which is also important for RPE differentiation (Kim et al., 2015).

Currently, there is lack of understanding of the role of Armcx proteins in regulating RPE differentiation and/or function. In the present study we have confirmed that the expression of Armcx members is indeed important for the differentiation of RPE cells cultured *in vitro*. Additional evidence indicating the role of Armcx in RPE comes from the report that Armcx3 is downregulated in RPE-choroid samples from early AMD patients. Differentially expressed genes between AMD and age-matched normal individuals in RPE-choroid samples include Armcx3. Notably, while expression was high in the RPE-choroid, the authors did not find any Armcx expression in the retina samples, indicating that Armcx are important proteins specifically for the RPE layer (Newman et al., 2012). In agreement, our study showed Armcx1 and Armcx2 immuno staining localised in the RPE layer of human control and AMD patient eyes, further supporting the hypothesis that Armcx are important for the RPE cells. However, this needs to be supported with further immunohistochemistry analysis of more AMD donor eyes as in this study we were limited to just one eye.

Accumulation of ROS production inside mitochondria due to oxidative stress causes mitochondrial dysfunction and has been implicated in general aging-related disease including AMD (Srivastava and Kumar, 2015). Since the RPE mostly relies on oxidative phosphorylation to generate ATP, maintaining a functional population of mitochondria is critically important for RPE cells and mitochondrial degradation must be kept in check to avoid depletion of mitochondrial numbers. As discussed above our data suggests an important role for Armcx1 and Armcx2 in mediating mitochondrial degradation in non-differentiated ARPE-19 cells. Furthermore, Armcx2 overexpression resulted in

a strong mitochondrial aggregation phenotype, which resembles a similar phenotype to that observed in ARPE-19 cells after exposure to oxidative stress conditions with tert-butyl-hydroperoxide (Stripathi et al., 2016). Prohibitin was previously indicated as a mediator of the aggregated mitochondrial phenotype upon oxidative stress in ARPE-19 cells via interaction with mitochondrial trafficking components such as actin and vimentin. In the same study vimentin was found to reduce mitochondrial mobility (Goehler et al., 2004) and interestingly, has also been reported to interact with Armcx2 (Stripathi et al., 2016). Notably, in our study we identified reduced mitochondrial movement in Armcx2-depleted ARPE-19 cells; loss of interaction with Armcx2 may enhance the function of vimentin in reducing mitochondrial mobility. As discussed above, it appears that Armcx members are involved in mitochondrial dynamics in ARPE-19 cells. However, further research is needed in order to understand the role of Armcx in RPE function. Importantly, all experiments related to investigating the role of Armcx in RPE need to be performed in differentiated ARPE-19 and also to be supported by another RPE cell model, such as primary porcine RPE or iPS-derived RPE. In these systems the effect of Armcx overexpression can be observed in respect to some of the main RPE structural characteristics, such as tight junction formation, RPE65 levels and phagocytotic function. Importantly, adenoviral delivery of shRNA against Armcx1 and 2 needs to be optimised as an alternative method of manipulating post-mitotic RPE cells. Furthermore, it would be of interest to analyse Armcx1 and Armcx2 expression levels in a mouse model with dysfunctional RPE such as the Ccl2/Cx3crl double knockout (CCDKO) mouse line that is described with retinal degeneration features (Luhmann et al., 2012) and more recently,

a lasered mouse model of retinal degeneration leaving the abnormal apical-basal RPE surfaces and Bruch's membrane thickening (Ibbett et al., 2019).

7.3 Eutherian ARMCX constitute a family with non-overlapping functions

The Armcx gene family has been described to have arisen by retrotransposition from the Arm-containing gene Armc10 located on chromosome 7 exclusive to all vertebrates, and by subsequent tandem duplication events have occupied specifically the X chromosome of Eutherian mammals (López-Doménech et al., 2012). With the assumption of Armcx as retrotransposed genes, and thus dependent largely on the regulatory sequences of the incorporation site, they were suggested to be generally regulated and share related physiological functions and similar expression levels (López-Doménech et al., 2012). Generally, due to the high sequence similarities among redundant genes have been described as are a result of gene duplications (Wagner, 1996, Nowak et al., 1997, Coveney et al., 2008), and indeed Armcx/Armc10 members were indicated to be redundant (Coveney et al., 2008). However, important mechanisms in genome evolution and the acquisition of novel functions are strongly believed to be due to gene duplications (Wang et al., 2013). Moreover, the gene encoding Armc10 contains multiple exons, whereas Armcx coding sequences are held by a single exon (Simonin et al., 2004), suggesting that Armc10 function has been split into Armcx members.

Notably, there is still lack of evidence and understanding whether the emergence of Armcx family from Armc10 constitutes divergent evolution

towards additional functions or if the functions of Armc10 have been spread across the additional Armcx genes to allow more robust control in the more complex clade. Eutheria is a lineage in which the neocortex underwent significant enlargement, and a well-developed placenta was established (Puelles, 2001). Thus, the emergence of the Armcx cluster has been hypothesised to be linked to the development of a more complex nervous system in the Eutherian brain (López-Doménech et al., 2012).

In the present study we confirmed that the Armcx gene members, present only in Eutherians, are evolutionary descendent proteins of Armc10 gene and that the closest mammalian clade Marsupial crucially only possesses the Armc10 gene, indicating this as the last ancestor living before the expansion of Armcx family. From the phylogenetic analysis we observed that Armcx1, 2, 3 and 6 appear to be clustered as a separate sub-family from Armcx4 and 5, which are more closely related to GASP members. This was in agreement with the sequence analysis of Armcx/GAPSs, where Armcx4 and Armcx5 lacked the conserved MTS and TMD characteristics for Armc10/Armcx and showed more relation to GASP members. Importantly, we validated the conserved MTS in Armcx1, 2, 3 and 6 experimentally by mutational analysis of exogenously expressed Armcx-GFP fusion proteins, in which we observed complete loss of mitochondrial association once the sequence within the N-terminus was deleted. Furthermore, Armcx4 and 5 did only not show differences in their sequences, but also were differentially expressed in RPE differentiation *in vitro*, suggesting that Armcx members fulfil separate functions in these cells. In support of this, we observed that Armcx1 and Armcx2 affected mitochondrial motility and CCCP-induced mitophagy differently, probably by interacting with

different proteins in the mitochondrial trafficking machinery and/or participate in separate functions. Furthermore, Armcx1 and Armcx2 showed opposite regulation over Lamp2 expression further indicating that Armcx proteins do not perform the same functions. Upon Armcx1 depletion, Lamp2 expression appeared significantly upregulated, which phenotype was rescued by exogenous Armcx2. However, when Armcx2 was depleted, Lamp2 levels were decreased and Armcx1 overexpression was unable to rescue them.

Moreover, experiments where exogenous marsupial Armc10 was expressed were conducted in order to evaluate whether Armc10 can rescue Armcx1/Armcx2 induced phenotypes. Therefore, this will indicate whether Armc10 function has been retained during evolution of the Armcx members in Eutheria or novel functions have emerged. These experiments were performed where strong phenotypes were observed by Armcx1/Armcx2. Importantly, when marsupial Armc10 was exogenously expressed in Armcx1 knockdown cells, Lamp2 levels were not rescued, suggesting that Armcx1 might have gained a new function upon evolution, which importantly Armcx2 possesses too. Importantly, Armcx2 appeared to have retained its function in regulating Lamp2 from its ancestral Armc10, as exogenous Armc10 was able to rescue Lamp2 expression upon Armcx2 depletion. In support to this, the mitochondrial phenotype upon Armcx2 knockdown was also rescued by the expression of marsupial Armc10, although further imaging and quantitation is needed for a firm conclusion. This was, however, not true for Armcx1, where marsupial Armc10 was unable to recover the mitochondrial phenotype caused by the lack of Armcx1, further indicating that Armcx1 have gained a new function, different from its ancestor. We aimed to prepare siRNA resistant

plasmids for Armcx phenotype rescuing experiments as positive controls and to exclude any off-target effects of siRNA against Armcx1 and Armcx2. However, this was not achieved due to insufficient time. Furthermore, consistent with divergent functions, Armcx1 deficiency led to an increased Parkin puncta number, whereas Armcx2 depletion resulted in no change. Importantly, when marsupial Armc10 was overexpressed, Parkin activation was completely suppressed, but both Armcx1 and Armcx2 proteins were still able, however to less extent to activate Parkin. This suggests that regarding Parkin activation, Armcx1 and Armcx2 have gained new functions and/or lost one from their ancestral Armc10. Notably, further independent experiments are required to make firm conclusions. Notably, it would be worth investigating if Armc10 is able to rescue the upregulation of Parkin activation when Armcx1 is depleted.

Overall, this data strongly indicates that the emergence of Armcx has evolved in Eutheria did not occur to make redundant proteins, but rather represents divergent evolution towards novel functional proteins. Moreover, Armcx expansion can also be explained as a result of “asymmetrical evolution”, where similar genes after tandem duplication can generate substantially novel genes (Holland et al., 2017).

In conclusion, Armcx protein function has until now mostly been analysed in neurons, where Armcx3 is involved in axonal mitochondrial traffic (Lopez-Domenech et al.,2012). Here, with this work we confirmed that Armcx genes encode for mitochondrial targeting proteins. We show association with mitochondria of Armcx1, 2 and a clear indication of regulation of mitochondrial dynamics, mitochondrial degradation and thus mitochondrial homeostasis in

ARPE-19 cells. In addition, we show that Armcx members emerged during the early evolution of Eutheria to fulfil separate functions which are essential to meet the needs of the more complex clade.

Chapter 8 References

ABU-HELO, A. & SIMONIN, F. 2010. Identification and biological significance of G protein-coupled receptor associated sorting proteins (GASPs). *Pharmacol Ther,* 126**,** 244-50.

AHMADO, A., CARR, A. J., VUGLER, A. A., SEMO, M., GIAS, C., LAWRENCE, J. M., CHEN, L. L., CHEN, F. K., TUROWSKI, P., DA CRUZ, L. & COFFEY, P. J. 2011. Induction of differentiation by pyruvate and DMEM in the human retinal pigment epithelium cell line ARPE-19. *Invest Ophthalmol Vis Sci,* 52**,** 7148-59.

AN, Y., CHEN, C. Y., MOYER, B., ROTKIEWICZ, P., ELSLIGER, M. A., GODZIK, A., WILSON, I. A. & BALCH, W. E. 2009. Structural and functional analysis of the globular head domain of p115 provides insight into membrane tethering. *J Mol Biol,* 391**,** 26-41.

ANZELL, A. R., FOGO, G. M., GURM, Z., RAGHUNAYAKULA, S., WIDER, J. M., MAHERAS, K. J., EMAUS, K. J., BRYSON, T. D., WANG, M., NEUMAR, R. W., PRZYKLENK, K. & SANDERSON, T. H. 2021. Mitochondrial fission and mitophagy are independent mechanisms regulating ischemia/reperfusion injury in primary neurons. *Cell Death Dis,* 12**,** 475.

APTE, R. S., CHEN, D. S. & FERRARA, N. 2019. VEGF in Signaling and Disease: Beyond Discovery and Development. *Cell,* 176**,** 1248-1264.

BARNSTABLE, C. J. & TOMBRAN-TINK, J. 2004. Neuroprotective and antiangiogenic actions of PEDF in the eye: molecular targets and therapeutic potential. *Prog Retin Eye Res,* 23**,** 561-77.

BAROT, M., GOKULGANDHI, M. R. & MITRA, A. K. 2011. Mitochondrial dysfunction in retinal diseases. *Curr Eye Res,* 36**,** 1069-77.

BARTLETT, S. E., ENQUIST, J., HOPF, F. W., LEE, J. H., GLADHER, F., KHARAZIA, V., WALDHOER, M., MAILLIARD, W. S., ARMSTRONG, R., BONCI, A. & WHISTLER, J. L. 2005. Dopamine responsiveness is regulated by targeted sorting of D2 receptors. *Proc Natl Acad Sci U S A,* 102**,** 11521-6.

BAUER, N. C., DOETSCH, P. W. & CORBETT, A. H. 2015. Mechanisms Regulating Protein Localization. *Traffic,* 16**,** 1039-61.

BEAUSOLEIL, S. A., JEDRYCHOWSKI, M., SCHWARTZ, D., ELIAS, J. E., VILLÉN, J., LI, J., COHN, M. A., CANTLEY, L. C. & GYGI, S. P. 2004. Large-scale characterization of HeLa cell nuclear phosphoproteins. *Proc Natl Acad Sci U S A,* 101**,** 12130-5.

BERG, T. O., FENGSRUD, M., STRØMHAUG, P. E., BERG, T. & SEGLEN, P. O. 1998. Isolation and characterization of rat liver amphisomes. Evidence for fusion of autophagosomes with both early and late endosomes. *J Biol Chem,* 273**,** 21883-92.

BOLAND, M. L., CHOURASIA, A. H. & MACLEOD, K. F. 2013. Mitochondrial dysfunction in cancer. *Front Oncol,* 3**,** 292.

BONILHA, V. L. 2014. Retinal pigment epithelium (RPE) cytoskeleton in vivo and in vitro. *Exp Eye Res,* 126**,** 38-45.

BOOIJ, J. C., BAAS, D. C., BEISEKEEVA, J., GORGELS, T. G. & BERGEN, A. A. 2010. The dynamic nature of Bruch's membrane. *Prog Retin Eye Res,* 29**,** 1-18.

BOULTON, M. E. 2014. Studying melanin and lipofuscin in RPE cell culture models. *Exp Eye Res,* 126**,** 61-7.

BOUTET, E., LIEBERHERR, D., TOGNOLLI, M., SCHNEIDER, M. & BAIROCH, A. 2007. UniProtKB/Swiss-Prot. *Methods Mol Biol,* 406**,** 89-112.

BRECKWOLDT, M. O., PFISTER, F. M., BRADLEY, P. M., MARINKOVIC, P., WILLIAMS, P. R., BRILL, M. S., PLOMER, B., SCHMALZ, A., ST CLAIR, D. K., NAUMANN, R., GRIESBECK, O., SCHWARZLANDER, M., GODINHO, L., BAREYRE, F. M., DICK, T. P., KERSCHENSTEINER, M. & MISGELD, T. 2014. Multiparametric optical analysis of mitochondrial redox signals during neuronal physiology and pathology in vivo. *Nat Med,* 20**,** 555-60.

BRICKLEY, K. & STEPHENSON, F. A. 2011. Trafficking kinesin protein (TRAK)-mediated transport of mitochondria in axons of hippocampal neurons. *J Biol Chem,* 286**,** 18079-92.

BROWN, E. E., DEWEERD, A. J., ILDEFONSO, C. J., LEWIN, A. S. & ASH, J. D. 2019. Mitochondrial oxidative stress in the retinal pigment epithelium (RPE) led to metabolic dysfunction in both the RPE and retinal photoreceptors. *Redox Biol,* 24**,** 101201.

CALDWELL, R. B. & SLAPNICK, S. M. 1989. Increased cytochrome oxidase activity in the diabetic rat retinal pigment epithelium. *Invest Ophthalmol Vis Sci,* 30**,** 591-9.

CARIDI, B., DONCHEVA, D., SIVAPRASAD, S. & TUROWSKI, P. 2021. Galectins in the Pathogenesis of Common Retinal Disease. *Front Pharmacol,* 12**,** 687495.

CARRIE, C. & WHELAN, J. 2013. Widespread dual targeting of proteins in land plants: when, where, how and why. *Plant Signal Behav,* 8.

CHAN, D. C. 2006. Mitochondria: dynamic organelles in disease, aging, and development. *Cell,* 125**,** 1241-52.

CHANDEL, N. S. 2014. Mitochondria as signaling organelles. *BMC Biol,* 12**,** 34.

CHANDEL, N. S., MALTEPE, E., GOLDWASSER, E., MATHIEU, C. E., SIMON, M. C. & SCHUMACKER, P. T. 1998. Mitochondrial reactive

oxygen species trigger hypoxia-induced transcription. *Proc Natl Acad Sci U S A,* 95**,** 11715-20.

CHANG, K. T., NIESCIER, R. F. & MIN, K. T. 2011. Mitochondrial matrix Ca2+ as an intrinsic signal regulating mitochondrial motility in axons. *Proc Natl Acad Sci U S A,* 108**,** 15456-61.

CHEN, G., KROEMER, G. & KEPP, O. 2020. Mitophagy: An Emerging Role in Aging and Age-Associated Diseases. *Front Cell Dev Biol,* 8**,** 200.

CHEN, Z., LEI, C., WANG, C., LI, N., SRIVASTAVA, M., TANG, M., ZHANG, H., CHOI, J. M., JUNG, S. Y., QIN, J. & CHEN, J. 2019. Global phosphoproteomic analysis reveals ARMC10 as an AMPK substrate that regulates mitochondrial dynamics. *Nat Commun,* 10**,** 104.

CHO, B., CHO, H. M., JO, Y., KIM, H. D., SONG, M., MOON, C., KIM, H., KIM, K., SESAKI, H., RHYU, I. J., KIM, H. & SUN, W. 2017. Constriction of the mitochondrial inner compartment is a priming event for mitochondrial division. *Nat Commun,* 8**,** 15754.

CHOI, H. D., KIM, K.-Y., PARK, K. I., KIM, S.-H., PARK, S.-G., YU, S.-N., KIM, Y.-W., KIM, D. S., CHUNG, K. T. & AHN, S.-C. 2020. Dual role of reactive oxygen species in autophagy and apoptosis induced by compound PN in prostate cancer cells. *Molecular & Cellular Toxicology,* 17**,** 41-50.

CONSORTIUM, G. T. 2018. Erratum: Genetic effects on gene expression across human tissues. *Nature,* 553**,** 530.

COVENEY, D., ROSS, A. J., SLONE, J. D. & CAPEL, B. 2008. A microarray analysis of the XX Wnt4 mutant gonad targeted at the identification of genes involved in testis vascular differentiation. *Gene Expr Patterns,* 8**,** 529-37.

CUI, L., ZHAO, L. P., YE, J. Y., YANG, L., HUANG, Y., JIANG, X. P., ZHANG, Q., JIA, J. Z., ZHANG, D. X. & HUANG, Y. 2020. The Lysosomal Membrane Protein Lamp2 Alleviates Lysosomal Cell Death by

Promoting Autophagic Flux in Ischemic Cardiomyocytes. *Front Cell Dev Biol,* 8**,** 31.

DAGDA, R. K., CHERRA, S. J., 3RD, KULICH, S. M., TANDON, A., PARK, D. & CHU, C. T. 2009. Loss of PINK1 function promotes mitophagy through effects on oxidative stress and mitochondrial fission. *J Biol Chem,* 284**,** 13843-13855.

DEVI, T. S., YUMNAMCHA, T., YAO, F., SOMAYAJULU, M., KOWLURU, R. A. & SINGH, L. P. 2019. TXNIP mediates high glucose-induced mitophagic flux and lysosome enlargement in human retinal pigment epithelial cells. *Biol Open,* 8.

DIOT, A., MORTEN, K. & POULTON, J. 2016. Mitophagy plays a central role in mitochondrial ageing. *Mamm Genome,* 27**,** 381-95.

DOĞAN, T., MACDOUGALL, A., SAIDI, R., POGGIOLI, D., BATEMAN, A., O'DONOVAN, C. & MARTIN, M. J. 2016. UniProt-DAAC: domain architecture alignment and classification, a new method for automatic functional annotation in UniProtKB. *Bioinformatics,* 32**,** 2264-71.

DOMBI, E., MORTIBOYS, H. & POULTON, J. 2018. Modulating Mitophagy in Mitochondrial Disease. *Curr Med Chem,* 25**,** 5597-5612.

DOXAKI, C. & PALIKARAS, K. 2020. Neuronal Mitophagy: Friend or Foe? *Front Cell Dev Biol,* 8**,** 611938.

DUNN, K. C., AOTAKI-KEEN, A. E., PUTKEY, F. R. & HJELMELAND, L. M. 1996. ARPE-19, a human retinal pigment epithelial cell line with differentiated properties. *Exp Eye Res,* 62**,** 155-69.

EDGAR, R. C. 2004. MUSCLE: multiple sequence alignment with high accuracy and high throughput. *Nucleic Acids Res,* 32**,** 1792-7.

EISNER, V., PICARD, M. & HAJNOCZKY, G. 2018. Mitochondrial dynamics in adaptive and maladaptive cellular stress responses. *Nat Cell Biol,* 20**,** 755-765.

EVANS, M. D., DIZDAROGLU, M. & COOKE, M. S. 2004. Oxidative DNA damage and disease: induction, repair and significance. *Mutat Res,* 567**,** 1-61.

FEHER, J., KOVACS, I., ARTICO, M., CAVALLOTTI, C., PAPALE, A. & BALACCO GABRIELI, C. 2006. Mitochondrial alterations of retinal pigment epithelium in age-related macular degeneration. *Neurobiol Aging,* 27**,** 983-93.

FIELDS, M. A., DEL PRIORE, L. V., ADELMAN, R. A. & RIZZOLO, L. J. 2020. Interactions of the choroid, Bruch's membrane, retinal pigment epithelium, and neurosensory retina collaborate to form the outer blood-retinal-barrier. *Prog Retin Eye Res,* 76**,** 100803.

FILOMENI, G., DE ZIO, D. & CECCONI, F. 2015. Oxidative stress and autophagy: the clash between damage and metabolic needs. *Cell Death Differ,* 22**,** 377-88.

FRANSSON, A., RUUSALA, A. & ASPENSTROM, P. 2003. Atypical Rho GTPases have roles in mitochondrial homeostasis and apoptosis. *J Biol Chem,* 278**,** 6495-502.

FRIEDMAN, J. R., LACKNER, L. L., WEST, M., DIBENEDETTO, J. R., NUNNARI, J. & VOELTZ, G. K. 2011. ER tubules mark sites of mitochondrial division. *Science,* 334**,** 358-62.

FRIEDMAN, J. R. & NUNNARI, J. 2014. Mitochondrial form and function. *Nature,* 505**,** 335-43.

FUKASAWA, Y., TSUJI, J., FU, S. C., TOMII, K., HORTON, P. & IMAI, K. 2015. MitoFates: improved prediction of mitochondrial targeting sequences and their cleavage sites. *Mol Cell Proteomics,* 14**,** 1113-26.

GANESAN, V., WILLIS, S. D., CHANG, K. T., BELUCH, S., COOPER, K. F. & STRICH, R. 2019. Cyclin C directly stimulates Drp1 GTP affinity to mediate stress-induced mitochondrial hyperfission. *Mol Biol Cell,* 30**,** 302-311.

GEORGAKOPOULOS, N. D., WELLS, G. & CAMPANELLA, M. 2017. The pharmacological regulation of cellular mitophagy. *Nat Chem Biol,* 13**,** 136-146.

GLANCY, B., KIM, Y., KATTI, P. & WILLINGHAM, T. B. 2020. The Functional Impact of Mitochondrial Structure Across Subcellular Scales. *Front Physiol,* 11**,** 541040.

GOEHLER, H., LALOWSKI, M., STELZL, U., WAELTER, S., STROEDICKE, M., WORM, U., DROEGE, A., LINDENBERG, K. S., KNOBLICH, M., HAENIG, C., HERBST, M., SUOPANKI, J., SCHERZINGER, E., ABRAHAM, C., BAUER, B., HASENBANK, R., FRITZSCHE, A., LUDEWIG, A. H., BÜSSOW, K., COLEMAN, S. H., GUTEKUNST, C. A., LANDWEHRMEYER, B. G., LEHRACH, H. & WANKER, E. E. 2004. A protein interaction network links GIT1, an enhancer of huntingtin aggregation, to Huntington's disease. *Mol Cell,* 15**,** 853-65.

GOURAS, P., IVERT, L., NEURINGER, M. & NAGASAKI, T. 2016. Mitochondrial elongation in the macular RPE of aging monkeys, evidence of metabolic stress. *Graefes Arch Clin Exp Ophthalmol,* 254**,** 1221-7.

GUO, C., SUN, L., CHEN, X. & ZHANG, D. 2013. Oxidative stress, mitochondrial damage and neurodegenerative diseases. *Neural Regen Res,* 8**,** 2003-14.

HAM, S. J., LEE, D., YOO, H., JUN, K., SHIN, H. & CHUNG, J. 2020. Decision between mitophagy and apoptosis by Parkin via VDAC1 ubiquitination. *Proc Natl Acad Sci U S A,* 117**,** 4281-4291.

HATZFELD, M. 1999. The armadillo family of structural proteins. *Int Rev Cytol,* 186**,** 179-224.

HAZIM, R. A., VOLLAND, S., YEN, A., BURGESS, B. L. & WILLIAMS, D. S. 2019. Rapid differentiation of the human RPE cell line, ARPE-19, induced by nicotinamide. *Exp Eye Res,* 179**,** 18-24.

HEO, J. M., HARPER, N. J., PAULO, J. A., LI, M., XU, Q., COUGHLIN, M., ELLEDGE, S. J. & HARPER, J. W. 2019. Integrated proteogenetic analysis reveals the landscape of a mitochondrial-autophagosome synapse during PARK2-dependent mitophagy. *Sci Adv,* 5**,** eaay4624.

HOLLAND, P. W., MARLÉTAZ, F., MAESO, I., DUNWELL, T. L. & PAPS, J. 2017. New genes from old: asymmetric divergence of gene duplicates and the evolution of development. *Philos Trans R Soc Lond B Biol Sci,* 372.

HOON, M., OKAWA, H., DELLA SANTINA, L. & WONG, R. O. 2014. Functional architecture of the retina: development and disease. *Prog Retin Eye Res,* 42**,** 44-84.

HORNBECK, P. V., ZHANG, B., MURRAY, B., KORNHAUSER, J. M., LATHAM, V. & SKRZYPEK, E. 2015. PhosphoSitePlus, 2014: mutations, PTMs and recalibrations. *Nucleic Acids Res,* 43**,** D512-20.

HU, J. & BOK, D. 2001. A cell culture medium that supports the differentiation of human retinal pigment epithelium into functionally polarized monolayers. *Mol Vis,* 7**,** 14-9.

HYTTINEN, J. M. T., VIIRI, J., KAARNIRANTA, K. & BLASIAK, J. 2018. Mitochondrial quality control in AMD: does mitophagy play a pivotal role? *Cell Mol Life Sci,* 75**,** 2991-3008.

IBBETT, P., GOVERDHAN, S. V., PIPI, E., CHOUHAN, J. K., KEELING, E., ANGUS, E. M., SCOTT, J. A., GATHERER, M., PAGE, A., TEELING, J. L., LOTERY, A. J. & ARJUNA RATNAYAKA, J. 2019. A lasered mouse model of retinal degeneration displays progressive outer retinal pathology providing insights into early geographic atrophy. *Sci Rep,* 9**,** 7475.

INANA, G., MURAT, C., AN, W., YAO, X., HARRIS, I. R. & CAO, J. 2018. RPE phagocytic function declines in age-related macular degeneration and

is rescued by human umbilical tissue derived cells. *J Transl Med,* 16**,** 63.

ISEKI, H., TAKEDA, A., ANDOH, T., KUWABARA, K., TAKAHASHI, N., KUROCHKIN, I. V., ISHIDA, H., OKAZAKI, Y. & KOYAMA, I. 2012. ALEX1 suppresses colony formation ability of human colorectal carcinoma cell lines. *Cancer Sci,* 103**,** 1267-71.

IVANKOVIC, D., CHAU, K. Y., SCHAPIRA, A. H. & GEGG, M. E. 2016. Mitochondrial and lysosomal biogenesis are activated following PINK1/parkin-mediated mitophagy. *J Neurochem,* 136**,** 388-402.

JAVADPOUR, M. M., EILERS, M., GROESBEEK, M. & SMITH, S. O. 1999. Helix packing in polytopic membrane proteins: role of glycine in transmembrane helix association. *Biophys J,* 77**,** 1609-18.

KARGL, J., BALENGA, N. A., PLATZER, W., MARTINI, L., WHISTLER, J. L. & WALDHOER, M. 2012. The GPCR-associated sorting protein 1 regulates ligand-induced down-regulation of GPR55. *Br J Pharmacol,* 165**,** 2611-9.

KILLACKEY, S. A., PHILPOTT, D. J. & GIRARDIN, S. E. 2020. Mitophagy pathways in health and disease. *J Cell Biol,* 219.

KIM, J. H., PARK, S., CHUNG, H. & OH, S. 2015. Wnt5a attenuates the pathogenic effects of the Wnt/β-catenin pathway in human retinal pigment epithelial cells via down-regulating β-catenin and Snail. *BMB Rep,* 48**,** 525-30.

KIRBY, A. 2016. *ARMCX proteins as regulators of mitochondrial dynamics in the retinal pigment epithelium.* Mres in Brain Sciences UCL.

KIYAMA, A., ISOJIMA, Y. & NAGAI, K. 2006. Role of Per1-interacting protein of the suprachiasmatic nucleus in NGF mediated neuronal survival. *Biochem Biophys Res Commun,* 339**,** 514-9.

KLECKER, T., BOCKLER, S. & WESTERMANN, B. 2014. Making connections: interorganelle contacts orchestrate mitochondrial behavior. *Trends Cell Biol,* 24**,** 537-45.

KONO, M., GOLETZ, P. W. & CROUCH, R. K. 2008. 11-cis- and all-trans-retinols can activate rod opsin: rational design of the visual cycle. *Biochemistry,* 47**,** 7567-71.

KOROBOVA, F., RAMABHADRAN, V. & HIGGS, H. N. 2013. An actin-dependent step in mitochondrial fission mediated by the ER-associated formin INF2. *Science,* 339**,** 464-7.

KUROCHKIN, I. V., YONEMITSU, N., FUNAHASHI, S. I. & NOMURA, H. 2001. ALEX1, a novel human armadillo repeat protein that is expressed differentially in normal tissues and carcinomas. *Biochem Biophys Res Commun,* 280**,** 340-7.

KUSAMA, Y., TAKAYANAGI, S., TATEGU, M. & YOSHIDA, K. 2010. Expression and tissue distribution of human X-linked armadillo repeat containing-6. *Exp Ther Med,* 1**,** 395-399.

LAMB, T. D. 2016. Why rods and cones? *Eye (Lond),* 30**,** 179-85.

LEE, H. & YOON, Y. 2014. Transient contraction of mitochondria induces depolarization through the inner membrane dynamin OPA1 protein. *J Biol Chem,* 289**,** 11862-11872.

LEE, J. J., SANCHEZ-MARTINEZ, A., MARTINEZ ZARATE, A., BENINCA, C., MAYOR, U., CLAGUE, M. J. & WHITWORTH, A. J. 2018. Basal mitophagy is widespread in Drosophila but minimally affected by loss of Pink1 or parkin. *J Cell Biol,* 217**,** 1613-1622.

LEHMANN, G. L., BENEDICTO, I., PHILP, N. J. & RODRIGUEZ-BOULAN, E. 2014. Plasma membrane protein polarity and trafficking in RPE cells: past, present and future. *Exp Eye Res,* 126**,** 5-15.

LEMASTERS, J. J., THERUVATH, T. P., ZHONG, Z. & NIEMINEN, A. L. 2009. Mitochondrial calcium and the permeability transition in cell death. *Biochim Biophys Acta,* 1787**,** 1395-401.

LEONARD, A. P., CAMERON, R. B., SPEISER, J. L., WOLF, B. J., PETERSON, Y. K., SCHNELLMANN, R. G., BEESON, C. C. & ROHRER, B. 2015. Quantitative analysis of mitochondrial morphology and membrane potential in living cells using high-content imaging, machine learning, and morphological binning. *Biochim Biophys Acta,* 1853**,** 348-60.

LI, G. B., ZHANG, H. W., FU, R. Q., HU, X. Y., LIU, L., LI, Y. N., LIU, Y. X., LIU, X., HU, J. J., DENG, Q., LUO, Q. S., ZHANG, R. & GAO, N. 2018. Mitochondrial fission and mitophagy depend on cofilin-mediated actin depolymerization activity at the mitochondrial fission site. *Oncogene,* 37**,** 1485-1502.

LIU, C., LIN, C., YAO, J., WEI, Q., XING, G. & CAO, X. 2017. Dynamic expression analysis of armc10, the homologous gene of human GPRASP2, in zebrafish embryos. *Mol Med Rep,* 16**,** 5931-5937.

LIU, H. Y., LIAO, P. C., CHUANG, K. T. & KAO, M. C. 2011. Mitochondrial targeting of human NADH dehydrogenase (ubiquinone) flavoprotein 2 (NDUFV2) and its association with early-onset hypertrophic cardiomyopathy and encephalopathy. *J Biomed Sci,* 18**,** 29.

LIU, X., LIAO, X., RAO, X., WANG, B., ZHANG, J., XU, G., JIANG, X., QIN, X., CHEN, C. & ZOU, Z. 2020. The lysosomal membrane protein LAMP-2 is dispensable for PINK1/Parkin-mediated mitophagy. *FEBS Lett,* 594**,** 823-840.

LÓPEZ-DOMÉNECH, G., SERRAT, R., MIRRA, S., D'ANIELLO, S., SOMORJAI, I., ABAD, A., VITUREIRA, N., GARCÍA-ARUMÍ, E., ALONSO, M. T., RODRIGUEZ-PRADOS, M., BURGAYA, F., ANDREU, A. L., GARCÍA-SANCHO, J., TRULLAS, R., GARCIA-FERNÀNDEZ, J. & SORIANO, E. 2012. The Eutherian Armcx genes

regulate mitochondrial trafficking in neurons and interact with Miro and Trak2. *Nat Commun,* 3**,** 814.

LUHMANN, U. F., LANGE, C. A., ROBBIE, S., MUNRO, P. M., COWING, J. A., ARMER, H. E., LUONG, V., CARVALHO, L. S., MACLAREN, R. E., FITZKE, F. W., BAINBRIDGE, J. W. & ALI, R. R. 2012. Differential modulation of retinal degeneration by Ccl2 and Cx3cr1 chemokine signalling. *PLoS One,* 7**,** e35551.

LUND, R. D., ADAMSON, P., SAUVE, Y., KEEGAN, D. J., GIRMAN, S. V., WANG, S., WINTON, H., KANUGA, N., KWAN, A. S., BEAUCHENE, L., ZERBIB, A., HETHERINGTON, L., COURAUD, P. O., COFFEY, P. & GREENWOOD, J. 2001. Subretinal transplantation of genetically modified human cell lines attenuates loss of visual function in dystrophic rats. *Proc Natl Acad Sci U S A,* 98**,** 9942-7.

MA, K., CHEN, G., LI, W., KEPP, O., ZHU, Y. & CHEN, Q. 2020. Mitophagy, Mitochondrial Homeostasis, and Cell Fate. *Front Cell Dev Biol,* 8**,** 467.

MAMINISHKIS, A., CHEN, S., JALICKEE, S., BANZON, T., SHI, G., WANG, F. E., EHALT, T., HAMMER, J. A. & MILLER, S. S. 2006. Confluent monolayers of cultured human fetal retinal pigment epithelium exhibit morphology and physiology of native tissue. *Invest Ophthalmol Vis Sci,* 47**,** 3612-24.

MARMOR, M. F. 1990. Control of subretinal fluid: experimental and clinical studies. *Eye (Lond),* 4 (Pt 2)**,** 340-4.

MARMORSTEIN, A. D. 2001. The polarity of the retinal pigment epithelium. *Traffic,* 2**,** 867-72.

MARNEROS, A. G., KEENE, D. R., HANSEN, U., FUKAI, N., MOULTON, K., GOLETZ, P. L., MOISEYEV, G., PAWLYK, B. S., HALFTER, W., DONG, S., SHIBATA, M., LI, T., CROUCH, R. K., BRUCKNER, P. & OLSEN, B. R. 2004. Collagen XVIII/endostatin is essential for vision and retinal pigment epithelial function. *EMBO J,* 23**,** 89-99.

MASLAND, R. H. 2001. The fundamental plan of the retina. *Nat Neurosci,* 4**,** 877-86.

MAZZONI, F., SAFA, H. & FINNEMANN, S. C. 2014. Understanding photoreceptor outer segment phagocytosis: use and utility of RPE cells in culture. *Exp Eye Res,* 126**,** 51-60.

MCCARRON, J. G., WILSON, C., SANDISON, M. E., OLSON, M. L., GIRKIN, J. M., SAUNTER, C. & CHALMERS, S. 2013. From structure to function: mitochondrial morphology, motion and shaping in vascular smooth muscle. *J Vasc Res,* 50**,** 357-71.

MCGUFFIN, L. J., BRYSON, K. & JONES, D. T. 2000. The PSIPRED protein structure prediction server. *Bioinformatics,* 16**,** 404-5.

MCLELLAND, G. L., SOUBANNIER, V., CHEN, C. X., MCBRIDE, H. M. & FON, E. A. 2014. Parkin and PINK1 function in a vesicular trafficking pathway regulating mitochondrial quality control. *Embo j,* 33**,** 282-95.

MCLENACHAN, S., HAO, E., ZHANG, D., ZHANG, L., EDEL, M. & CHEN, F. 2017. Bioengineered Bruch's-like extracellular matrix promotes retinal pigment epithelial differentiation. *Biochem Biophys Rep,* 10**,** 178-185.

MCWILLIAM, H., LI, W., ULUDAG, M., SQUIZZATO, S., PARK, Y. M., BUSO, N., COWLEY, A. P. & LOPEZ, R. 2013. Analysis Tool Web Services from the EMBL-EBI. *Nucleic Acids Res,* 41**,** W597-600.

MCWILLIAMS, T. G., PRESCOTT, A. R., ALLEN, G. F., TAMJAR, J., MUNSON, M. J., THOMSON, C., MUQIT, M. M. & GANLEY, I. G. 2016. mito-QC illuminates mitophagy and mitochondrial architecture in vivo. *J Cell Biol,* 214**,** 333-45.

MCWILLIAMS, T. G., PRESCOTT, A. R., MONTAVA-GARRIGA, L., BALL, G., SINGH, F., BARINI, E., MUQIT, M. M. K., BROOKS, S. P. & GANLEY, I. G. 2018. Basal Mitophagy Occurs Independently of PINK1 in Mouse Tissues of High Metabolic Demand. *Cell Metab,* 27**,** 439-449.e5.

MEIER, S., NEUPERT, W. & HERRMANN, J. M. 2005. Proline residues of transmembrane domains determine the sorting of inner membrane proteins in mitochondria. *J Cell Biol,* 170**,** 881-8.

MIRRA, S., ULLOA, F., GUTIERREZ-VALLEJO, I., MARTÌ, E. & SORIANO, E. 2016. Function of Armcx3 and Armc10/SVH Genes in the Regulation of Progenitor Proliferation and Neural Differentiation in the Chicken Spinal Cord. *Front Cell Neurosci,* 10**,** 47.

MITRA, K., WUNDER, C., ROYSAM, B., LIN, G. & LIPPINCOTT-SCHWARTZ, J. 2009. A hyperfused mitochondrial state achieved at G1-S regulates cyclin E buildup and entry into S phase. *Proc Natl Acad Sci U S A,* 106**,** 11960-5.

MIYAZONO, Y., HIRASHIMA, S., ISHIHARA, N., KUSUKAWA, J., NAKAMURA, K. I. & OHTA, K. 2018. Uncoupled mitochondria quickly shorten along their long axis to form indented spheroids, instead of rings, in a fission-independent manner. *Sci Rep,* 8**,** 350.

MONTAVA-GARRIGA, L. & GANLEY, I. G. 2020. Outstanding Questions in Mitophagy: What We Do and Do Not Know. *J Mol Biol,* 432**,** 206-230.

MOU, Z., TAPPER, A. R. & GARDNER, P. D. 2009. The armadillo repeat-containing protein, ARMCX3, physically and functionally interacts with the developmental regulatory factor Sox10. *J Biol Chem,* 284**,** 13629-13640.

NAYLOR, A., HOPKINS, A., HUDSON, N. & CAMPBELL, M. 2019. Tight Junctions of the Outer Blood Retina Barrier. *Int J Mol Sci,* 21.

NEWMAN, A. M., GALLO, N. B., HANCOX, L. S., MILLER, N. J., RADEKE, C. M., MALONEY, M. A., COOPER, J. B., HAGEMAN, G. S., ANDERSON, D. H., JOHNSON, L. V. & RADEKE, M. J. 2012. Systems-level analysis of age-related macular degeneration reveals global biomarkers and phenotype-specific functional networks. *Genome Med,* 4**,** 16.

NISHINO, I., FU, J., TANJI, K., YAMADA, T., SHIMOJO, S., KOORI, T., MORA, M., RIGGS, J. E., OH, S. J., KOGA, Y., SUE, C. M., YAMAMOTO, A., MURAKAMI, N., SHANSKE, S., BYRNE, E., BONILLA, E., NONAKA, I., DIMAURO, S. & HIRANO, M. 2000. Primary LAMP-2 deficiency causes X-linked vacuolar cardiomyopathy and myopathy (Danon disease). *Nature,* 406**,** 906-10.

NITA, M. & GRZYBOWSKI, A. 2016. The Role of the Reactive Oxygen Species and Oxidative Stress in the Pathomechanism of the Age-Related Ocular Diseases and Other Pathologies of the Anterior and Posterior Eye Segments in Adults. *Oxid Med Cell Longev,* 2016**,** 3164734.

NOTOMI, S., ISHIHARA, K., EFSTATHIOU, N. E., LEE, J. J., HISATOMI, T., TACHIBANA, T., KONSTANTINOU, E. K., UETA, T., MURAKAMI, Y., MAIDANA, D. E., IKEDA, Y., KUME, S., TERASAKI, H., SONODA, S., BLANZ, J., YOUNG, L., SAKAMOTO, T., SONODA, K. H., SAFTIG, P., ISHIBASHI, T., MILLER, J. W., KROEMER, G. & VAVVAS, D. G. 2019. Genetic LAMP2 deficiency accelerates the age-associated formation of basal laminar deposits in the retina. *Proc Natl Acad Sci U S A,* 116**,** 23724-23734.

NOWAK, J. Z. 2006. Age-related macular degeneration (AMD): pathogenesis and therapy. *Pharmacol Rep,* 58**,** 353-63.

NOWAK, J. Z. 2014. AMD--the retinal disease with an unprecised etiopathogenesis: in search of effective therapeutics. *Acta Pol Pharm,* 71**,** 900-16.

NOWAK, M. A., BOERLIJST, M. C., COOKE, J. & SMITH, J. M. 1997. Evolution of genetic redundancy. *Nature,* 388**,** 167-71.

OKATSU, K., KIMURA, M., OKA, T., TANAKA, K. & MATSUDA, N. 2015. Unconventional PINK1 localization to the outer membrane of depolarized mitochondria drives Parkin recruitment. *J Cell Sci,* 128**,** 964-78.

OSELLAME, L. D., BLACKER, T. S. & DUCHEN, M. R. 2012. Cellular and molecular mechanisms of mitochondrial function. *Best Pract Res Clin Endocrinol Metab,* 26**,** 711-23.

OWEN, C. G., JARRAR, Z., WORMALD, R., COOK, D. G., FLETCHER, A. E. & RUDNICKA, A. R. 2012. The estimated prevalence and incidence of late stage age related macular degeneration in the UK. *Br J Ophthalmol,* 96**,** 752-6.

OZAWA, M., TERADA, H. & PEDRAZA, C. 1995. The fourth armadillo repeat of plakoglobin (gamma-catenin) is required for its high affinity binding to the cytoplasmic domains of E-cadherin and desmosomal cadherin Dsg2, and the tumor suppressor APC protein. *J Biochem,* 118**,** 1077-82.

PALIKARAS, K., LIONAKI, E. & TAVERNARAKIS, N. 2018. Mechanisms of mitophagy in cellular homeostasis, physiology and pathology. *Nat Cell Biol,* 20**,** 1013-1022.

PARK, Y. S., CHOI, S. E. & KOH, H. C. 2018. PGAM5 regulates PINK1/Parkin-mediated mitophagy via DRP1 in CCCP-induced mitochondrial dysfunction. *Toxicol Lett,* 284**,** 120-128.

PARZYCH, K. R. & KLIONSKY, D. J. 2014. An overview of autophagy: morphology, mechanism, and regulation. *Antioxid Redox Signal,* 20**,** 460-73.

PELLEGRINI, M., MARCOTTE, E. M., THOMPSON, M. J., EISENBERG, D. & YEATES, T. O. 1999. Assigning protein functions by comparative genome analysis: protein phylogenetic profiles. *Proc Natl Acad Sci U S A,* 96**,** 4285-8.

PI, H., XU, S., ZHANG, L., GUO, P., LI, Y., XIE, J., TIAN, L., HE, M., LU, Y., LI, M., ZHANG, Y., ZHONG, M., XIANG, Y., DENG, L., ZHOU, Z. & YU, Z. 2013. Dynamin 1-like-dependent mitochondrial fission initiates

overactive mitophagy in the hepatotoxicity of cadmium. *Autophagy,* 9**,** 1780-800.

PICAUD, S., DALKARA, D., MARAZOVA, K., GOUREAU, O., ROSKA, B. & SAHEL, J. A. 2019. The primate model for understanding and restoring vision. *Proc Natl Acad Sci U S A*, 116, 26280-7

PUELLES, L. 2001. Brain segmentation and forebrain development in amniotes. *Brain Res Bull,* 55**,** 695-710.

PUGAZHENDHI, A., HUBBELL, M., JAIRAM, P. & AMBATI, B. 2021. Neovascular Macular Degeneration: A Review of Etiology, Risk Factors, and Recent Advances in Research and Therapy. *Int J Mol Sci,* 22.

PURVES, D., AUGUSTINE, G.J., FITZPATRICK, D., KATZ, L., LAMANTIA, A.-S., MCNAMARA, J. AND WILLIAMS, S.M., 2004. The Retina. *Neuroscience.* 3rd ed. Sunderland (MA): Sinauer Associates.

RANGACHARI, K., JEYALAXMI, J., ESWARI PANDARANAYAKA, P. J., PRASANTHI, N., SUNDARESAN, P., KRISHNADAS, S. R. & KRISHNASWAMY, S. 2011. Significance of G-X-W motif in the myocilin olfactomedin domain. *J Ocul Biol Dis Infor,* 4**,** 154-8.

REHBERG, S., LISCHKA, P., GLASER, G., STAMMINGER, T., WEGNER, M. & ROSORIUS, O. 2002. Sox10 is an active nucleocytoplasmic shuttle protein, and shuttling is crucial for Sox10-mediated transactivation. *Mol Cell Biol,* 22**,** 5826-34.

RIZZOLO, L. J. 2014. Barrier properties of cultured retinal pigment epithelium. *Exp Eye Res,* 126**,** 16-26.

ROTH, A. C., GONNET, G. H. & DESSIMOZ, C. 2008. Algorithm of OMA for large-scale orthology inference. *BMC Bioinformatics,* 9**,** 518.

SAITO, T. & SADOSHIMA, J. 2015. Molecular mechanisms of mitochondrial autophagy/mitophagy in the heart. *Circ Res,* 116**,** 1477-90.

SAMUEL, W., JAWORSKI, C., POSTNIKOVA, O. A., KUTTY, R. K., DUNCAN, T., TAN, L. X., POLIAKOV, E., LAKKARAJU, A. & REDMOND, T. M. 2017. Appropriately differentiated ARPE-19 cells regain phenotype and gene expression profiles similar to those of native RPE cells. *Mol Vis,* 23**,** 60-89.

SANTEL, A. & FULLER, M. T. 2001. Control of mitochondrial morphology by a human mitofusin. *J Cell Sci,* 114**,** 867-74.

SAOTOME, M., SAFIULINA, D., SZABADKAI, G., DAS, S., FRANSSON, A., ASPENSTROM, P., RIZZUTO, R. & HAJNOCZKY, G. 2008. Bidirectional Ca2+-dependent control of mitochondrial dynamics by the Miro GTPase. *Proc Natl Acad Sci U S A,* 105**,** 20728-33.

SCHERZ-SHOUVAL, R. & ELAZAR, Z. 2007. ROS, mitochondria and the regulation of autophagy. *Trends Cell Biol,* 17**,** 422-7.

SCHNEIDER, C. A., RASBAND, W. S. & ELICEIRI, K. W. 2012. NIH Image to ImageJ: 25 years of image analysis. *Nat Methods,* 9**,** 671-5.

SEAGLE, B. L., REZAI, K. A., KOBORI, Y., GASYNA, E. M., REZAEI, K. A. & NORRIS, J. R., JR. 2005. Melanin photoprotection in the human retinal pigment epithelium and its correlation with light-induced cell apoptosis. *Proc Natl Acad Sci U S A,* 102**,** 8978-83.

SEO, B. J., YOON, S. H. & DO, J. T. 2018. Mitochondrial Dynamics in Stem Cells and Differentiation. *Int J Mol Sci,* 19.

SERRAT, R., LÓPEZ-DOMÉNECH, G., MIRRA, S., QUEVEDO, M., GARCIA-FERNÀNDEZ, J., ULLOA, F., BURGAYA, F. & SORIANO, E. 2013. The non-canonical Wnt/PKC pathway regulates mitochondrial dynamics through degradation of the arm-like domain-containing protein Alex3. *PLoS One,* 8**,** e67773.

SHEN, J., ZHANG, J. H., XIAO, H., WU, J. M., HE, K. M., LV, Z. Z., LI, Z. J., XU, M. & ZHANG, Y. Y. 2018. Mitochondria are transported along

microtubules in membrane nanotubes to rescue distressed cardiomyocytes from apoptosis. *Cell Death Dis,* 9**,** 81.

SHENG, Z. H. 2014. Mitochondrial trafficking and anchoring in neurons: New insight and implications. *J Cell Biol,* 204**,** 1087-98.

SIMO, R., VILLARROEL, M., CORRALIZA, L., HERNANDEZ, C. & GARCIA-RAMIREZ, M. 2010. The retinal pigment epithelium: something more than a constituent of the blood-retinal barrier--implications for the pathogenesis of diabetic retinopathy. *J Biomed Biotechnol,* 2010**,** 190724.

SIMONIN, F., KARCHER, P., BOEUF, J. J., MATIFAS, A. & KIEFFER, B. L. 2004. Identification of a novel family of G protein-coupled receptor associated sorting proteins. *J Neurochem,* 89**,** 766-75.

SMITH, C. A., MCCLIVE, P. J. & SINCLAIR, A. H. 2005. Temporal and spatial expression profile of the novel armadillo-related gene, Alex2, during testicular differentiation in the mouse embryo. *Dev Dyn,* 233**,** 188-93.

SPARROW, J. R., HICKS, D. & HAMEL, C. P. 2010. The retinal pigment epithelium in health and disease. *Curr Mol Med,* 10**,** 802-23.

SRIDEVI GURUBARAN, I., VIIRI, J., KOSKELA, A., HYTTINEN, J. M. T., PATERNO, J. J., KIS, G., ANTAL, M., URTTI, A., KAUPPINEN, A., FELSZEGHY, S. & KAARNIRANTA, K. 2020. Mitophagy in the Retinal Pigment Epithelium of Dry Age-Related Macular Degeneration Investigated in the NFE2L2/PGC-1α(-/-) Mouse Model. *Int J Mol Sci,* 21.

SRIPATHI, S. R., HE, W., SYLVESTER, O., NEKSUMI, M., UM, J. Y., DLUYA, T., BERNSTEIN, P. S. & JAHNG, W. J. 2016. Altered Cytoskeleton as a Mitochondrial Decay Signature in the Retinal Pigment Epithelium. *Protein J,* 35**,** 179-92.

SRIVASTAVA, K. K. & KUMAR, R. 2015. Stress, oxidative injury and disease. *Indian J Clin Biochem,* 30**,** 3-10.

STRAUSS, O. 1995. The Retinal Pigment Epithelium. *In:* KOLB, H., FERNANDEZ, E. & NELSON, R. (eds.) *Webvision: The Organization of the Retina and Visual System.* Salt Lake City (UT): University of Utah Health Sciences Center

STRAUSS, O. 2005. The retinal pigment epithelium in visual function. *Physiol Rev,* 85**,** 845-81.

SUAREZ-RIVERO, J. M., VILLANUEVA-PAZ, M., DE LA CRUZ-OJEDA, P., DE LA MATA, M., COTAN, D., OROPESA-AVILA, M., DE LAVERA, I., ALVAREZ-CORDOBA, M., LUZON-HIDALGO, R. & SANCHEZ-ALCAZAR, J. A. 2016. Mitochondrial Dynamics in Mitochondrial Diseases. *Diseases,* 5.

SUGIURA, A., MCLELLAND, G. L., FON, E. A. & MCBRIDE, H. M. 2014. A new pathway for mitochondrial quality control: mitochondrial-derived vesicles. *Embo j,* 33**,** 2142-56.

TECHNOLOGIES, I. D. Codon optimisation tool.

TERLUK, M. R., KAPPHAHN, R. J., SOUKUP, L. M., GONG, H., GALLARDO, C., MONTEZUMA, S. R. & FERRINGTON, D. A. 2015. Investigating mitochondria as a target for treating age-related macular degeneration. *J Neurosci,* 35**,** 7304-11.

TERMAN, A., KURZ, T., NAVRATIL, M., ARRIAGA, E. A. & BRUNK, U. T. 2010. Mitochondrial turnover and aging of long-lived postmitotic cells: the mitochondrial-lysosomal axis theory of aging. *Antioxid Redox Signal,* 12**,** 503-35.

TEWARI, R., BAILES, E., BUNTING, K. A. & COATES, J. C. 2010. Armadillo-repeat protein functions: questions for little creatures. *Trends Cell Biol,* 20**,** 470-81.

THAI, P. N., SEIDLMAYER, L. K., MILLER, C., FERRERO, M., DORN, G. W., II, SCHAEFER, S., BERS, D. M. & DEDKOVA, E. N. 2019. Mitochondrial Quality Control in Aging and Heart Failure: Influence of

Ketone Bodies and Mitofusin-Stabilizing Peptides. *Front Physiol,* 10**,** 382.

TIAN, L., POTUS, F., WU, D., DASGUPTA, A., CHEN, K. H., MEWBURN, J., LIMA, P. & ARCHER, S. L. 2018. Increased Drp1-Mediated Mitochondrial Fission Promotes Proliferation and Collagen Production by Right Ventricular Fibroblasts in Experimental Pulmonary Arterial Hypertension. *Front Physiol,* 9**,** 828.

TOYAMA, E. Q., HERZIG, S., COURCHET, J., LEWIS, T. L., JR., LOSON, O. C., HELLBERG, K., YOUNG, N. P., CHEN, H., POLLEUX, F., CHAN, D. C. & SHAW, R. J. 2016. Metabolism. AMP-activated protein kinase mediates mitochondrial fission in response to energy stress. *Science,* 351**,** 275-281.

TSIN, A., BETTS-OBREGON, B. & GRIGSBY, J. 2018. Visual cycle proteins: Structure, function, and roles in human retinal disease. *J Biol Chem,* 293**,** 13016-13021.

TUROWSKI, P., ADAMSON, P., SATHIA, J., ZHANG, J. J., MOSS, S. E., AYLWARD, G. W., HAYES, M. J., KANUGA, N. & GREENWOOD, J. 2004. Basement membrane-dependent modification of phenotype and gene expression in human retinal pigment epithelial ARPE-19 cells. *Invest Ophthalmol Vis Sci,* 45**,** 2786-94.

TUROWSKI, P., MARTINELLI, R., CRAWFORD, R., WATERIDGE, D., PAPAGEORGIOU, A. P., LAMPUGNANI, M. G., GAMP, A. C., VESTWEBER, D., ADAMSON, P., DEJANA, E. & GREENWOOD, J. 2008. Phosphorylation of vascular endothelial cadherin controls lymphocyte emigration. *J Cell Sci,* 121**,** 29-37.

UYAMA, H., MANDAI, M. & TAKAHASHI, M. 2021. Stem-cell-based therapies for retinal degenerative diseases: Current challenges in the establishment of new treatment strategies. *Dev Growth Differ,* 63**,** 59-71.

VALENTE, A. J., MADDALENA, L. A., ROBB, E. L., MORADI, F. & STUART, J. A. 2017. A simple ImageJ macro tool for analyzing mitochondrial network morphology in mammalian cell culture. *Acta Histochem,* 119**,** 315-326.

VITILLO, L., DURANCE, C., HEWITT, Z., MOORE, H., SMITH, A. & VALLIER, L. 2020. GMP-grade neural progenitor derivation and differentiation from clinical-grade human embryonic stem cells. *Stem Cell Res Ther,* 11**,** 406.

WAGNER, A. 1996. Genetic redundancy caused by gene duplications and its evolution in networks of transcriptional regulators. *Biol Cybern,* 74**,** 557-67.

WALSH, T. G., VAN DEN BOSCH, M. T. J., LEWIS, K. E., WILLIAMS, C. M. & POOLE, A. W. 2018. Loss of the mitochondrial kinase PINK1 does not alter platelet function. *Sci Rep,* 8**,** 14377.

WALTERS, R. F. & DEGRADO, W. F. 2006. Helix-packing motifs in membrane proteins. *Proc Natl Acad Sci U S A,* 103**,** 13658-63.

WANG, K. & KLIONSKY, D. J. 2011. Mitochondria removal by autophagy. *Autophagy,* 7**,** 297-300.

WANG, T., ZHONG, H., QIN, Y., WEI, W., LI, Z., HUANG, M. & LUO, X. 2020. ARMCX Family Gene Expression Analysis and Potential Prognostic Biomarkers for Prediction of Clinical Outcome in Patients with Gastric Carcinoma. *Biomed Res Int,* 2020**,** 3575038.

WANG, Y., TAN, X. & PATERSON, A. H. 2013. Different patterns of gene structure divergence following gene duplication in Arabidopsis. *BMC Genomics,* 14**,** 652.

WASMEIER, C., HUME, A. N., BOLASCO, G. & SEABRA, M. C. 2008. Melanosomes at a glance. *J Cell Sci,* 121**,** 3995-9.

WESTERMANN, B. 2015. The mitochondria-plasma membrane contact site. *Curr Opin Cell Biol,* 35**,** 1-6.

WINTER, E. E. & PONTING, C. P. 2005. Mammalian BEX, WEX and GASP genes: coding and non-coding chimaerism sustained by gene conversion events. *BMC Evol Biol,* 5**,** 54.

WONG, W. L., SU, X., LI, X., CHEUNG, C. M., KLEIN, R., CHENG, C. Y. & WONG, T. Y. 2014. Global prevalence of age-related macular degeneration and disease burden projection for 2020 and 2040: a systematic review and meta-analysis. *Lancet Glob Health,* 2**,** e106-16.

WONG, Y. C., YSSELSTEIN, D. & KRAINC, D. 2018. Mitochondria-lysosome contacts regulate mitochondrial fission via RAB7 GTP hydrolysis. *Nature,* 554**,** 382-386.

XIAN, H., YANG, Q., XIAO, L., SHEN, H. M. & LIOU, Y. C. 2019. STX17 dynamically regulated by Fis1 induces mitophagy via hierarchical macroautophagic mechanism. *Nat Commun,* 10**,** 2059.

YANG, M.-M. 2013. *Characterisation of ARMCX Proteins in Retinal Pigment Epithelium.* Master degree, UCL.

YOGEV, O. & PINES, O. 2011. Dual targeting of mitochondrial proteins: mechanism, regulation and function. *Biochim Biophys Acta,* 1808**,** 1012-20.

ZHAO, S., RIZZOLO, L. J. & BARNSTABLE, C. J. 1997. Differentiation and Transdifferentiation of the Retinal Pigment Epithelium.

ZHENG, Y. R., ZHANG, X. N. & CHEN, Z. 2019. Mitochondrial transport serves as a mitochondrial quality control strategy in axons: Implications for central nervous system disorders. *CNS Neurosci Ther,* 25**,** 876-886.

ZILOCCHI, M., FINZI, G., LUALDI, M., SESSA, F., FASANO, M. & ALBERIO, T. 2018. Mitochondrial alterations in Parkinson's disease human samples and cellular models. *Neurochem Int,* 118**,** 61-72.

Appendix

Table 0.1 Armcx/Armc10 protein sequences

Protein names	NCBI Accession number
Armcx1	NP_057692.1
Armcx2	NP_808818.1
Armcx3	NP_057691.1
Armcx4	NP_001243084.2
Armcx5	NP_001161951.1
Armcx6	NP_001171697.1
Armc10 (Human)	NP_001154481.1
GASP1	NP_001171656.1
GASP2	NP_001171803.1
GASP3	NP_001135999.1
Armc10 (Marsupial)	XP_007504121.1
Armc10 (Mouse)	NP_080310.1
Armc10 (Teleost fish)	XP_009296248.1

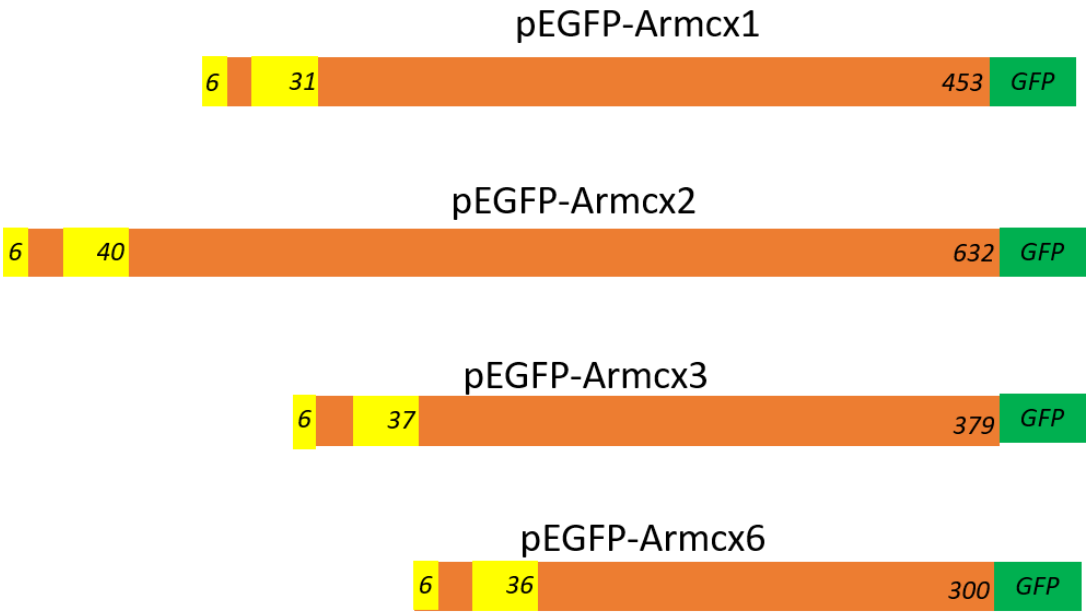

Figure 0.1 Armcx-GFP constructs. Representation of Armcx1-3 and 6 constructs fused to GFP tag; MTS targeting sequence is labelled in yellow including the number of amino acids that spans.

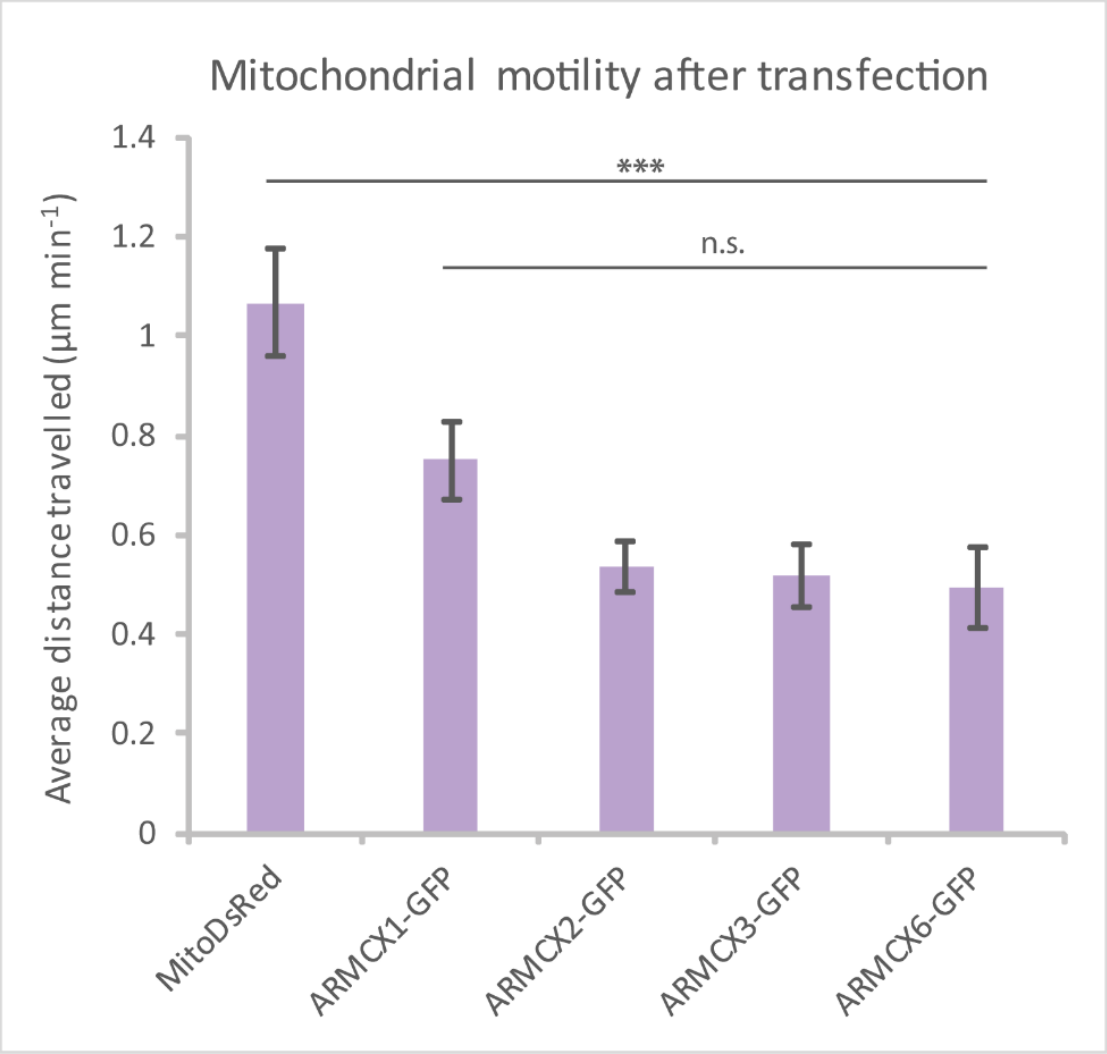

Figure 0.2 Armcx overexpression affects mitochondrial motility. ARPE-19 cells were co-transfected with 0.1 ug of Armcx plasmid DNA and 1 ug of MitoDsRed plasmid for 24 h incubation. 10 minutes time-lapse images were taken by Nikon fluorescence microscopy with 1 min interval. The Histogram displays results of Manual Traking plugin used to monitor mitochondrial motility (mean distance travelled in uM min-1). Error bars represent bootstrapped SEM values. Individual mitochondria were tracked for each ARMCX (n=3, 3 videos per sample). A Kruskal-Wallis test showed significant difference between all Armcx proteins and MitoDsRed control. The data is courtesy of Alice Kirby, a Master student at Institute of Ophthalmology, UCL in 2014.